Particle Tracking in a Lab-Scale Conical Fluidized Bed Dryer

A Thesis Submitted to the College of Graduate Studies and Research
in Partial Fulfillment of the Requirements for the Degree of
Master of Science
In the Department of Chemical Engineering
University of Saskatchewan
Saskatoon, Saskatchewan

By

Pankaj Khanna

Permission for use

The author has agreed that the Libraries of the University of Saskatchewan may make this thesis freely available for inspection. Moreover, the author has agreed that permission for extensive copying of this thesis for scholarly purposes may be granted by the professor(s) who supervised this thesis work recorded herein or, in their absence, by the Head of the Department of Chemical Engineering or the Dean of the College of Graduate Studies. Copying or publication or any other use of thesis or parts thereof for financial gain without written approval by the University of Saskatchewan is prohibited. It is also understood that due recognition will be given to the author of this thesis and to the University of Saskatchewan in any use of the material of the thesis.

Request for permission to copy or to make other use of material in this thesis in whole or parts should be addressed to:

Head

Department of Chemical Engineering

University of Saskatchewan

57 Campus Drive

Saskatoon, Saskatchewan

S7N 5A9

Canada

Abstract

Conical fluidized bed dryers are widely used in the pharmaceutical industry due to their high heat and mass transfer characteristics. Despite their widespread use, very little is known about the hydrodynamics of conical fluidized bed dryers. Wet pharmaceutical granule has high moisture content and wide particle size distribution (PSD), which can lead to poor mixing and non uniform drying. Uneven moisture content in the final product can adversely affect the quality and shelf life of these high value drugs. Previous studies on the conical fluidized bed dryers focused on the study of the gas phase, however motion of particulate phase has never been studied. Particle tracking is an important tool to study the motion of the particulate phase.

Two particle tracking techniques were developed and used to study the motion of the particulate phase in a conical fluidized bed dryer. The first technique was radioactive particle tracking (RPT) which was developed at the University of Saskatchewan laboratory for a vessel having conical geometry. Experiments were conducted using dry pharmaceutical granule and during the actual drying of wet pharmaceutical granule. Two radioactive tracers of different sizes (1.6 to 2.6 mm) were tracked in each set of experiments to determine the effect of particle size on particle motion and particle mixing. Superficial gas velocities of 1, 1.5, 2 and 2.5m/s were used in dry bed studies to quantify the effect of superficial gas velocity. The second particle tracking technique was developed at the labs of Merck Frosst Canada Inc. Movies were captured using a high speed video camera coupled to a borescope and then analyzed off-line using image analysis software.Three powders having mean particle diameters of 774,

468 and 200 microns were used. Experiments were conducted at superficial gas velocities of 1.5, 2 and 3 m/s.

RPT revealed that there is a distinct circulation pattern of the particulate phase. Particles move upwards at high velocities near the centre of the bed and fall slowly near the walls. Furthermore, most of the gas flow is concentrated near the centre of the bed and the circulation pattern was observed at all the superficial gas velocities. Particle size of the tracer particle and PSD of the bed material had an appreciable impact on particle mixing with bigger particles exhibiting higher segregation tendencies than the smaller ones in the case of dry granule having a broad PSD. Particle segregation due to size difference was more pronounced at a superficial gas velocity of 1 m/s. However, segregation decreased with an increase in superficial gas velocity. During drying of wet granule, particle mixing and motion of the tracer particle was poor during the first 7 minutes of drying suggesting that most of the gas flow was concentrated near the centre of the bed. Particle mixing and average particle speeds increased considerably when the moisture content in the granule was less than 18 wt% suggesting a change in the hydrodynamics of the bed with the gas being more evenly distributed throughout the bed. Image analysis of high speed movies also suggested that a dilute region existed at the center of the bed. These observations were in agreement with the observations made by RPT.

Acknowledgements

First and foremost, I wish to express my gratitude to my supervisor Dr. Todd Pugsley for his continuous support and encouragement and giving me sufficient freedom to pursue my research goals. I would also like to thank Helen Tanfara and Dr. Hubert Dumont of Merck Frosst & Co., for their guidance and support during my research internship. I am also indebted to other members of my advisory committee Dr. Ajay Dalai and Dr. Gordon Hill for their helpful suggestions throughout the project.

A special thanks to Dr. Rob Pywell from the Department of Engineering Physics for his help in writing one of the software codes. Many thanks to the technical and administrative staff of the Department of Chemical Engineering for their help.

I would like to express my gratitude to all the members of the fluidization and particle characterization group for all the useful discussions and suggestions. Your friendship made a big difference and I hope our friendship continues to grow in the future.

Last but not the least, I would like to acknowledge the continuous love and support from my family in India. Financial support from NSERC and Merck Frosst & Co. is also gratefully acknowledged.

Table of contents

List of tables

List of figures

Nomenclature

f_a	Probability that Gamma say escapes the reactor without scattering
f_D	Probability that Gamma ray interacts with detector crystal
r	Radius of the detector of the detector, mm
d	Distance traveled by the photon in the detector, mm
dr	Photon path length traveled in the reactor, mm
p	Distance of the tracer from the detector axis, mm
h	Distance between the center of the detector face to the tracer location
T	Sampling time, sec
f	Accuracy factor
x,y,z	Cartesian directions
M_i	Measured counts
C_i	Calculated counts

Greek symbols

μ	Total attenuation coefficient, /m.
ε	Total detector efficiency
ε'	Total intrinsic efficiency
$\theta, \alpha, \beta, \gamma$	Angles, rd.
Φ	Photopeak ratio
Ω	Solid angle, strd
υ	Number of Gamma rays emitted/ disintegration
τ	Dead time per recorded pulse, s.
ς	Statistical weight

ω	Statistical weight
α	Angle in detector frame, rd.
σ	Standard deviation

Subsript

Cri	Critical
Max	Maximum
w	Wall
r	Reactor
D	Detector

Chapter 1 Introduction

1.1 Manufacture of solid dosage form pharmaceuticals

Approximately 80% of pharmaceutical products are in the solid dosage form (i.e. tablets and capsules). Tablets and capsules are made either by dry-blending of the fine powder ingredients (also called the direct method) or by combining the powder ingredients in a wet granulator, followed by drying to achieve the desired moisture content in the final product. In the latter case, conical fluidized bed dryers are widely used in the pharmaceutical industry.

1.2 Gas solid fluidization

1.2.1 Fluidization

Fluidization is a process by which a static bed of granular solids is converted to a dynamic fluid-like state by passing a fluid (liquid or gas) upward through the bed. There are two types of commonly used fluidized bed systems: gas-solid fluidized beds and liquid-solid fluidized beds. Since the focus of the present work is gas-solid fluidized beds, only the characteristics and properties of gas-solid fluidized beds will be discussed further.

When fluidized, a bed of solid particles takes on certain fluid-like properties. For instance, like water in a bucket, the bed will conform to the volume of the vessel, its surface remaining perpendicular to gravity; objects with a lower density than the bed density will float on its surface, while objects with a higher density sink to the bottom of the bed. The fluidic behavior also allows the particles to be transported like a fluid, channeled through pipes, not requiring mechanical transport such as a conveyer belt.

1.2.2 Regimes of fluidization

When a gas is introduced at a low flowrate into a vessel containing a bed of solid particles, due to its small volume, it passes through the voids between the solid particles and the bed remains in a fixed state. The only evidence of the presence of the gas in the bed is the pressure drop that is registered across the bed due to flow of the gas. When the flow of the gas is increased, the drag produced by the upward flow of gas increases and the pressure drop across the bed also increases linearly with the increase in gas velocity. Further increase in gas flow leads to a point where the upward drag produced by the passing gas counteracts the downward pull of gravity on the particles and the frictional effects of the vessel wall. At this point, the bed becomes fluidized and pressure drop across the bed becomes constant. The velocity of the gas at this point is called minimum fluidization velocity and it is one of the most important parameters in fluidized bed design. The value of minimum fluidization velocity depends on many factors; two of the most important factors are the physical properties of the particles and the fluidizing gas.

With further increase in gas velocity, the bed passes through six distinct fluidization regimes. Lim et al. [1] identified six distinct fluidization regimes for gas-solid fluidized beds. The fluidization regimes are identified on the basis of motion of the solid phase and nature of the bubbles of the fluidizing gas passing through the bed. The first regime in called smooth fluidization, in this regime the bed is fluidized smoothly and expands uniformly with the increase in gas velocity. With further increase in gas velocity, the excess gas passes through the bed as bubbles and therefore, this regime is called bubbling fluidization. The next regime is called the slugging regime. In this regime, the bubbles grow in size and approach the internal diameter of the vessel with increasing gas velocity. The slugging regime is typically observed in beds having large height to

diameter ratios and fluidizing coarse particles. In some cases, the bed directly goes into the regime of turbulent fluidization from bubbling fluidization thereby bypassing the regime of slugging fluidization. In turbulent fluidization, bubbles become distorted and eventually disappear due to the high shearing force encountered by the fast moving gas. Significant entrainment takes place in this regime and a cyclone at the exit of the bed may be needed to capture the solids. The solids can be returned back to the system by either an internal or external return line. This type of system is referred to as a circulating fluidized bed, or a CFB. Further increase in gas velocity leads to more entrainment and the so-called fast fluidization regime and finally all of the solid particles from the bed become entrained in the fluidizing gas and this regime is known as pneumatic transport. The above mentioned six regimes are depicted in figure 1.1.

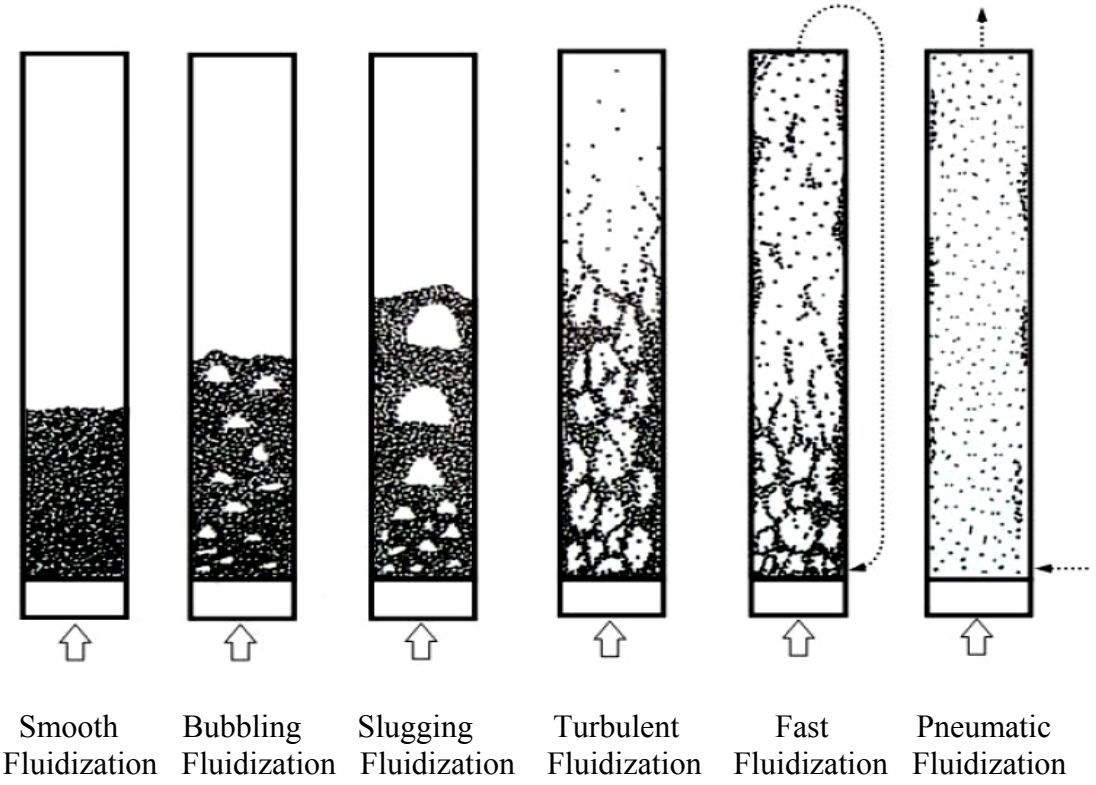

Figure 1.1 Regimes of fluidization in gas-solid fluidized bed taken from Lim et al. [1]

1.2.3 Geldart classification of powders

Geldart [2] classified powders into groups A, B, C and D, based on their density, mean diameter and their fluidization properties (figure 1.2). Group A powders, when fluidized by air at ambient conditions, give a region of non-bubbling fluidization beginning at minimum fluidization velocity, followed by bubbling fluidization as fluidizing velocity increases. Group B particles are coarser and denser and give only bubbling fluidization. Group C powders are very fine, cohesive powders which are not suitable for fluidization and Group D powders are large particles and have the ability to produce deep spouting beds.

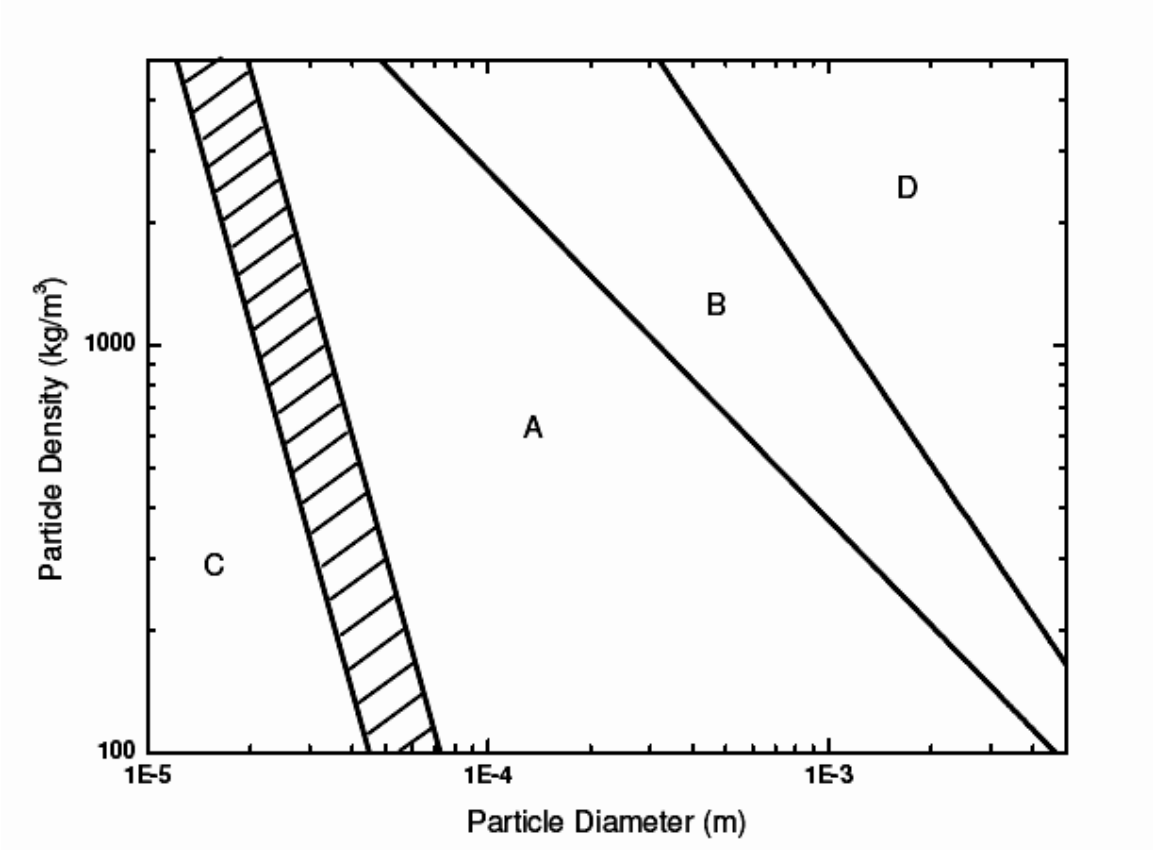

Figure 1.2 The Geldart chart for classification of powders (Kunii and Levelspiel [3])

1.2.4 Segregation in fluidized beds

Segregation is likely to occur when there is substantial difference in the drag/ unit weight between different particles. Particles having higher drag/unit weight migrate to the surface while particle with a low drag/ unit weight migrate to the bottom of the bed. Segregation leads to poor mixing and hence affects the performance of fluidized beds. Geldart [2] used powders having mono-disperse particle size distribution; however, in the case of powders having polydisperse particle size distribution, the mean particle diameter alone is not sufficient to completely characterize fluidized bed behaviour. The distribution of particle sizes about the mean also plays an important role [4]. Earlier studies in the 1940's showed that addition of small quantities of fines led to substantial decrease in the apparent viscosity of a fluidized bed of synthetic cracking catalyst [5]. Later studies confirmed that broadening of particle size distribution (PSD) by addition of fines improves the uniformity of fluidized beds by decreasing the minimum fluidization velocity and increasing the bed expansion as well as minimum bubbling velocity [5]. Gauthier et al. [6] studied the influence of PSD of powders on the fluidization velocities of Geldart B and D group sand particles. They conducted experiments with powders having the same density, but varied the PSDs and the mean diameter. It was stated that wide PSD powders show fluidization characteristics quite different from powders having narrow PSD. Rowe et al. [7] studied segregation in a binary mixture of particles and introduced the terminology of jetsam (the larger particles) and flotsam (the smaller particles). The jetsam was shown to have a tendency to settle near the bottom of the bed while the flotsam stayed near the top of the bed. Hoffmann and Romp [8], first studied segregation in sand particles (Geldart B) having a continuous PSD. They reported that segregation patterns were very sensitive to the PSD and the relative humidity of the

fluidizing gas. Courser sand particles tended to settle to the bottom of the bed at low superficial gas velocities.

1.3 Conical fluidized bed dryers

Conical fluidized bed dryers are favored in the pharmaceutical industry because of their high heat and mass transfer rates, which can be attributed to the efficient gas-solid contacting during the drying process. Another advantage of the conical geometry is that the cross sectional area increases with height. Therefore, the superficial velocity decreases as the gas flows upward through the bed, making it possible to maintain higher velocity at the inlet as compared to the outlet. This leads to better mixing of the particulate phase [9]. Since most of the pharmaceutical powders are heat sensitive, overheating or prolonged exposure to heat can adversely affect the quality of the product as well as increase the cost due to loss of high value drug. Therefore, rapid and uniform drying is essential to the process. Furthermore, rapid drying decreases the time required for drying and hence increases efficiency and production. A fluidized bed dryer can reduce the drying time to several minutes, compared with several hours in the case of a conventional tray dryer [9]. Fluidized bed dryers are generally considered to operate isothermally, which results in easy operation and control of bed parameters, as the temperature of the bed is easily maintained.

Pharmaceutical granules have a wide PSD ranging from approximately 50 microns to a 3 millimeters; this wide PSD can lead to segregation in the bed, which can result in non-uniform drying [4]. With the advent of high potency designer drugs, the efficiency of the drying step becomes all the more important as operation in a non-optimal state can lead to non-uniform moisture content and granule attrition in the final

product, which may be harmful for these high value drugs. Moisture in the final product can lead to decreased shelf life as well as decreased product quality while over-drying can change the chemical composition or the crystal structure of one or more constituents of the final product.

1.4 Granule drying studies by the U of S fluidization group

Wormsbecker et al. [10], studied segregation tendencies in a conical fluidized bed dryer using dry pharmaceutical granules of wide PSD and found that, while larger particles segregate at the bottom of the bed in accordance with the behaviour of fluidized beds, static bed height showed no influence on radial or axial segregation. Tanfara et al. [4], measured voidage profiles with electrical capacitance tomography (ECT) inside a conical fluidized bed dryer and found that, for the wide PSD studied, an annular flow of gas was established at velocities up to and including 0.50 m/s due to segregation of large particles at the bottom of the fluidized bed. At higher gas velocities, a centrally concentrated gas core surrounded by dense annulus at the wall was found. Recently, Wiens et al [11], extended the ECT work done by Tanfara et al [4], by studying the voidage profiles inside a conical fluidized bed dryer at higher superficial gas velocities (up to 3m/s) and reported that a dense region exists near the wall of the fluidized bed with decreasing solids concentration towards the centre. Chaplin et al. [12] applied the ECT technique to study actual drying of wet pharmaceutical granule in a conical fluidized bed dryer and reported the presence of a highly centralized dilute core region during the early stages of the drying process resulting in most of the gas passing through the centre of the bed. The gas distribution improved with a decrease in moisture content of the bed material during the drying process.

1.5 Knowledge gap

Despite its widespread use in the pharmaceutical industry, very little is known about the hydrodynamics of a conical fluidized bed dryer. There are few published studies in the field of fluidized bed drying of wet pharmaceutical granule and the need for research in this area is clearly stated in the work of Wormsbecker et al. [10]. The previous ECT studies described above have provided important information about gas void fraction and its distribution in the vessel. However, it does not provide any information about the velocity and circulation pattern of the particulate phase. Wormsbecker et al. [10] has proposed a mechanism of segregation but it cannot be validated due to non-availability of experimental data. To date, there is no study that involves following the trajectory of tracers of different sizes in a media having wide PSD in a conical fluidized bed and particle tracking has never been performed in an actual drying experiment in which the hydrodynamics of the bed changes considerably due to loss of moisture during drying. Furthermore, characterization of inhomogeneous two phase flow is incomplete without the knowledge of the motion of the particulate phase. Therefore, it is evident that there is a knowledge gap which needs to be filled to fully understand the movement of particles having wide PSD inside a conical fluidized bed dryer.

1.6 Objective of the study

The above mentioned knowledge gap leads to the following objectives for the present study:

1. To develop a particle tracking system for a lab-scale fluidized bed having conical geometry and containing pharmaceutical granule.

2. To implement the particle tracking system to study the motion of the particulate phase with respect to changes in superficial gas velocity and particle diameter.
3. To perform particle tracking in an actual drying experiment to understand the effect of loss of moisture on particle mixing and segregation in a conical fluidized bed dryer.
4. To perform particle tracking in an actual industrial setting.

1.7 Outline of Thesis

A literature review of the study of conical fluidized bed dryers and particle tracking techniques used in the present study will be presented in chapter 2. Development of a particle tracking system included selection of relevant equipment and development of a software for data acquisition and analysis. The description of equipments and development of software will be discussed in detail in chapters 3 and 4, respectively. A radioactive particle tracking (RPT) system was successfully developed and used to perform particle tracking in a bench-sale conical fluidized bed dryer; the results of RPT experiments will be presented in chapter 5. To achieve the final objective of this study, particle tracking experiments were performed in the laboratories of Merck Frosst Canada Ltd. (Kirkland, Quebec) using a conical fluidized bed dryer. A novel particle tracking technique consisting of a high speed camera and borescope was used for these experiments. The results of particle tracking experiments at Merck Frosst labs will be discussed in chapter 6. Conclusions of the present study and recommendations will be presented in chapter 7.

Chapter 2 Literature review

2.1 Previous studies of conical fluidized bed dryer

The U of S fluidization group is the only research group in the world studying hydrodynamics and drying of wet pharmaceutical granule having wide PSD in a conical fluidized bed dryer. The key findings of previous research studies by our group are presented in this section.

Tanfara et al. [4] and Wiens et al. [11] studied the behaviour of the gas phase in a conical fluidized bed dryer using electrical capacitance tomography (ECT). ECT is a non-intrusive two-phase flow measuring technique that allows for the determination of dispersed phase distribution within an enclosed area such as vessel or a pipe. The ECT system produces images of the cross-sectional area enclosed by the sensors based on the difference in the dielectric constants or permittivities of the two phases under investigation [9]. The ECT system used by Tanfara et al. [4] and Wiens et al. [11] consisted of two planes of eight individual measuring electrodes and the image reconstruction from the data recorded by the electrodes was done using a MATLAB iterative algorithm [11].

Tanfara et al. [4] investigated the effect of particle size distribution (PSD) of dried pharmaceutical granule on local voidage inside a conical fluidized bed dryer. The so called PSD1 was the pharmaceutical granule having wide PSD and four additional granule mixtures having different PSDs were created by manipulating PSD1. For each of the five PSDs studied, the static bed height was varied between 12 and 17 cm and the superficial gas velocity was varied between 0.05 and 0.75 m/s. Tanfara et al. [4] reported annular flow of gas at lower superficial gas velocities but observed a centralized gas flow at higher superficial gas velocities. They concluded that segregation of bigger particles at

the bottom of the bed at lower superficial gas velocities resulted in dispersion of fluidizing gas which led to the annular flow. Furthermore, in the granule mixtures that contained no particles greater than 500 μm, a centralized flow of gas was observed at all superficial gas velocities. The voidage at the centre of the bed increased with the increase in superficial gas velocity, suggesting that more gas was passing through the centre of the bed. Increasing the static bed height tended to decrease the centralized gas flow in the case of PSD1. Again, the segregation of bigger particles was cited as the reason for this behaviour. The centralized gas flow increased with increase in static bed height in the case of the remaining four PSDs tested.

Wiens et al. [11] extended the work of Tanfara et al. [4] by studying the voidage profiles at higher superficial gas velocities (up to 3 m/s). The range of superficial gas velocity covered both the bubbling and turbulent fluidization regimes. The static bed height was kept constant at 16 cm for all the experiments. The equipment and measurement system used by Wiens et al. [11] was similar to the one used by Tanfara et al. [4]. Two granule mixtures of differing PSDs were studied. The first had a bimodal PSD with modes occurring at 168 and 1288 μm and was similar to the PSD1 used by Tanfara et al. [4]. The second granule mixture had a narrow PSD with a mean particle size of 237 μm. For both PSDs, it was reported that an "M" shaped time averaged voidage profile existed in the bed at higher superficial gas velocities, which was typified by high solid concentration near the wall and the centre of the fluidized bed, with much lower solid concentrations in between. Furthermore, two main bubble types were observed, circular bubbles and penetrated bubbles. Penetrated bubbles were characterized by high solids concentration in the core of the bubble. At higher superficial gas velocities, splitting of the penetrated bubbles was commonly seen resulting in a big bubble, a small

bubble and high solids concentration in the middle of the bed. Bubble splitting was associated with the turbulent fluidization regime and it was reported that fluidization regime transition from bubbling to turbulent fluidization happened over a wide range of superficial gas velocity due to the presence of larger particles. Furthermore, it was observed that as compared to the upper ECT plane, regime transitions happened at lower superficial gas velocity in the lower ECT plane. In a conical bed the cross sectional area increases with increasing axial position, thereby reducing the velocity of the fluidizing gas; the conical geometry of the bed was therefore cited as the main reason for the observed differences in regime transition at two different axial positions in the bed.

With the change in moisture content of the bed material during the drying process, its electrical permittivity also changes. This makes it difficult to use the ECT technique during the drying process since the ECT measurement principle is based on a constant permittivity ratio of the solid and gas phases. Chaplin et al. [12] developed a dynamic calibration procedure for the ECT system to account for the change in moisture content during drying. The calibration procedure was based on a least-squares fit of packed bed capacitance readings taken during the drying process. The calibration procedure allowed Chaplin et al. [12] to study changes in the hydrodynamics of the fluidized bed dryer during actual drying of wet pharmaceutical granule by employing the same ECT system previously used by Tanfara et al. [4].

Van Ommen et al. [13] developed a signal analysis technique called the S-Statistic to study pressure fluctuations during fluidization. The technique was shown to successfully identify the subtle changes in pressure fluctuations due to changes in hydrodynamics of the bed during fluidization. Chaplin et al. [12] used the S-Statistic to study local voidage profiles in the bed by analyzing the local permittivity fluctuations

obtained from the ECT data captured during drying of wet pharmaceutical granule. Experiments were conducted at initial bed wet bed loadings of 3, 3.5 and 4 kg. For the better circulation of wet material, superficial gas velocity was maintained between 2 and 2.5 m/s during the first 10 minutes of the experiment and later reduced to 1.4 m/s for the remainder of the experiment. Inlet air temperature was maintained at 65^{o}C throughout the experiment. Chaplin et al. [12] presented the tomographic images of the drying process at moisture contents of 28, 18 and 10 wt% and reported that at moisture content of 28 wt %, which was 10 minutes into the drying process, a core region was present at the centre of the bed with most of the gas channelling through it. This resulted in upward flow of particles at the centre and downward flow in the dense region near the walls. Strong cohesive forces between the particles due to high moisture content were believed to be the reason for this observation. However, with the decrease in moisture content to 18 wt %, the dilute core was broken down resulting in better distribution of gas inside the bed. When the moisture content of the bed material was reduced to 10 wt%, a restricted region was again observed near the centre of the bed resulting in higher velocities of upward moving particles. This observation was used to explain the higher levels of particle entrainment in the later stages of drying process. The statistically relevant changes observed by the S-Statistic technique during the drying process confirmed the hydrodynamic changes observed by the ECT system.

Wormsbecker et al. [10] developed a novel core sampling technique to study segregation tendencies of dry pharmaceutical granule having wide PSD. The PSD of the granule was similar to PSD1 of Tanfara et al. [4]. The bed was fluidized for 15 minutes at a given superficial gas velocity, at which point the air supply to the bed was abruptly shut off. Core samples were extracted by using five core sampling probes. The samples were

extracted from five different radial positions of the bed and each sample was divided into 4 cm axial segments. This was done to study radial and axial segregation respectively. Experiments were conducted at superficial gas velocities of 0.5, 0.75 and 1 m/s at static bed heights of 12 and 17 cm. It was observed that particles larger than 800 μm showed a tendency to segregate at the bottom centre of the bed. It was suggested that the particles were transported upward in the dilute region near the centre of the bed and circulated downward in the region close to the wall of the vessel. Static bed height did not appear to have a significant effect on the segregation patterns for the given experimental conditions investigated.

The studies of Tanfara et al. [4], Wiens et al. [11] and Chaplin et al. [12] were mainly confined to the study of gas phase; circulation and mixing of the particulate phase in their conical fluidized bed dryer could not be studied using the ECT technique. Knowledge of the gas-solid fluidization is incomplete without information on the motion of the particulate phase. The study by Wormsbecker et al. [10] provided useful information regarding segregation tendencies of the particulate phase, however, it did not provide any information about the particle velocities and mixing patterns of the particulate phase in a conical fluidized bed dryer. Wormsbecker et al. [10] studied particles segregation up to superficial gas velocity 1 m/s, however, higher superficial velocities are typically employed in the pharmaceutical industry. Furthermore, the suggested circulation pattern for the particulate phase could not be verified due to lack of experimental data. These knowledge gaps in understanding the motion of the particulate phase can be filled by performing particle tracking studies.

2.2 Particle tracking systems

Particle tracking can provide useful information about the motion of the particulate phase inside a fluidized bed. In particle tracking, single or multiple tracer particles, which are dynamically similar to the particulate phase under investigation, are introduced inside the bed and tracked over a period of time to yield data about the motion and mixing of the particulate phase. Various particle tracking techniques such as radioactive particle tracking (RPT), positron emission particle tracking (PEPT), video imaging, and particle tracking using magnetic tracers have been developed and used by researchers in the past. For the present study, particle tracking techniques of RPT and video imaging were developed and used. Therefore, the history of development and usage of these two techniques is discussed in the next section.

2.2.1 Radioactive Particle Tracking

Radioactive particle tracking (RPT) is a non-invasive advanced measurement technique, which has received considerable attention during the last decade [14]. In the RPT technique a radioactive tracer particle emitting high energy γ-rays and dynamically similar to the particulate phase to be studied, is introduced into the process of interest and the movement of the tracer is tracked by scintillation detectors installed around the system. The intensity of γ-rays falling on the detector is proportional to the distance of the tracer particle from the scintillation detector. Therefore, by studying the amount of radiation falling on each detector, it is possible to determine the position of the tracer particle with respect to time. By tracking its motion over time, the three-dimensional velocity profile of the tracer particle and by extension the particulate phase, can be generated.

The first modern RPT system was developed and used by Lin et al. [15] to study the recirculatory pattern of solid particles in bubbling fluidized beds. Lin et al [15] used polynomial functions obtained by curve fitting of the calibration data for the reconstruction of tracer position inside the vessel. This approach was based on the principle that the number of γ-rays counted by a detector is only dependent on the distance between the point tracer and a virtual centre in the detector. To calibrate the system, a tracer particle was placed at a number of known locations inside the bed and a polynomial function was fitted to the counts recorded. An upgraded version of the system of Lin et al. [15] was developed at Washington University in St. Louis and, due to the versatility of this RPT system, it was used to study gas-solid fluidized beds, bubble columns, slurry bubble columns and liquid-solid risers (Devanathan et al. [16], Duduković et al. [17], Yang et al. [18] and Kumar et al. [19]). However, this approach suffered from low resolution and accuracy in dense flows. Furthermore, this approach was based on a tedious calibration process involving manual placement of the tracer at a large number of known locations inside the bed.

Larachi et al. [20] used a rigorous phenomenological model describing the interaction of γ-rays with the geometry of the vessel under investigation to find the location of the tracer particle from the counts recorded by the scintillation detectors. A Monte-Carlo simulation was used to create a map of counts recorded by scintillation detectors for a large number of points inside the vessel. The simulated counts were refined by a calibration process, in which a tracer particle was placed at known locations and the counts recorded by the scintillation detectors were compared with the Monte-Carlo counts to calculate optimal model parameters. Although the calibration process used in this method was similar to the one used by Lin et al. [15], the number of

calibration points needed was considerably smaller. During an actual particle tracking experiment, a least square search was used to compare the recorded counts with the simulated counts to find the exact location of the tracer particle. Godfroy et al. [21] used neural networks to calculate the position of the tracer particle from the experimental data. This method required less computational time to reconstruct the location of tracer particle as compared to the methods of Lin et al. [15] and Larachi et al. [20]. However, before the neural network could accurately determine the location of the tracer particle, it had to be trained or calibrated by using a large number of data points. The neural network approach for reconstruction of tracer location can not be used in the absence of training data. Godfroy et al. [21] used data points generated by the Monte-Carlo method to train the neural networks In the present study, the Monte-Carlo simulation approach developed by Larachi et al. [20] has been used in the development of RPT system. It is important to note that all the RPT systems mentioned above were developed for vessels having cylindrical geometry and RPT has never been used in a vessel having conical geometry. The details of the development of RPT system for a vessel having conical geometry will be described further in chapter 3.

2.2.2 Video imaging

Video imaging has been used by many researchers to observe the motion of particulate phase in a fluidized bed. Video imaging techniques involve introduction of fluorescent or coloured tracer particles inside a fluidized bed and recording their motion with a video camera Bram et al. [22] used computer-based imaging to measure the particle velocity and voidage profiles in a fluidized bed. Closely sized 1 mm glass beads were used as tracer particles and their motion was tracked by using a charged couple

device (CCD) variable shutter speed camera. Customized software was developed and automated to process the digitized video images using an image processing board. This technique suffered from low resolution and therefore, the system was not able to track fast moving particles inside the bed. Kai et al. [23] used tracer particles impregnated with photochromic dye to measure the particle movement in a two-dimensional fluidized bed. All the porous particles inside the bed were impregnated with an aqueous solution containing a photochromic dye. Selected particles were then irradiated by an ultraviolet light resulting in particles changing color for several seconds. The motion of the tracer particles was tracked by using a high-speed video camera. Images acquired by the camera were analyzed on the PC by digitizing the coordinates of the tracer particle images in a sequence of still images. Pallarés and Johnsson. [24] recently studied mixing mechanisms of fuel particles in a fluidized bed by tracking a phosphorescent tracer particle. The movement of the tracer particle was recorded by a video camera installed near the transparent front wall of the fluidized bed and the images were digitized and analyzed using a PC.

A part of the present study was carried out in the labs of Merck Frosst Canada Inc. (Kirkland, Quebec) where there is a strict policy against contamination in their process equipments. This ruled out the use of radioactive tracer. Furthermore, the video imaging techniques mentioned above use transparent vessels to track the motion of tracer particles and therefore it is difficult, if not impossible, to use them in an industrial setting due to the opaque nature of the process equipments. Therefore, a novel particle tracking technique using a high speed video camera coupled to a Borescope was developed to study motion of the particulate phase in a conical fluidized bed dryer. The details of this technique will be presented in chapter 3.

Chapter 3 Experimental

This chapter describes the experimental apparatus and equipment used to perform particle tracking experiments as well as the experimental conditions and research methodology.

3.1 Fluidized beds

3.1.1 Plexiglas fluidized bed at U of S

All RPT experiments were carried out in the same Plexiglas conical fluidized bed dryer used by Wormsbecker at al. [10]. Figure 3.1 is a schematic of this experimental fluidized bed system. The Plexiglas vessel has a cone angle of 14^{o} with a 0.115 m inlet and a 0.265 m outlet diameter. A 1.3 m tall disengagement section is flange-connected to the cone outlet. A cyclone mounted on top of the disengagement section collects the entrained particles and drop them into a fines collection pot. A perforated-plate with 2 mm holes spaced 7.5 mm apart and drilled on a square pitch is used as the air distributor. Fluidizing air is supplied by a regenerative blower with volumetric flow of air to the bed manually controlled with two bypass valves. The flow of air into the windbox is measured with an orifice plate designed according to ASME standards for fluid flow in closed conduits. A vertical U-tube water manometer is used to determine the orifice pressure drop [25].

When operated as a dryer, electrical heating is used to provide warm drying air to the fluidized bed. Air temperature is controlled by a feedback control loop and PID controller based on the temperature measured in the windbox by means of a type J thermocouple. A sample thief is present in the product bowl section to collect granule

samples during experimental drying runs, that are analyzed for moisture and the data used to construct the drying curve.

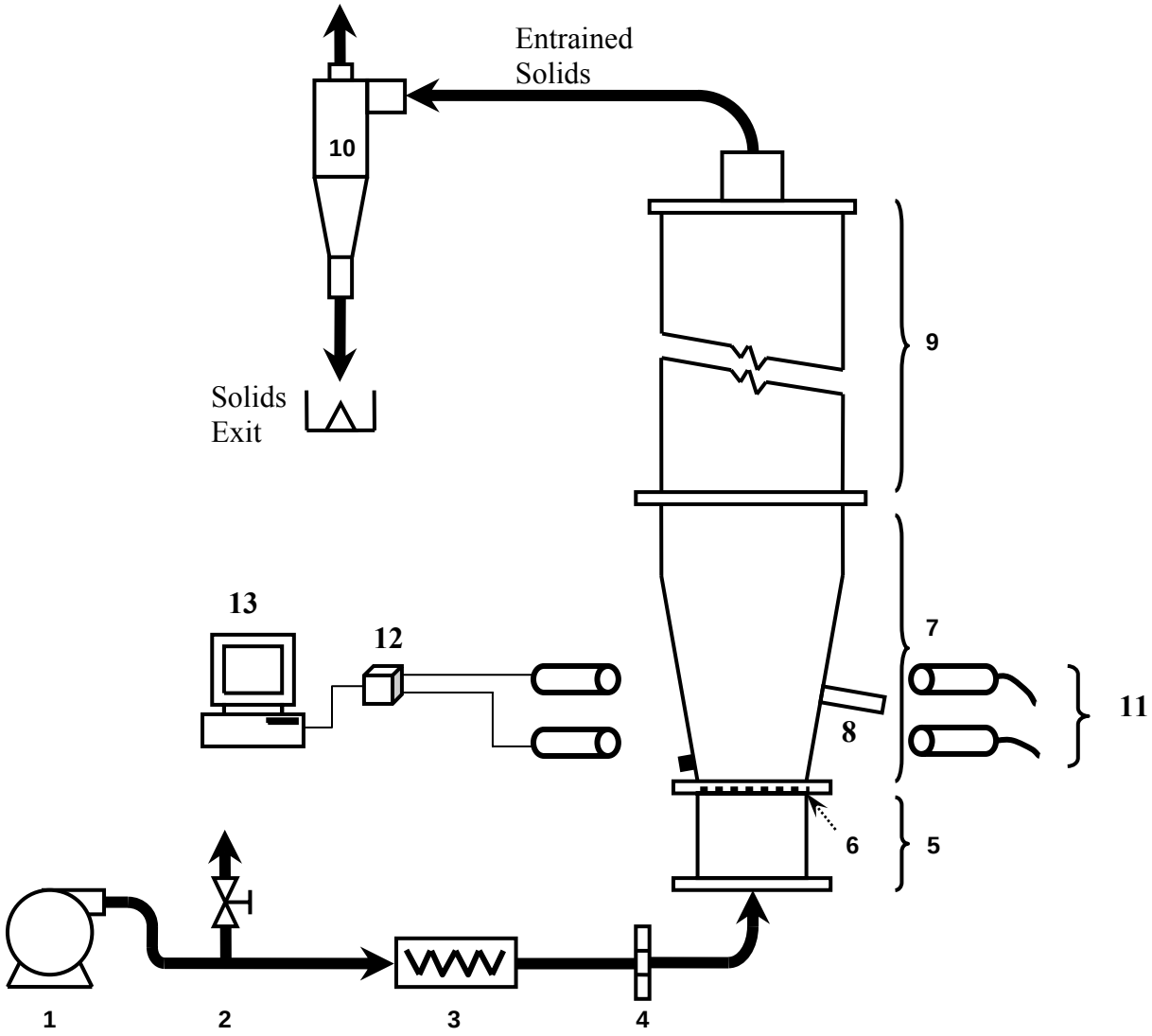

Figure 3.1 Fluidized bed apparatus components and instrumentation: blower (1), air bypass (2), heater (3), orifice (4), wind box (5), distributor (6), product bowl (7), sample thief (8), freeboard (9), cyclone (10), NaI scintillation detectors and MCA (11), USB hub (12), data acquisition computer (13)

3.1.2 Glatt GPCG-1 at Merck Frosst Canada & Co.

Particle tracking experiments using high speed video imaging system were performed in the Glatt GPCG-1 (Glatt Air Techniques, Ramsey, NJ) at the Merck Frosst

Canada & Co., labs in Kirkland, Quebec. This bench-scale conical fluidized bed dryer is fabricated of stainless steel with the inside walls of the bed having a mirrored finish. The dryer has an apex angle of 22^{o} with a 0.145 m inlet and a 0.305 m outlet diameter. Electrical heating is used to provide warm drying air to the fluidized bed and air temperature is monitored in the windbox by means of a thermocouple. Air flow is controlled by a pitot tube located in the square duct upstream of the windbox. The humidity of the drying air is not controlled, but the air intake is from a room with climate control. Filter bags present in the freeboard region of the fluidized bed collects the entrained particles, which can be added back to the process by periodically shaking the filter bags. The filter bags were pre-set to shake for 2 second every 30 seconds for each of the experiments conducted. The GPCG-1 is fitted with instrumentation for setting, monitoring and controlling air flow rate, temperature and shaking of the filter bags.

3.2 Granule preparation and characterization

Dried pharmaceutical granule supplied by Merck Frosst Canada & Co. and previously used by Wormsbecker et al. [10] and Wiens et al. [11] was used as bed material for radioactive particle tracking experiments. The formulation for the placebo granule is provided in Table 3.1. Wet granule for experiments was prepared at Merck Frosst Canada and Co. in a high-shear mixer by combining typical fine powder pharmaceutical ingredients given in Table 3.1 using an atomized water spray. The wet granule was then dried in the conical fluidized bed dryer to reduce its moisture content to less than 5%. The particle size distribution (PSD) and particle density of the granule was determined after completion of the drying process [10].

Table 3.1 Formulation ingredients for placebo pharmaceutical granule

Component	Percentage	Mass on dry basis (g)
Lactose Monohydrate	50%	250
Microcrystalline Cellulose	44%	220
Croscarmellose Sodium	2%	10
Binder	4%	20
Distilled Water	42%	210
Total Dry	100%	500
Total Wet	142%	710

Wormsmbecker et al. [10] stated that the granule exhibited a continuous bimodal PSD with modes at 168 and 1288 μm (Table 3.2). The PSD of the dried granule was measured using a Mastersizer S-Series Long Bench particle size analyzer (Malvern, Worcestershire, UK). Helium pycnometry and mercury intrusion tests were performed on samples taken from different size classes of the overall PSD. Specific pore volume was found to be 0.48 mL/g and was constant for all size classes. Particle densities for different size classes of the granule were calculated from skeletal densities and specific pore volume (Table 3.3). It was observed that particle densities vary by less than 3% from size class to size class [10].

Table 3.2 Particle size distribution of dry pharmaceutical granule

Particle Size (μm)	Mass percentage in range
<75	3.41
75-105	6.04
105-149	11.32
149-210	12.95
210-297	10.99
297-420	8.23
420-590	6.89
590-850	8.32
850-1190	9.6
1190-1680	10.41
1680-2380	7.96
2380-3360	3.71
>3360	0.17

Table 3.3 Skeletal and particle densities of selected size classes

Diameter range (μm)	Skeletal density (kg/m^3)	Particle density (kg/m^3)
208-300	1566	821
850-1180	1594	828
1180-2000	1650	843
2000-3350	1592	828
>3350	1625	830

3.3 Radioactive particle tracking (RPT)

A radioactive particle tracking (RPT) system consists of following components:

1. Radioactive tracer particle emitting γ-rays.
2. Scintillation detectors to record the radiations emitted by the tracer particle.
3. Pulse processing system to process and convert the pulses produced by scintillation detectors into meaningful data.
4. Computer interface to transfer the data from the pulse processing system to the computer.
5. Personal computer to process and correlate the data.

3.3.1 Tracer particle

As the name implies, RPT utilizes γ-rays emitted by a radioactive particle to track its movement inside the fluidized bed. Signal detection ability and counting statistics are the major aspects that govern the choice of radionuclide to be utilized in particle tracking. The performance of the RPT system expressed in terms of spatial resolution and sensitivity are directly linked to the properties of the radionuclide. In particular, the radionuclide selected for RPT study should be of very high purity so that the radiations emitted by it fall within a well defined bandwidth and interference caused by radiations emitted by impurities are minimized.

The result of the statistical nature of radioactive decay and the γ-ray detection process is that a high count rate can be measured more accurately. In order to reduce error in number of counts, a tracer particle of high radioactivity should therefore be selected. However, the source activity should not be so high that the detector is saturated when the particle comes close. Since counts are used to calculate the instantaneous

position of the tracer, the sampling time should be shorter than the time the particle takes to move a significant distance, therefore, high sampling frequencies are required at high flow velocities but the precision of the calculated positions of the tracer degrades with the increase in the sampling frequency. A compromise is generally made that takes into account the highest velocity expected to occur in the flow under study. In addition, the half life of the radionuclide should be much longer than the total time of the experiment so that the tracer does not lose activity to a significant degree during the experiment. This is balanced by the practical consideration that the half life should not be too long as the tracer having very long half life can become a source of contamination. Therefore, the tracer particle selected should satisfy many requirements at the same time which will lead to better performance. Godfroy et al. [26] conducted RPT experiments in a fluidized bed with three different commonly used radio nuclides: ^{46}Sc (2 γ-rays/disintegration, 1120 keV and 889 keV), ^{198}Au (0.96 effective γ-rays/disintegration, 412 keV) and ^{99}Mo (0.97 effective γ-rays/disintegration, 140 keV). They reported that ^{198}Au gave the best results for spatial resolution, with 7 mm for dilute and 9 mm for dense medium respectively.

In the present study, tracer particles were fabricated by mixing gold powder with epoxy resin following the approach of Godfroy et al. [26]. Epoxy resin and gold were mixed together in proportions to give a tracer with the same density as the pharmaceutical granule. After hardening of the resin mixture, a piece of the resin was cut and hand rounded to make a tracer of the desired size. The gold powder used during the fabrication of tracer particles was of 99.9 % purity (Strem Chemicals, Newburyport, MA, USA). The density of the tracer particle matched well with the placebo pharmaceutical granule with an error of 5%. The size of the tracer particle was determined by using a scanning electron microscope at the Department of Toxicology at U of S. Figure 3.2 is a picture of

1.33 mm tracer particle taken with the scanning electron microscope. The tracer particle was subjected to irradiation in the slowpoke II nuclear reactor at the Saskatchewan Research Council (SRC) to make it radioactive. The tracer particle was irradiated to achieve radioactivity of approximately 100 μCi. The time of irradiation was dependent on the amount of gold present in the tracer particle and varied from 25-60 minutes depending on the size of the particle i.e. a typical 1.33 mm tracer particle contained approximately 350 μg of gold and was irradiated for 60 minutes to achieve the radioactivity of 100 μCi.

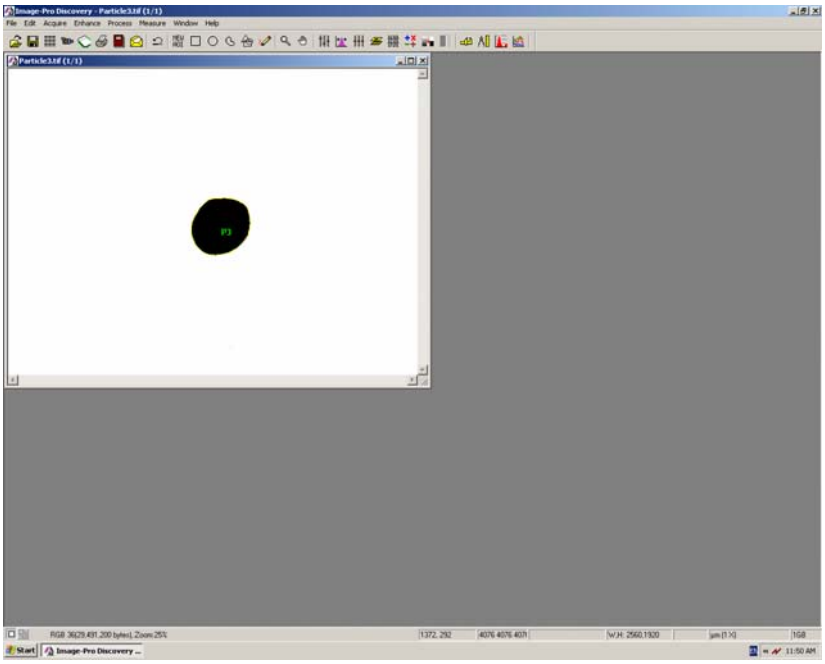

Figure 3.2 Picture of the 1.33 mm tracer particle taken with a scanning electron microscope

3.3.2 Scintillation detectors

Scintillation materials are those which produce light when ionizing radiation fall on them. This property can be used for the detection of ionizing photons or radiations. The scintillation mechanism in inorganic materials depends on the energy states determined by the crystal lattice of the material. The electrons have only discrete energy bands to move into. The lower band, called the valence band, represents those electrons that are essentially bound at the lattice sites, whereas the conduction band represent those electrons that have sufficient energy to be free to migrate throughout the crystal. There exists an intermediate band of energies, called the forbidden band, in which electrons can never be found in the pure crystal. The electrons present in the crystal lattice migrate to the conduction band from the valence band by absorbing energy of incident radiations, leaving a hole in the valence band. The return of electrons from the excited state back to the valence band is an inefficient process. Furthermore the energy gap between the two levels is such that the emitted radiation will not fall in the visible spectrum. For this reason, small amounts of impurities called activators (i.e. Tl in NaI crystal) are added so as to alter the energy band structure of the pure crystal, allowing the electrons to come back from the conduction band to the valence band through the forbidden band and hence emit energy which falls in the visible spectra. These de-excitation sites are called luminescence centres or recombination centres.

The photomultiplier or phototube is an integral part of a scintillation counter, without the amplification produced by a phototube, the scintillation counter is useless. The phototube is a fast amplifier, which in a time of 10^{-9} s amplifies to a factor of 10^{6} or more. A phototube consists of an evacuated glass tube with a photocathode at its entrance and several dynodes in its interior. The photons produced by the scintillator enter the

phototube and hit the photocathode. The photocathode emits electrons when hit by photons. These electrons are guided to the first dynode by an electric field, which emits secondary electrons when hit by electrons. Secondary electrons move from the first to the second dynode, and so on. A typical phototube may have up to 15 dynodes. The production of secondary electrons by successive dynodes leads to amplification of the signal. For best results, the spectrum of the scintillator should match the sensitivity of the photocathode; NaI(Tl) is the most popular scintillation detector and matches well with the commercially available photomultiplier tubes (PMTs). Scintillation detectors containing NaI (Tl) crystals are the most successful and commonly used scintillation detectors. They have been used previously by many researchers for the development of RPT systems. Twelve scintillation detectors having NaI (Tl) crystals of 5 cm x 5 cm (2" x 2") size were used in the present study.

3.3.3 Pulse processing system

The pulse processing system is required to process the signals generated by the Scintillation detector into useful data. It consists of preamplifier, amplifier, single or multiple channel analyzer, scaler and timer. The primary purpose of the preamplifier is to provide an optimized coupling between the output of the detector and the rest of the counting system. The preamplifier is also necessary to reduce the noise that may alter the signal. The signal that comes from the detector is very weak (in the millivolt (mV) range) and has to be amplified by a factor of 1000 or more before it can be recorded. To achieve this, the signal must be transmitted to the amplifier through a cable. If the signal is too weak it may be lost in transmission. To avoid this, the preamplifier is placed very close to the detector. The preamplifier shapes the signal and reduces its attenuation by matching

the impedance of the detector with that of the amplifier. Hence the primary function of the preamplifier is to provide the electronic matching between the output of the detector and the input of the amplifier. The main function of the amplifier is to amplify the signals by a factor of 1000 times or more. In addition to the amplification, an equally important function of amplifier is to convert the signal at the output of the preamplifier into a suitable form. The single channel analyzer (SCA) is used to eliminate noise, and in general, to reject unwanted pulses. When the pulse is amplified the noise associated with it is also amplified. Therefore, if one decides to measure all the pulses, the number will be very high on account of amplification of the electronic noise. The SCA is a device that can select the desired pulses and discard the other. In RPT, we wish to count only the photo peak values and discard the attenuated signals, therefore, the SCA can be tuned so as pulses lower than a certain height are rejected. Alternatively, a multi channel analyzer (MCA) when used with lower level and upper level discriminators can also serve as a SCA.

In the present study, each scintillation detector was attached to an Ortec DigiBASE (Advanced Measurement Technology Inc., Oak Ridge, USA), a 14-pin photomultiplier tube base for gamma-ray spectroscopy applications. The DigiBASE combines a miniaturized preamplifier, high voltage amplifier, multi-channel analyzer (MCA), lower level discriminator (LLD) and upper level discriminator (ULD) all incorporated into a light weight (287 g) compact (63 mm Diameter x 87 mm length) system with a USB connection. High voltage, LLD and ULD were adjusted to record only the photopeak counts of the ^{198}Au gold isotope. When operated in the LIST mode, DigiBASE can time stamp each photon count, which can be used to determine the number of counts recorded in a specified time interval, which acts as the scaler and timer.

A computer interface was created in Visual Basic programming language to operate the DigiBASE in LIST mode and to transfer the data recorded by DigiBASE to a personal computer for further analysis (Appendix A). DigiBASE stored the data in binary format. Hence, two separate pieces of code were written in C++ to convert the binary file into a text file and to calculate the number of counts recorded by each scintillation detector in a given time interval (Appendix B and C). An IBM Intellistation M Pro computer was used for data acquisition and analysis. Figure 3.3 provides the description of the components of the RPT system used in the present study.

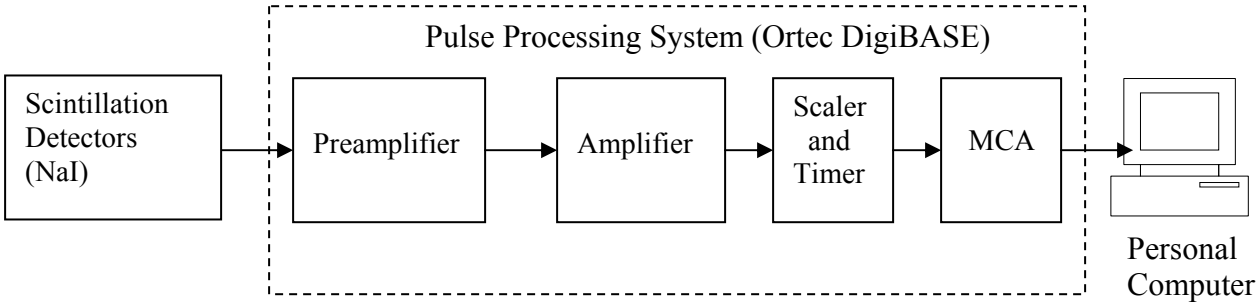

Figure 3.3 Block diagram of the components of the RPT system used in the present study

3.3.4 Arrangement of detectors

Strategic positioning of detectors around the process vessel of interest is an important step in the design of an RPT system. Placement of the detectors too close to the vessel can lead to blinding of the detectors due to recording of excessive counts. This will result in reduced sensitivity and resolution of the RPT system. Positioning the detectors too far away from the vessel leads to deterioration of spatial resolution due to a decrease in the detection solid angle and an increase in statistical fluctuation in the counts

recorded. Therefore, optimal positioning of detectors around the vessel is essential for achieving highest sensitivity and sufficiently meaningful measured counts. Recommendations of Roy et al. [27] were followed. In the present study, a special frame was built to place the 12 scintillation detectors strategically around the conical fluidized bed dryer. Detectors were arranged in 4 axial planes with 3 detectors in each plane. Figure-3.4(a) depicts the axial arrangement of detectors and figure-3.4(b) depicts the radial arrangement of detectors at each axial plane. Table 3.4 provides the location of the detectors in Cartesian coordinates.

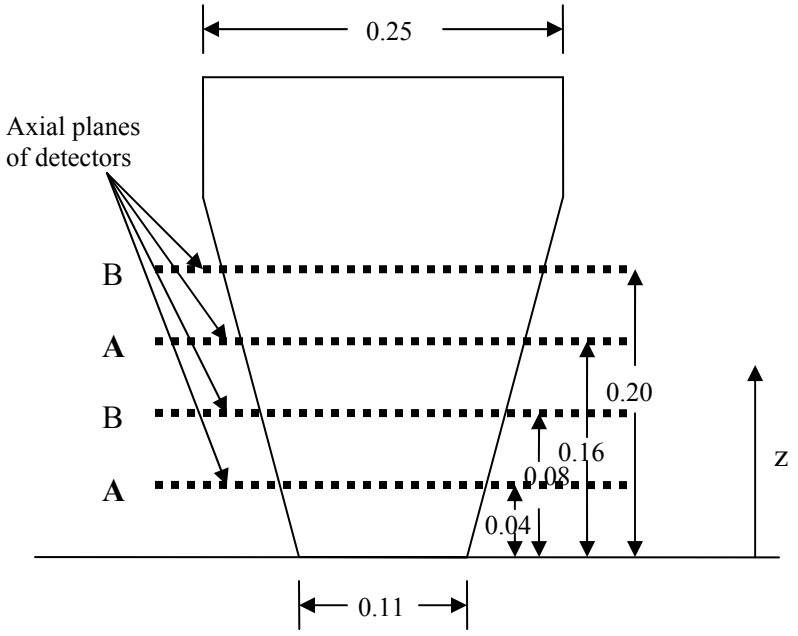

Figure 3.4(a) Axial arrangement of NaI detectors around conical fluidized bed (all dimensions in m)

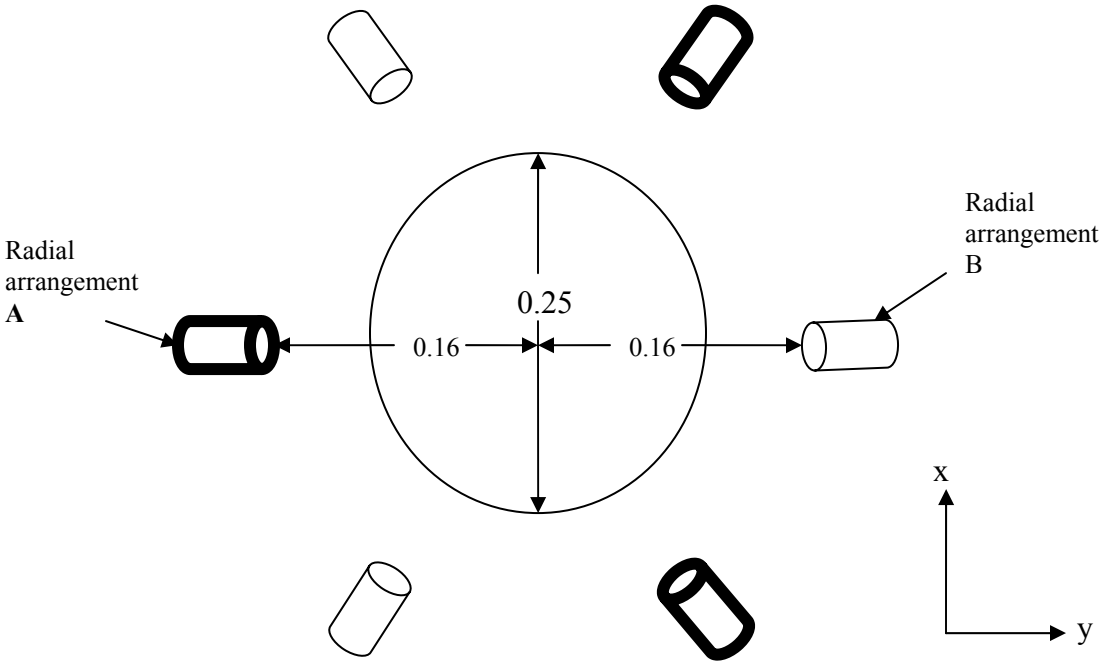

Figure 3.4(b) Radial arrangement of NaI detectors around conical fluidized bed (all dimensions in m)

Table 3.4 Location of detectors around the conical fluidized bed in Cartesian coordinates

Detector No.	MCA Serial Number	x (m)	y (m)	z (m)
1	639	0.165	0.0	0.086
2	665	-0.165	0.0	0.165
3	661	0.0825	-0.142	0.165
4	656	-0.0825	0.142	0.086
5	659	0.165	0.0	0.205
6	658	-0.165	0.0	0.046
7	657	0.0825	0.142	0.046
8	668	-0.0825	-0.142	0.205

9	638	-0.0825	-0.142	0.086
10	670	0.0825	-0.142	0.046
11	660	0.0825	0.142	0.165
12	669	-0.0825	0.142	0.205

3.3.5 Experimental conditions for RPT experiments

RPT experiments were carried with both dry and wet placebo pharmaceutical granule. Two radioactive tracers of different sizes were tracked in each set of experiments to study the effect of size of the particle on its motion inside the bed. The static bed height was held constant at 12 cm for all the dry bed studies. For wet bed studies, static bed height changed during drying due to loss of moisture; however, initial static bed height was kept constant at 16 cm for all the wet bed studies. The tracer was always placed on top of the placebo granule in the bed at the start of every experiment.

The first set of experiments with dry pharmaceutical granule was performed with granule having narrow particle size distribution between 200 and 250 μm. It was created from granule having wide PSD by using Tyler Series sieves and a Ro-Tap sieve shaker at the U of S labs. Two tracers of 2.54 mm and 1.33 mm were tracked in this set of experiments. It should be emphasized that only one of the tracer particles was present in the bed in one particular experiment. The second set of experiments with dry granule was performed with actual pharmaceutical granule having the wide bimodal PSD. The tracer sizes used in this set were 2.6 and 1.8 mm. As the fluidization state inside the bed is also dependent on the fluidization velocity, each set of the above mentioned experiments was performed at fluidization velocities of 1, 1.5, 2 and 2.5 m/s.

The third set of experiments was preformed by tracking the radioactive tracer particle during actual drying of wet pharmaceutical granule. The tracer sizes used during wet bed studies were 2.6 and 1.6 mm. The wet placebo granule was dried at a superficial gas velocity of 1.5 m/s for both the tracer studies. The air temperature was maintained at 65^0C throughout in all the experiments. Each drying experiment lasted for 25 minutes. During each drying experiment granule samples were collected every 2 minutes by using the sample thief. This was done to relate any observed changes in particle motion to moisture content of the bed material. It was necessary to operate at a superficial gas velocity of 2.5 m/s for the first 2 minutes of drying, after which the velocity was reduced to 1.5 m/s and held constant for the remainder of the experiment. The higher velocity was required to turn the bed over when it was very wet initially. The humidity of the drying air was not controlled in the dryer, but the air intake was from a room with climate control.

3.4 High Speed Imaging

As a complement to the RPT system, a novel particle tracking technique using a high speed video camera coupled to a borescope was also developed in this study. Movies were captured with the high speed video camera/borescope combination and then analyzed off-line using image analysis software.

3.4.1 High speed video camera and lighting

A Photron Ultima APX-RS FM (Monochrome) high speed camera (High Speed Imaging Inc., Mississauga, Ontario) was used to capture the high speed movies. It could capture 10,000 frames per second (fps) at 512 by 512 pixels, with a maximum speed of 250,000 fps at the cost of reduced resolution. The camera had an installed memory of 2

GB and it was connected to a personal computer through a 250 thousand fps fire wire port for data transfer. High speed photography requires high density lighting because of high frame rates, therefore, an Olympus fiber optic light with a 300 Watt Xenon bulb was used as the light source. The light source could be used in conjunction with the borescope to illuminate the interior of the fluidized bed.

3.4.2 Borescope and adapter

A borescope is an optical device consisting of a rigid or flexible tube with an eyepiece on one end and an objective lens on the other linked together by a relay optical system in between. The optical system is usually surrounded by optical fibers used for illumination of the remote object and a rigid or flexible protective outer sheath. Borescopes are generally used for inspection work where the area to be inspected is inaccessible by other means. In this study, an Olympus series-5 rigid tube borecope was used. The borescope tube was 24 cm in length and 8 mm in diameter. A C-mount lens adapter was used to couple the borescope with the high speed camera. Figure 3.5 is the schematic of the experimental set-up.

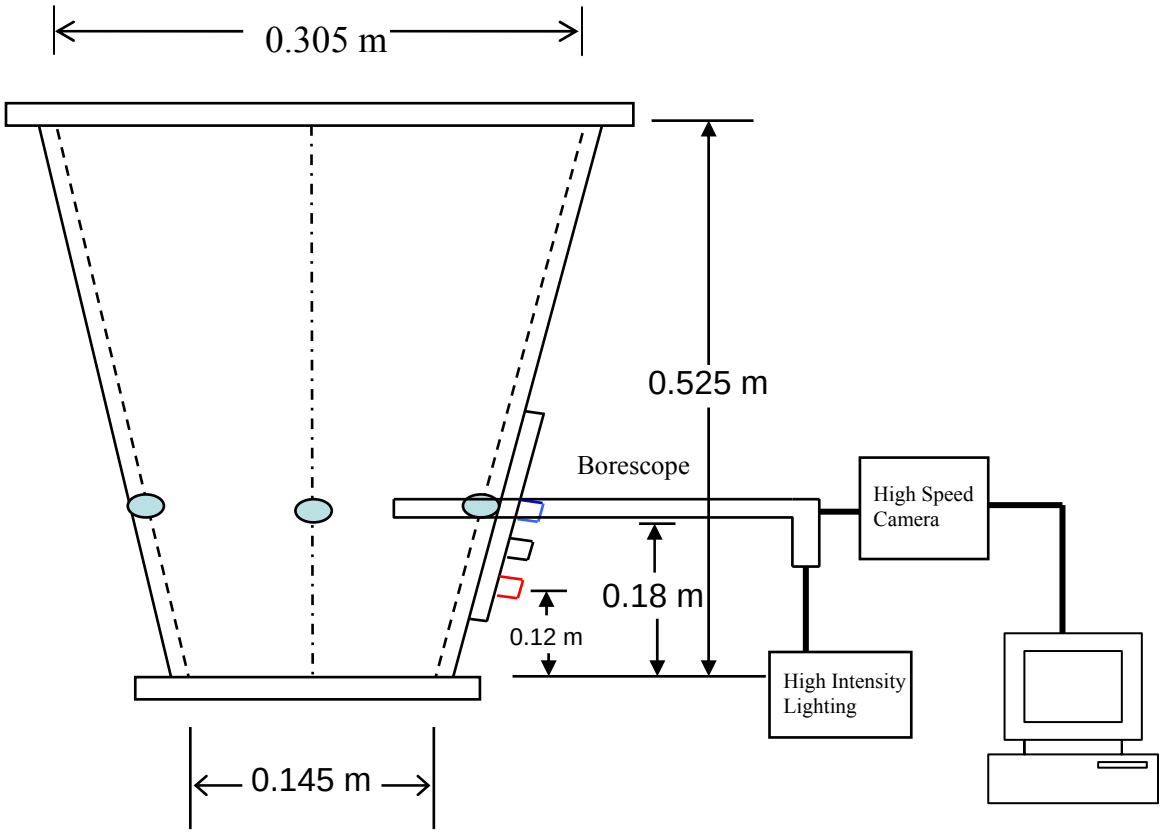

Figure 3.5 Schematic of the experimental set-up for the high speed imaging

3.4.3 Image processing software

Image Pro-Plus version-6 software (Media Cybernetics Inc., Silver Spring, MD, USA) was used to analyze the high speed movies and for performing particle tracking. Image Pro-Plus has the capability to count the number of particles in a single frame and measure the size and surface area of individual particles. It can also track the particles automatically, but due to the high density of particles in a single frame and their random motion, the automatic tracking feature was not useful in the present study. Therefore, particles were tracked manually with the software and their velocities were computed by using an Excel spreadsheet.

3.4.4 Research strategy

Research strategy was based on two principles:

1. Visual observations of particle motion and mixing at different radial and axial locations inside the bed.
2. Manual particle tracking and calculation of particle velocities from the high speed movies.

The borescope was inserted at two axial (12 and 18 cm above the distributor plate) and 3 radial locations (wall-centre-wall) inside the bed. The frame rate of the high speed camera at which movies were recorded was kept constant at 12000 fps due to the trade-off between capture rate and image resolution mentioned earlier. At 12000 fps, the camera was able to record 1 second of continuous motion because of the limitation of installed memory of 2 GB. However, due to the high frame rate of 12000 fps, sufficient data was generated to make it statistically viable. Furthermore, multiple particles were tracked at a given time to increase the sample size and thereby reduce the standard error in mean particle velocities to less than 10 %. Movies were captured at superficial gas velocities of 1.5, 2 and 3 m/s. Two movies both of 1-second duration were captured at each superficial gas velocity to increase the data available for analysis. The static bed height of the bed was kept constant at 12 cm for all experiments.

3.4.5 Test Powders

Three types of powders were used during the experiments: 1) Sugar spheres of 20-25 Mesh (707-841 microns) having a mono-disperse particle size distribution; 2) A 50:50 w/w mixture of 20-25 Mesh and 40-60 Mesh (250-420 microns) sugar spheres; 3) Actual placebo pharmaceutical granulate having wide particle size distribution. The dried

pharmaceutical granule was made in the laboratories of Merck Frosst, Canada using a high shear granulator (Fukae Powtec, model LF-GS-2J) and then dried using a fluidized bed dryer (Glatt GPCG-1). The granulate composition and procedure used for granulation was similar to the one employed at U of S laboratory. The properties of the three test powders are summarized in Table 3.5.

Table 3.5 Properties of test powders

Powder	Mean particle diameter (μm)	Bulk Density (g/ml)	True density (g/ml)
Mono-Disperse	774	0.83	1.56
Mixture	468	0.83	1.56
Placebo	200	0.55	1.56

The particle size distributions were measured using a Sympatec particle size analyzer with HELOS laser diffraction sensor (Sympatec GmbH, Clausthal-Zellerfeld, Germany); the true particle densities were calculated using helium pycnometry (Quantachrome Ultrapycnometer 1000). Each powder was fluidized separately in the Glatt GPCG-1 fluidized bed dryer and two high speed movies were captured at each borescope location at a given superficial gas velocity. It should be emphasized that dry pharmaceutical granule was used for all the experiments.

3.4.6 Software calibration and image analysis

Calibration was performed by measuring the particles of known size range. Sugar spheres having a mono-disperse particle size distribution in the range of 20-25 mesh were fluidized and high speed movies were captured. Calibration of the software was performed by using these high speed movies. During calibration and image analysis, it was observed that large numbers of particles were captured in a single frame, which made it difficult to use the automatic tracking feature of the software. However, some of the particles were in focus and some were out of focus. Therefore, particles which were in sharp focus were considered for calibration (Figure 3.6) and particle tracking. Particle tracking was performed by tracking the particles in sharp focus by following their trajectory in subsequent frames and measuring the distance travelled by them (Figure 3.7). Particle velocities were calculated manually by using an Excel spreadsheet. The standard error in the estimation of particle size and distance travelled by the particles was found to be less than 7 % for particles in sharp focus. However, the error can vary depending on the particles chosen for tracking and as a result, the accuracy of this technique is subjective.

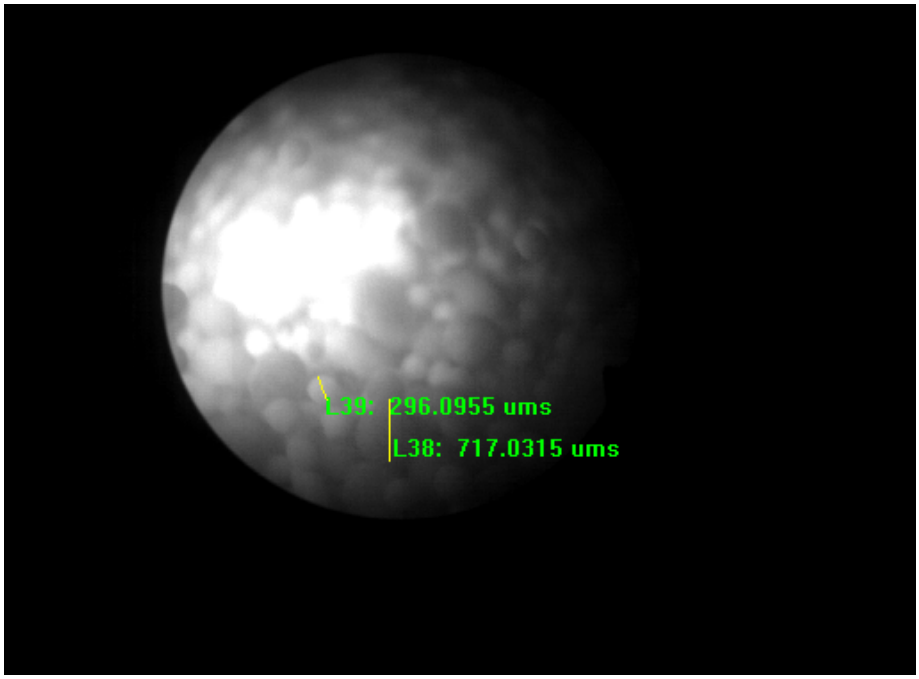

Figure 3.6 Measurement of particle size in the case of 50:50 mixture from high speed movies by using Image Pro-Plus. Lines drawn on the image indicate particle diameter

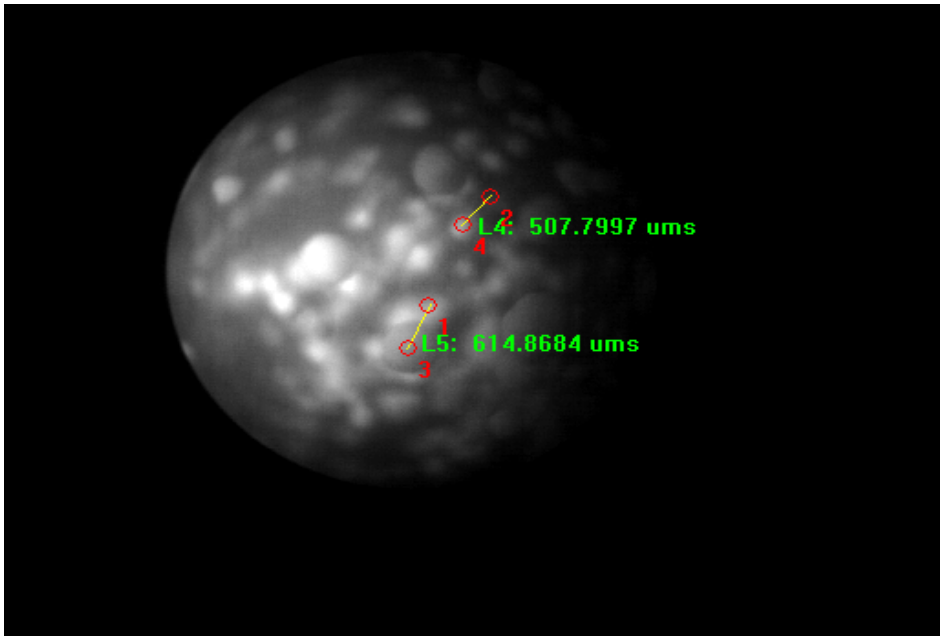

Figure 3.7 Measurement of distance travelled by particles in the case of 50:50 mixture by using Image Pro-Plus software. Lines drawn on the figure indicate distance travelled by the particles

Chapter 4 - Development of Radioactive Particle Tracking System

The application of this RPT technique required determination of total efficiency and photon counts of the detector with respect to particle position. The first step in designing the RPT system was to calculate the efficiency and photon counts of each scintillation detector with respect to the large possible number of tracer positions inside the bed. This was done by using the Monte-Carlo simulation technique. Monte-Carlo simulation is widely used for approximate determination of the value of a multi-dimensional surface integral. This is done by evaluating the integral at a large number of random points. Averaging the value of the integral at each point gives the approximate value of the integral. The application of the Monte-Carlo technique for estimation of the total efficiency of the detectors will be discussed in greater detail in section 4.2.

Once the map of photon counts with respect to each detector was constructed and calibrated, the RPT equipment was used to trace the movement of the tracer particle, wherein, a radioactive tracer particle emitting high energy γ-rays was introduced into the bed and its motion was tracked by the 12 strategically located NaI scintillation detectors. The photon counts were recorded by each detector with respect to time and, by comparing the counts recorded by the detector with the simulated counts from the Monte Carlo method, the position of the tracer was calculated. This information was further used to calculate the local velocities and trajectory of the tracer particle. A least-squares search approach was adopted for the search of the best position of the tracer particle by comparing the measured photon counts to the counts obtained by Monte-Carlo simulation.

4.1 Random point generation inside the vessel

In the RPT system, location of the tracer particle is found by comparing the actual counts with the simulated counts at each of the simulated points inside the vessel. Therefore, the number of points generated inside the vessel is one of the factors in determining the resolution of the RPT system. If the number of points generated is small, the distance between the two points will be large and hence the resolution of the RPT system will suffer. If too many points are generated, it will increase the computational time in finding the location of the tracer. Therefore, a trade-off has to be made between the resolution and computational time. The volume of the vessel used in the present study was similar to the vessel used by Larachi et al. [20]. Therefore, similar to the approach used by Larachi et al. [20], 19,200 random points were generated to simulate a map of γ-ray counts inside the conical vessel. A computer code (Appendix D) was created in C++ to generate coordinates of 19,200 points inside the conical bed using the approach of Larachi et al. [20] (Figure 4.1).

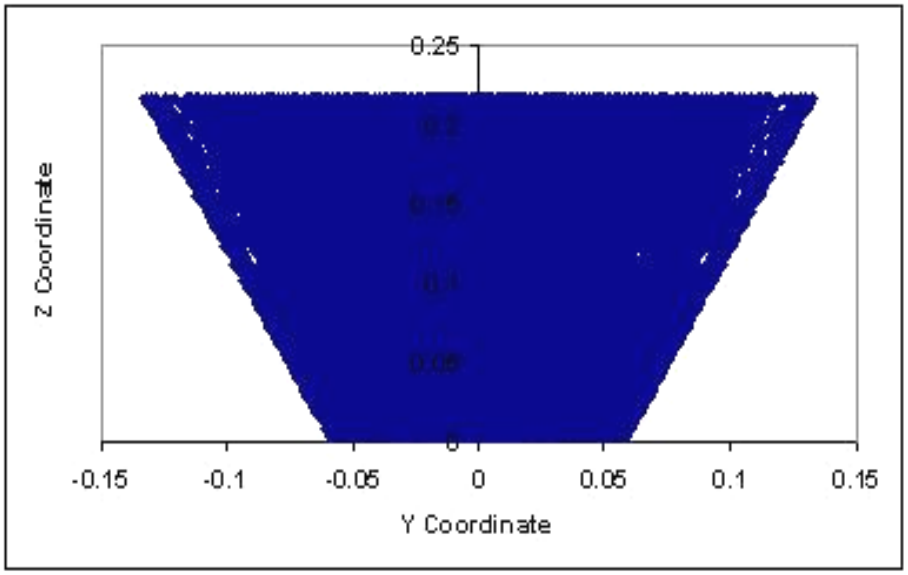

Figure 4.1 Tracer coordinates generated by using method used by Larachi et al. [20]

4.2 Monte-Carlo simulation

The Monte-Carlo simulation technique was used to generate a map of counts *vs.* tracer location for the 19,200 random points throughout the vessel. This served as the basis for the reconstruction of tracer coordinates from the set of counts recorded by multiple detectors situated around the vessel. Once the map of the counts *vs.* tracer location has been constructed, the position of the tracer is found by applying the least squares technique on the counts measured by the detectors and the counts predicted by a Monte Carlo simulation.

When γ-rays of energy less than 1 MeV passes through a dense material, they undergo photoelectric absorption and Compton scattering. As a consequence, their energy spectrum broadens. The fraction of the total γ-rays, that are able to pass unscattered, is called the photopeak fraction. The number of photopeak counts C recorded by a scintillation detector during a sampling time interval T from a point radioactive source of strength A placed at location (x, y, z) without an attenuating media can be expressed by the following relationship [20] (Figure 4.2):

$$C = \frac{T\nu A\phi\varepsilon}{1+\tau\nu A\phi\varepsilon} \tag{1}$$

Where

$$\varepsilon = \iint_{\Omega} \frac{R.n}{R^3}(1-\exp(-\mu_D d))d\sum \tag{2}$$

In the equations (1) and (2), ν is the number of γ-rays emitted per disintegration, Є is the total efficiency (i.e. the probability that γ-rays will emerge from the reactor without scattering and will interact with the detector), τ is the dead-time per recorded pulse and □

is the photopeak to total efficiency ratio. In addition, R is the distance between the source and a point P on the outer surface of the detector crystal and the thickness of the crystal in the direction given by vector R. Ω is the solid angle subtended by the detector surface at the source, and μ_D is the linear attenuation coefficient of the detector material and depends on the γ-ray energy.

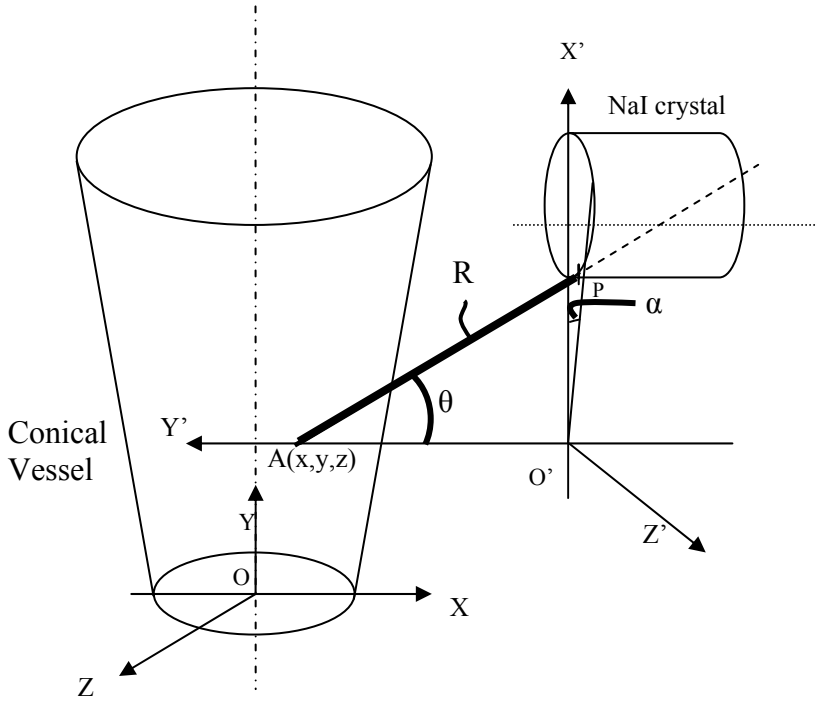

Figure 4.2 Geometrical construction of the path followed by the photon from the source to the detector.

The Monte Carlo treatment consists of following and categorizing a large number of photon histories from emission at the source to absorption within the detector [14]. For each photon emitted from the point source, the probability of it striking the detector and the point where it actually strikes must be known. The former is achieved by calculating

the solid angle Ω subtended by the detector on the point source using the Monte Carlo method. The details for calculating the solid angle and efficiency of the detector for an arbitrarily located isotropic point source were taken from Wielopolski [28] and Beam et al. [29] respectively. The calculation of these two key parameters is described in the next two sections.

4.2.1 Solid angle calculation

The solid angle Ω is a three dimensional angle which can be represented by two dimensional angles α and θ. The surface integral given by equation (2) is evaluated by sampling at random several directions i.e. (α, θ). However all the directions given by (α, θ) are not equivalent, as for some values of (α, θ) the probability of the photon striking the detector is greater than other values. To solve this problem, an appropriate statistical weight ω (α, θ) is assigned to each sampling direction. By assuming isotropic emission, angles α and θ can be sampled independently so that

$$\omega(\alpha, \theta) = \zeta(\alpha)\zeta(\theta). \quad (3)$$

The function ζ(α) is calculated from equations (4) and (5) as follows:

$$\alpha_{max} = \arcsin(r/p)\ ,\ \alpha = \alpha_{max}(2n-1) \text{ (see Figure 4.3)} \quad (4)$$

$$\zeta(\alpha) = \alpha_{max}/\pi \quad (5)$$

The variable n in equation (4) is a random number uniformly distributed between 0 and 1.

For calculating $\zeta(\theta)$, the angles θ, θ_{max}, θ_{min} and θ_{cri} must first be defined as per equations (6) to (9):

$$OB = p\cos\alpha - (r^2 - p^2\sin^2\alpha)^{0.5} \quad (6)$$

$$OA = p\cos\alpha + (r^2 - p^2\sin^2\alpha)^{0.5} \quad (7)$$

When the source is located at a non-axial point (i.e. at S1 in Figure 4.3),

$$\theta_{max} = \arctan(OA/h),\ \theta_{min} = \arctan(OB/(h+L)),\ \theta_{cri} = \arctan(OB/h) \quad (8)$$

$$\theta = \arccos\{\cos(\theta_{min}) - n[\cos(\theta_{min}) - \cos(\theta_{max})]\} \quad (9)$$

Where n is another rectangularly distributed random number between 0 and 1.

The function $\zeta(\theta)$ is calculated from, equation (10).

$$\zeta(\theta) = [\cos(\theta_{min}) - \cos(\theta_{max})]/2 \quad (10)$$

In equations (6) to (10), r is the radius of the detector, h is the distance between the center of the detector face and the source location S1, and p is the distance of the source from the detector axis.

When the source is located at position S3, along the axis of the detector (Figure 4.4), the angle θ_{max} remains constant.

In this case, angle θ is calculated first and angle α is calculated after that. θ_{max} and θ_{cri} are calculated as:

$$\theta_{max} = \arctan [(r + p)/h] \quad (11)$$

$$\theta_{cri} = \arctan [(r-p)/h] \text{ and } \theta_{min} = 0 \quad (12)$$

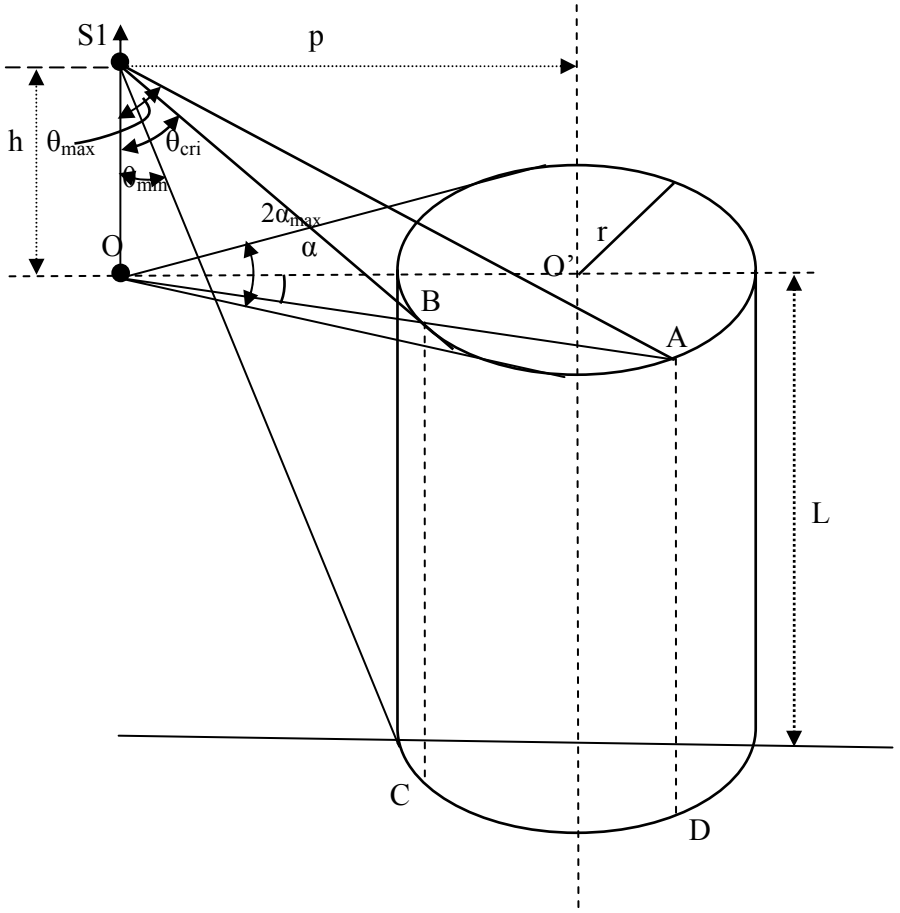

Figure 4.3 Notation in the case of a point source non-axially located at S1

Angle θ is then calculated according to equation (9) and if $\theta > \theta_{cri}$, the angle α varies over 2π and ζ(α) is taken as 1.

For $\theta < \theta_{cri}$, the angle α is restricted to $2\alpha_{max}$ given by:

$$\alpha_{\max} = ar\cos\left[\left(p^2 + h^2\tan^2\theta - r^2\right)/2hp\tan\theta\right] \tag{13}$$

and angle α is calculated from using equation (4).

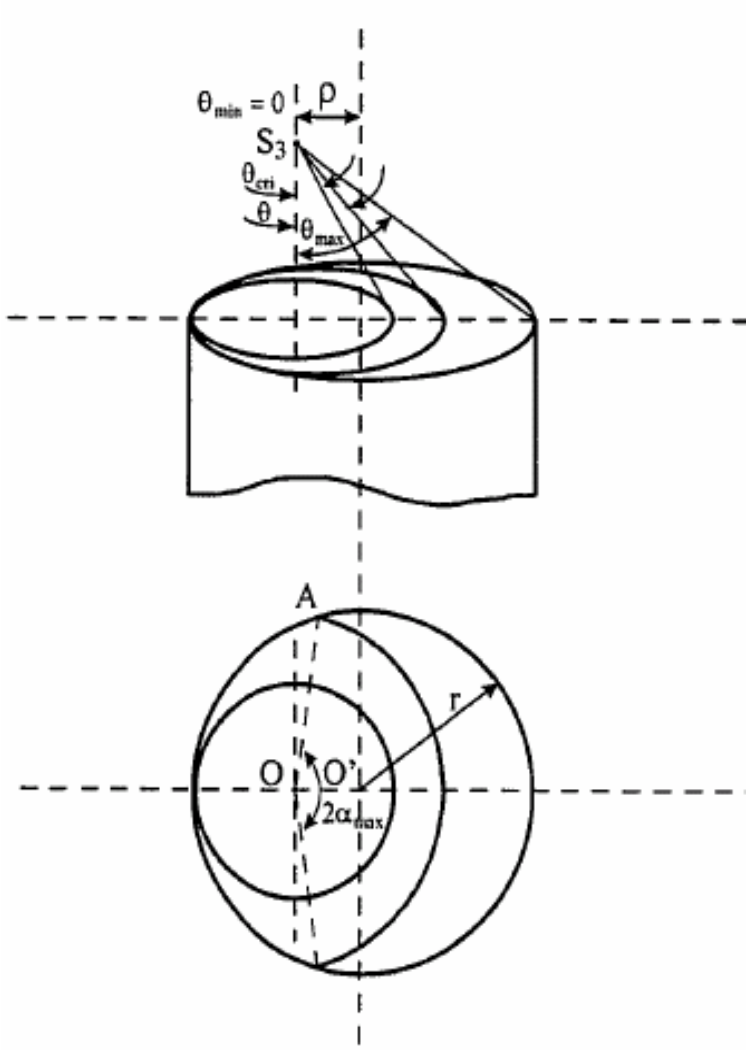

Figure 4.4 Notations when the point source is axially located at point S3 [29]

The total weighting factor for any selection of α and θ is given by:

$W_i = \zeta(\alpha)\, \zeta(\theta)$ (14)

The estimate of the solid angle, Ω is given by the mean value

$$\Omega = \left(\frac{1}{N}\right)\sum_{i=1}^{N} W_i \quad (15)$$

4.2.2 Calculation of detector efficiency

The following factors must be taken into account for the Monte Carlo calculation of the total detection efficiency:

1) The solid angle (Ω) between tracer and detector.
2) The probability $f_a = \exp(-\mu_R e_R(\alpha,\theta) - \mu_w e_w(\alpha,\theta))$ of non-interaction of γ-rays emitted within Ω with the material in the vessel and vessel wall, where $e_r(\alpha, \theta)$ (figure-4.6) and $e_w(\alpha, \theta)$ are the distance traveled by the γ-ray inside the vessel and inside the wall of the vessel respectively. μ_R and μ_w are the attenuation coefficients of the material inside the vessel and vessel wall respectively.
3) The probability $f_D = 1 - \exp(-\mu_D d(\alpha,\theta))$ of interaction of these γ-rays along distance d in the detector crystal, where $d(\alpha, \theta)$ (Figure 4.5) is the distance traveled by the γ-ray inside the scintillation detector and μ_D is the attenuation coefficient of the detector material.

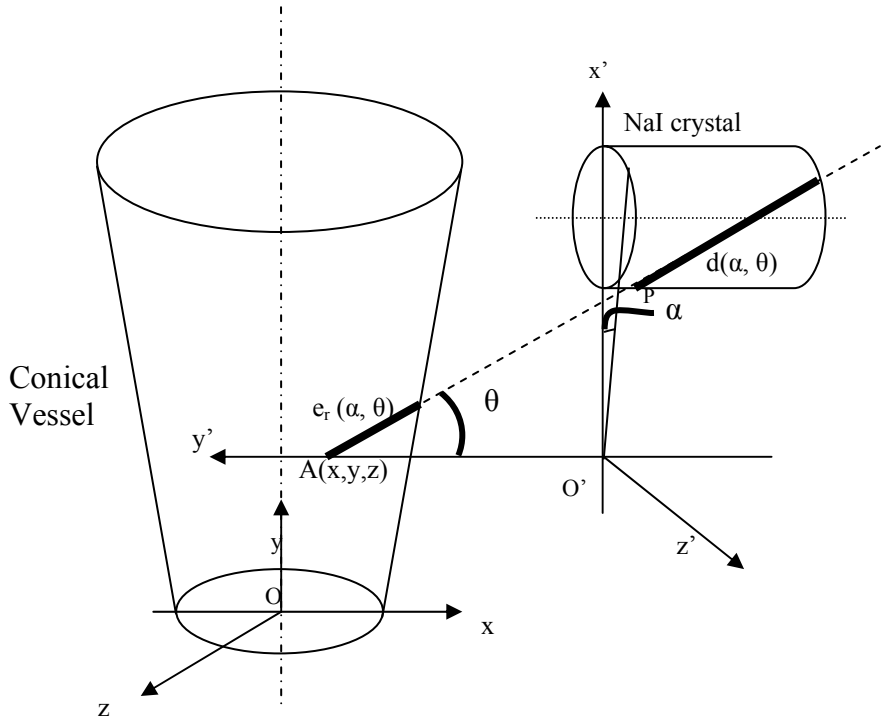

Figure 4.5 Geometrical construction for the determination of the path length e(α,θ) and the effective distance d(α,θ) traveled by the photon in the bed and the detector

After the solid angle has been calculated, the distance (d) traveled by a photon inside the detector must be calculated to determine the probability f_D. To calculate the distance d, the point of entrance to and exit from the detector must be known. Four cases (Figure 4.6) exist for travel of a photon through the detector [14]:

1. The photon may enter from the lateral side and exit from the bottom and the distance d becomes (case1):

$$d(\alpha,\theta) = \frac{p\cos\alpha + \left[(L/2)^2 - p^2\sin^2\alpha\right]^{0.5}}{\sin\theta} - \frac{h}{\cos\theta} \qquad (16)$$

2. The photon may enter from the lateral side and exit from the lateral side; in this case the distance d is (case2):

$$d(\alpha,\theta)=\frac{L}{\cos\theta} \tag{17}$$

3. The photon may enter from the top and exit from the bottom; the distance d is represented by the following formula (case 3):

$$d(\alpha,\theta)=\frac{2\left[(L/2)^2-p^2\sin^2\alpha\right]^{0.5}}{\sin\theta} \tag{18}$$

4. The photon may enter from the top and exit from the lateral side; following formula represents the distance d (case 4):

$$d(\alpha,\theta)=\frac{h+L}{\cos\theta}-\frac{p\cos\alpha-\left[(L/2)^2-p^2\sin^2\alpha\right]^{0.5}}{\sin\theta} \tag{19}$$

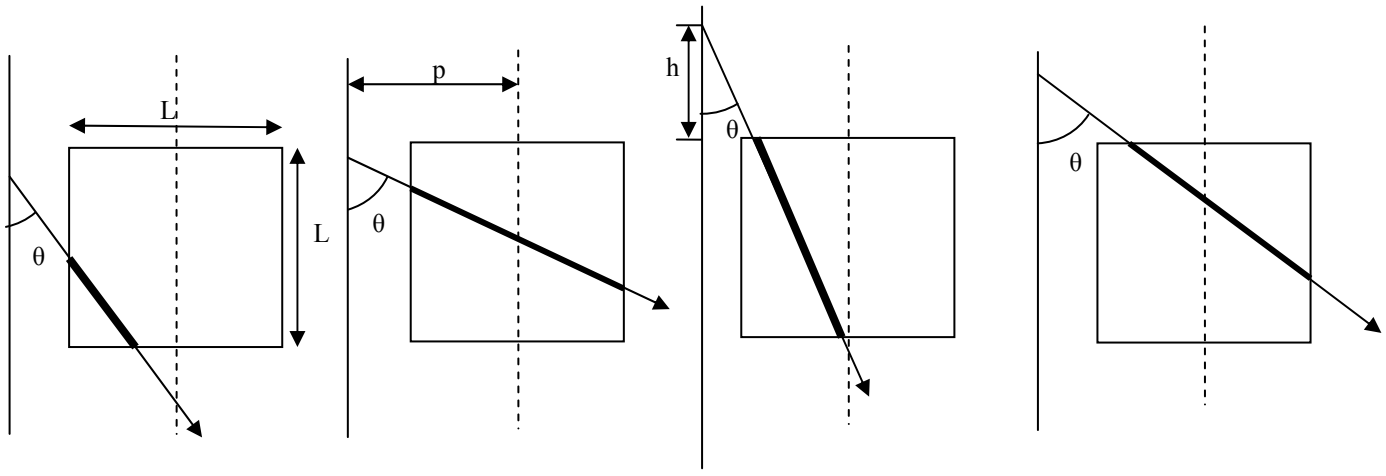

Case 1 **Case 2** **Case 3** **Case 4**

Figure 4.6 The four possible cases of travel of photon through the NaI crystal

Where, L is the length of the detector. If the source is located at point S1 (non-axial position), the above-mentioned cases are evaluated by following conditions [14].

If $\theta_{citical} > \theta$ (see Figure 4.3) the photon enters from the lateral side of the detector. Constants T and N are defined as:

$$T = h(\tan\theta_{\max} - \tan\theta_{critical}) \tag{20}$$

$$N = (h + L)(\tan\theta - \tan\theta_{\min}) \tag{21}$$

If T>N, the photon leaves from the bottom of the detector, otherwise it leaves from the lateral side.

If $\theta_{citical} < \theta$, the photon enters from the top side of the detector. In this case, constants T1 and N1 are defined as:

$$T1 = h\tan\theta_{\max} \tag{22}$$

$$N1 = (h + L)\tan\theta \tag{23}$$

If T1>N1, the photon leaves from the bottom, otherwise it leaves from the lateral side.

When the source is located at S3 (along the axis of the detector) the photon always enters from the top, and the exit point of the photon depends once again on the magnitude of θ compared with $\theta_{critical}$

When $\theta < \theta_{critical}$, the photon always leaves from the bottom. While when $\theta > \theta_{critical}$, the photon may leave from the bottom or from the lateral side of the detector. To calculate the exit point in the latter this case the constants T1 and T2 must be defined as follows:

$$T1 = h \tan\theta_{max} \cos\alpha \tag{24}$$

$$T2 = \arctan\left(\frac{TI}{h+L}\right) \tag{25}$$

When $\theta < T2$, the photon leaves from the bottom and when $\theta > T2$, the photon leaves from the lateral side.

Once it has been determined which of the 4 cases of Figure 4.6 applies, the distance d can easily be calculated using the appropriate equations (16) to (19). W_{i1} represents the probability of the interaction of γ-rays along distance d in the crystal for a particular selection of α and θ

$$W_{i1} = (1 - \exp(-\mu_D d(\alpha,\theta)) \tag{26}$$

For the calculation of distance traveled by the γ-rays inside the vessel, the angles α and θ must be related to the direction cosines of the γ-ray path from the arbitrarily located point source to the entry point of the detector. As the axis of the vessel is perpendicular to the axis of the detector, the transformation and rotation of the coordinate is required. The origin of the initial coordinate system is the center of the bottom of the cone with the x-y plane forming the horizontal cross section of the cone and the z-axis pointing in the

upward direction. For any tracer particle located at position (x_p, y_p, z_p) and the detector located at (x_c, y_c, z_c) outside the vessel, the axis rotation and transformations described in the next section are performed [30].

4.2.3 First coordinate transform

The first coordinate transform is a rotation in the x-y plane by an angle ω' to make the detector axis parallel to the new x'-axis (Figure 4.7)

$$\omega' = \begin{cases} \tan^{-1}\left(\frac{y_c}{x_c}\right) \ldots\ldots\ldots\ldots\ldots\ldots x_c > 0 \\ \frac{\pi}{2} \ldots\ldots\ldots\ldots\ldots\ldots\ldots\ldots\ldots\ldots x_c = 0 \\ \pi + \tan^{-1}\left(\frac{y_c}{x_c}\right) \ldots\ldots\ldots\ldots\ldots\ldots x_c < 0 \end{cases} \quad (27)$$

The particle and detector positions in the new coordinate system are (z coordinate remains the same):

$$x'_p = x_p \cos\omega' + y_p \sin\omega' \qquad y'_p = -x_p \sin\omega' + y_p \cos\omega' \qquad z'_p = z_p \quad (28)$$

$$x'_c = x_c \cos\omega' + y_c \sin\omega' \qquad y'_c = 0 \qquad z'_c = z_c \quad (29)$$

With this transformation in place the distance h between the center of the detector face to the tracer location, and distance p of the tracer from the detector axis (see Figure 4.3) is calculated as:

$$h = \left| x'_c - x'_p \right| \tag{30}$$

$$p = \left[\left(y'_c - y'_p \right)^2 + \left(z'_c - z'_p \right)^2 \right]^{0.5} \tag{31}$$

The equation of the circle describing the inside perimeter of the right circular cone in the horizontal cross section remains the same as the original coordinate system:

$$x'^2 + y'^2 = (z' \tan\theta' + 0.0575)^2 \tag{32}$$

Where (z'tanθ'+0.0575), represents the inner radius of the cone in terms of the height (z-axis) with 0.0575 m being the base radius of the cone. The angle (θ') represents the angle between the z-axis and the slant height of the right circular cone.

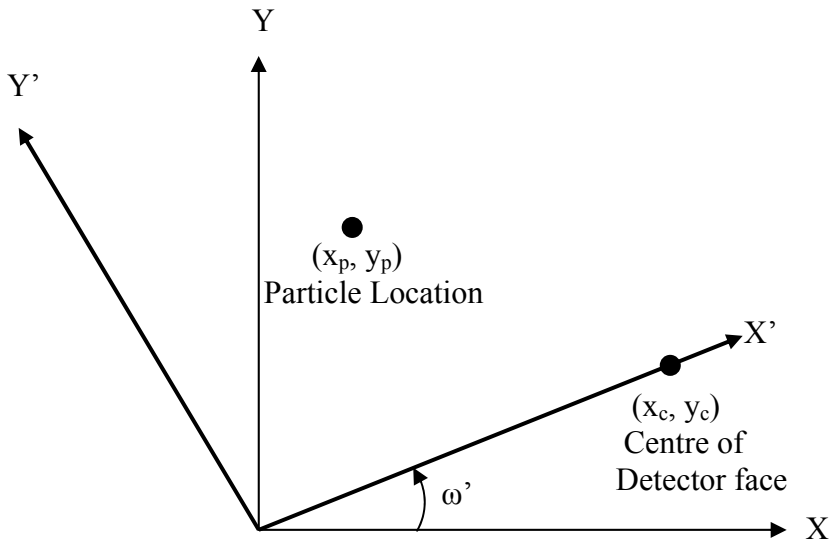

Figure 4.7 First coordinate transform

4.2.4 Second coordinate transform

The second transformation is a rotation of the y-z plane by an angle ω'' to make the new z'' axis parallel to the projection of the 3-D line (x'_p, y'_p, z'_p) to (x'_c, y'_c, z'_c)(Figure 4.8)

$$\omega'' = \begin{cases} \tan^{-1}\left(\dfrac{y'_c - y'_p}{z'_c - z'_p}\right) \ldots\ldots\ldots\ldots\ldots z'_c \neq z'_p \\ \dfrac{\pi}{2} \ldots\ldots\ldots\ldots\ldots\ldots\ldots\ldots\ldots\ldots z'_c = z'_p \end{cases} \tag{33}$$

The particle and detector positions in the new coordinate system are (x' coordinate remains the same):

$$x''_p = x'_p \qquad y''_p = -z'_p \sin\omega'' + y'_p \cos\omega'' \qquad z''_p = z'_p \cos\omega'' + y'_p \sin\omega'' \tag{34}$$

$$x''_c = x'_c \qquad y''_c = -z'_c \sin\omega'' + y'_c \cos\omega'' \qquad z''_c = z'_c \sin\omega'' + y'_c \sin\omega'' \tag{35}$$

The equations of the circle describing the cone perimeter in the new coordinate system are:

$$x''^2 + (z'' \sin\omega'' + y'' \cos\omega'')^2 = (z'' \cos\omega'' - y'' \sin\omega'')^2 \tan^2\theta \tag{36}$$

The y-axis and z-axis change with the rotation of the y-z plane but the angle θ of the cone remains the same.

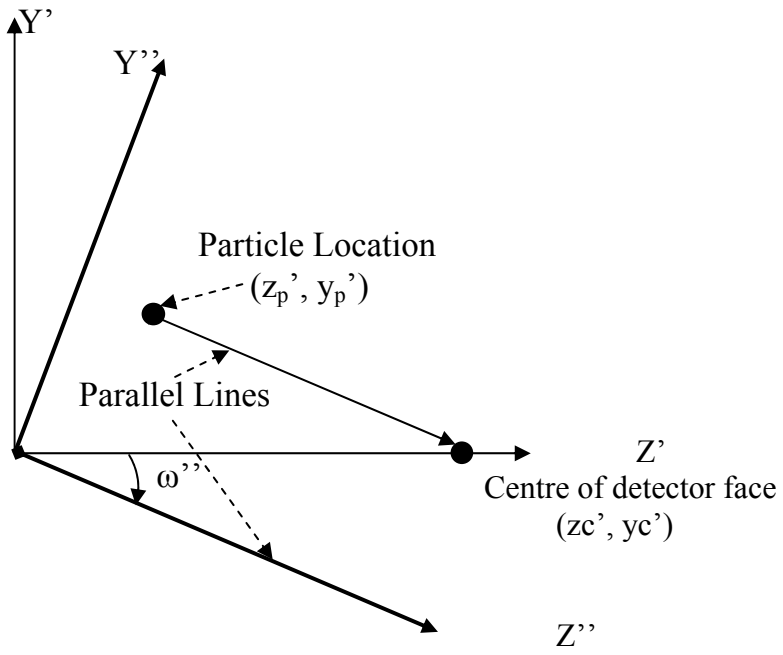

Figure 4.8 Second coordinate transform

The direction cosines (cos α'', cos β'', cos γ'') representing the path of the γ-ray from an arbitrarily isotropic point source to the entry point on the detector can now be related to the chosen angles α and θ as:

$$\cos\alpha'' = \cos\theta_1, \qquad \cos\beta'' = \sin\theta_1 \sin\alpha, \qquad \cos\gamma'' = \sin\theta_1 \cos\alpha \tag{37}$$

$$\text{Where} \quad \theta_1 = \begin{cases} \theta \ldots\ldots\ldots\ldots\ldots\ldots z''_p \le z''_c \\ \pi - \theta \ldots\ldots\ldots\ldots\ldots\ldots z''_p > z''_c \end{cases} \tag{38}$$

Hence, the equation of the line from the point source to the point of γ-ray entry into the detector for a particular choice of α and θ becomes:

$$x'' = x''_p + t\cos\alpha'' \qquad y'' = y''_p + t\cos\beta'' \qquad z'' = z''_p + t\cos\gamma'' \tag{39}$$

Where, t is the parameter defining the line in 3-D space.

These equations are solved along with the circle equation for the cone to obtain the intersection of the line with the cone. Substitution of these equations (39) into circle equation (36) leads to a quadratic equation in t and is given by:

$$t^2\left(\begin{array}{l}\cos^2\alpha''+\cos^2\gamma''\sin^2\omega''+\cos^2\beta''\cos^2\omega''+2\cos\beta''\cos\gamma''-\cos^2\gamma''\cos^2\omega''\tan^2\theta'-\\ \cos^2\beta''\sin^2\omega''\tan^2\theta'+2\cos\gamma''\cos\beta''\cos\omega''\sin\omega''\tan^2\theta'\end{array}\right)$$

+

$$t\left(\begin{array}{l}2x_p\cos\alpha+2z_p\cos\gamma\sin^2\omega''+2y_p\cos\beta''\cos^2\omega''+2y_p\cos\gamma''+2z_p\cos\beta''-\\ 2z_p\cos\gamma''\cos^2\omega''\tan^2\theta'-2y_p\cos\beta''\sin^2\omega''\tan^2\theta'+2z_p\cos\beta''\cos\omega''\sin\omega''\tan^2\theta'+\\ 2y_p\cos\gamma''\cos\omega''\sin\omega''\tan^2\theta'-0.115\cos\omega''\cos\gamma''\tan\theta'+0.115\cos\beta''\sin\omega''\tan\theta'\end{array}\right)$$

+

$$\left(\begin{array}{l}x_p^2+z_p^2\sin^2\omega''+y_p^2\cos^2\omega''+2y_pz_p\sin\omega\cos\omega-z_p^2\cos^2\omega''\tan^2\theta'-y_p^2\sin^2\omega''\tan^2\theta'\\ +2y_pz_p\cos\omega''\sin\omega''\tan^2\theta'-0.00331-0.115z_p\cos\omega''\tan\theta'+0.115y_p\sin\omega''\tan\theta'\end{array}\right)$$

$$=0 \tag{40}$$

By solving this equation for t, the intersection point of 3-D line representing the path of γ-ray with the circle describing the perimeter of the right circular cone can be evaluated (by using equation (40).

The distance traveled by the γ-ray through the media inside the cone, d_r is calculated from the source position and the intersection point:

$$d_r = \left[\left(x''_p - x''\right)^2 + \left(y''_p - y''\right)^2 + \left(z''_p - z''\right)^2\right]^{0.5} \tag{41}$$

There are two intersection points for each circle equation. The one close to the detector is the true solution, whereas the other one is discarded. This is done by calculating the distance d_r in each case and then choosing the larger one.

The distance d_w is calculated by modifying the equation of circle representing the perimeter of the right circular cone.

Once the distances d_r and d_w are known the probability factor f_a is calculated as:

$$f_a = \exp(-\mu_R d_R(\alpha,\theta) - \mu_w d_w(\alpha,\theta)) \tag{42}$$

Values of μ_w and μ_D were obtained from literature [31] to be 5 and 3.5 m^{-1} respectively, value of μ_R was assumed to be 5 m^{-1} for all the detectors for initial calculations. Total efficiency is calculated by taking the average value of the product for all the sampled directions [20]:

$$\varepsilon = \frac{1}{N}\sum_{1}^{N} \zeta(\alpha)\zeta(\theta) f_D(\alpha,\theta) f_a(\alpha,\theta) \tag{43}$$

Once the efficiency of the detectors at each point in the vessel was calculated, the counts recorded were calculated using equation (1). Photopeak to total efficiency ratio for NaI

crystals was calculated using the method given by Cesana et al. [32] and τ was assumed to be 3 μs for all the detectors. However, the actual value of the attenuation coefficient was determined during the calibration of the RPT system.

For each detector, the Monte-Carlo calculation was performed for 19,200 locations inside the vessel: for 60 values of axial coordinate z, 8 radii and 40 azimuthal angles [20]. A computer code was created in C++ programming language (Appendix E) to calculate the total counts for each detector for the above mentioned tracer locations inside the bed, in the presence of an attenuating media.

4.3 Strength of the radioactive tracer particle

During the calculation of the simulated counts by the Monte-Carlo method, the strength of the radioactive tracer was assumed to be 100 μCi. However, due to the small size of tracer particle, it was very difficult to accurately estimate the amount of gold present in the tracer particle. The error in the estimation in the quantity to gold would have led to error in the calculation of irradiation time in the Slow Poke nuclear reactor. Therefore, it was difficult to accurately produce a tracer particle of a given strength. To solve this problem, a novel technique was employed whereby the counts recorded by each detector were normalized with respect to the total number of counts recorded by all the 12 detectors. This was done for both the simulated counts C_i and measured counts M_i:

$$C_i = \frac{c_i}{\sum_{i=1}^{n} c_i} \tag{44}$$

$$M_i = \frac{m_i}{\sum_{i=1}^{n} m_i} \tag{45}$$

Where c_i is the calculated count for detector i, C_i is the calculated count for detector i with respect to total counts recorded by all the detectors when tracer particle is present at a given point, m_i is the measured count for detector i, M_i is the measured count for detector i with respect to the measured counts recorded by all the detectors and n is the total number of detectors. A computer code was written in C++ to perform this calculation (Appendix F).

4.4 Reverse construction algorithm

Once the map of anticipated number of counts for each scintillation detector for every point inside the bed was accurately calculated by Monte-Carlo simulation and the problem of accurately determining the strength of the tracer particle was solved, a reverse construction algorithm was needed to locate the exact position of the tracer particle during the actual experiment by comparing the actual counts recorded by each detector during an experiment with the simulated counts inside the vessel.

Photon counts recorded by each detector represents that the tracer particle is located on an isocount spherical shell but the shell is distorted because of the attenuation of the material in the vessel and anisotropicity of the detector. Ideally, the exact location of the tracer could be the intersection point of these shells and therefore, three detectors can accurately determine the position of the tracer. However, due to the distortion of the isocount shell and statistical fluctuations in the counts recorded by the detectors in an

actual experiment, large number of detectors is needed to accurately locate the tracer particle from the counts data.

A least square approach was used for the search of the best tracer position by comparing the measured counts with the counts calculated by Monte-Carlo simulation for each point inside the vessel. The point which minimizes χ^2 is chosen as the location of the tracer particle [20]

$$\chi^2 = \sum_{i=1}^{n} \frac{(C_i - M_i)^2}{\sigma_i^2} \tag{46}$$

Where C_i is the calculated count for detector i with respect to counts recorded by all the detectors, M_i is the measured count for detector i with respect to counts recorded by all the other detectors, n is the total number of detectors and σ_i is the statistical uncertainty or the standard-deviation given by the square-root of C_i.

A computer code was written in C++ programming language (Appendix H) which compared the counts recorded by each detector interval with the counts calculated at 19,200 points inside the vessel to find the location of the tracer particle. 12 scintillation detectors were utilized in one RPT experiment; therefore, 230,400 calculations had to be performed to calculate one position of the tracer particle.

Table 4.1 Dead time and attenuation coefficients of scintillation detectors

Detector Number	τ (μs)	μ_R (m^{-1})
1	3.1	4.9
2	2.9	6.3
3	2.8	5.6
4	3.2	6.5
5	3.1	5.3
6	2.7	4.1
7	3.0	4.8
8	3.1	6.3
9	3.3	4.8
10	2.9	5.6
11	2.8	6.4
12	3.0	7.0

4.5 Calibration of the RPT system and determination of attenuation coefficient

The RPT system was calibrated to estimate the value of attenuation coefficient μ_R and dead time (τ) for each detector to improve the accuracy of the RPT system. Calibration was performed by manually placing a radioactive tracer particle at 14 known locations inside the vessel. The bed containing dry pharmaceutical granule was fluidized at a superficial gas velocity of 2 m/s so that the fluctuation in media density during calibration matches closely with the media density fluctuations during an actual experiment. The static bed height was kept constant at 12 cm.

Subsequently, location of the particle was calculated by reverse construction algorithm. At every known location, a new value of μ_R and τ was selected to minimize the difference between simulated counts and actual counts. Due to the change in the density of the media inside the vessel, the attenuation coefficient of the reactor material μ_R kept on changing inside the bed. The values of μ_R and τ at all the 14 locations were averaged to calculate the final value of μ_R and τ for each detector. The mean values of μ_R and τ for each detector are given in table 4.1.

The simulated counts for each detector for 19,200 points inside the vessel were calculated again using the new values of μ_R and τ. The static bed height was held constant at 12 cm for all the dry bed studies, furthermore, the static bed height of wet bed at the end of drying was 12 cm and the density of placebo granule and water were very similar. Also, it was observed that due to large number of detectors used in the study, a small change in attenuation coefficient of the reactor material did not affect the results significantly. Therefore, μ_R was assumed to be constant for each detector for all the dry bed as well as wet bed studies.

Chapter 5 Results and Discussions for Radioactive Particle Tracking System

This chapter presents the results of the experiments performed by using the radioactive particle tracking system. The chapter starts with a discussion of the accuracy and resolution of the newly developed RPT system. This is followed by the results of particle tracking experiments performed in the U of S labs. The radioactive particle tracking experiments are divided into two sections. The first section presents the results of dry bed studies involving the use of dry pharmaceutical granule, while the second section presents the results of wet bed studies involving the use of wet pharmaceutical granule that is dried during particle tracking experiments. In both dry and wet bed studies, two important aspects of the particulate phase were discussed. First is the circulation pattern of the particulate phase and the second is particle segregation. Furthermore, the effect of particle size distribution (PSD), tracer size and superficial gas velocity on particle segregation is also discussed.

5.1 Spatial resolution of radioactive particle tracking system

γ-ray emission is a statistical process that follows Poisson statistics. In addition there are local density fluctuations that are inherent in any fluidized bed which can introduce uncertainty into the values of tracer position measured by the RPT system. Furthermore, error can also be propagated through algorithm computation. In order to determine the accuracy and resolution of RPT system, tests were conducted wherein a tracer particle was placed at 20 known axial and radial locations as depicted in Figures 5.1a and 5.1b. At each known location, counts were repeatedly measured 1000 times by all the detectors at 30 ms intervals.

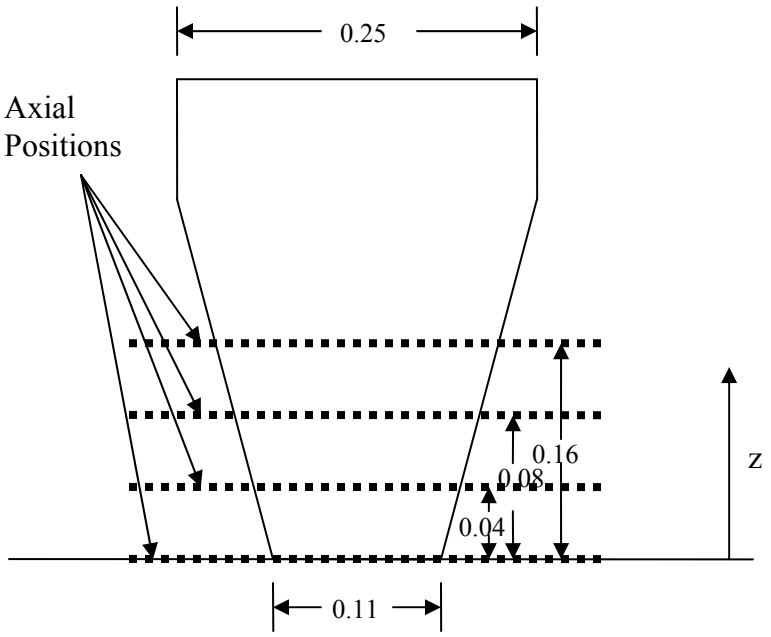

Figure 5.1 (a) Axial positions of the known locations of tracer particle inside the conical fluidized bed used for determining the resolution of RPT system

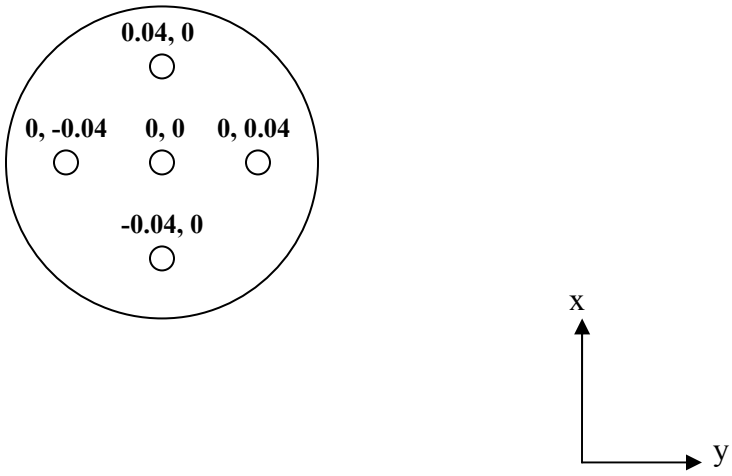

Figure 5.1 (b) Radial positions of the known locations of the tracer particle inside the conical fluidized bed used for determining the resolution of RPT system

The reverse construction algorithm described in section 4.4 was used to find the apparent position of the tracer particle inside the bed. Statistical analysis was conducted

by comparing the apparent position of the tracer particle with the true tracer position and the standard deviation (or resolution) was computed for the x, y and z axes. It was observed that the radial resolution (x and y axis) of the RPT system was better than the axial (z axis) resolution. The three-dimensional standard deviation was given by:

$$\sigma = \left(\sigma_x^2 + \sigma_y^2 + \sigma_z^2\right)^{\frac{1}{2}} \tag{47}$$

In all cases, the three-dimensional standard deviation was dominated by the standard deviation σ_z which was found to be 8 mm. The value of σ_x and σ_y was found to be 3 mm. The three-dimensional standard deviation was found to be 9 mm. Regarding the accuracy of particle velocity measurements, RPT experiments were conducted at superficial gas velocities of 1.5, 2 and 2.5 m/s, therefore, the average tracer velocity was expected to be around 1 m/s. Furthermore, the location of the tracer was determined every 30 ms. At 1m/s, the tracer would travel 30 mm in 30 ms time interval. Since the three-dimensional standard deviation was found to be 9mm, it was concluded that the tracer could be tracked with reasonable accuracy using the present RPT system. Recommendations for improving the resolution of the RPT system are presented in chapter-7.

5.2 Dry bed studies

In both the dry bed and wet bed studies, the position of the tracer particle was determined every 30 ms. The 30 ms interval was sufficient to track fast moving tracer particles with a resolution of 9 mm. A dry bed run using a given tracer particle lasted 2 hours with RPT data collected for 30 minutes at a given superficial gas velocity to achieve good statistical relevance. The RPT data was analyzed for gaining better

knowledge of particle mixing and overall particle motion. It is important to note that as particle location was determined after every 30 ms, therefore, 30 minutes of particle tracking at a given superficial gas velocity in the case of dry bed studies produced 60,000 successive tracer locations.

5.2.1 Particle circulation

Axial and radial velocities were extracted from the RPT data in order to gain qualitative information on the solid circulation patterns in the dry bed. It is challenging to present the complex axial and radial flow patterns of tracer in two-dimensional graphs. Therefore, in this work, a novel approach was taken whereby the axial and radial movement of the tracer was analyzed at both the macroscopic and microscopic scales. In the macroscopic scale, the bed volume was divided into small cubes of 1 cm on a side. This was accomplished by dividing the entire bed into vertical planes of 1 cm thickness and starting from the centre, each vertical plane was further divided into radial cross sections of 1 cm each (Figure 5.2). Axial and radial velocities in each radial cross section in each axial plane were time averaged over the entire run at a given superficial gas velocity. These average axial and radial velocities were plotted against the radial distance ‘r’ and axial height ‘z’ to represent the circulation of the particulate phase. A computer algorithm was written in C++ programming language to process the data.

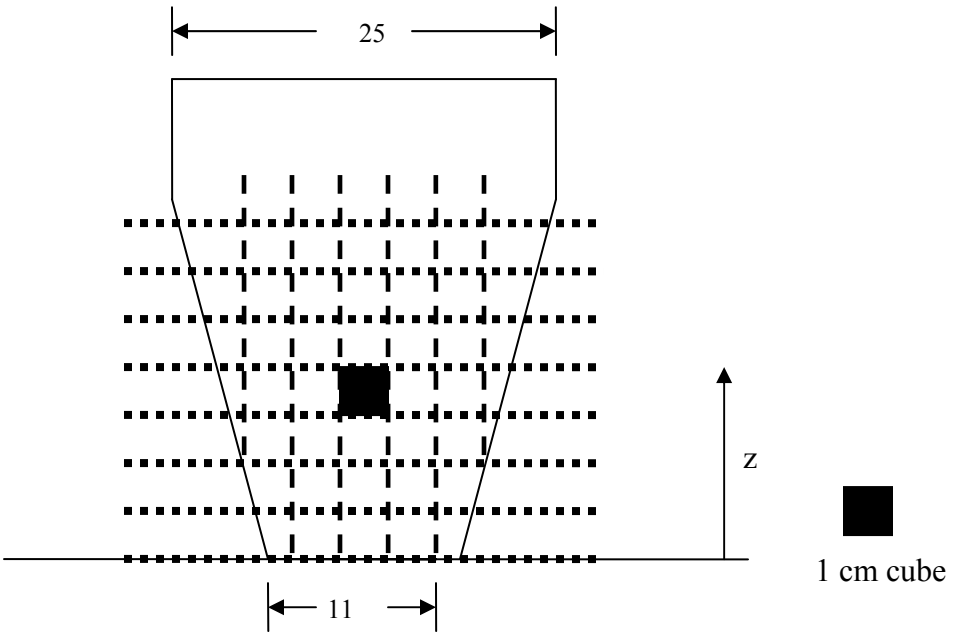

Figure 5.2 Division of entire volume of the fluidized bed dryer into small cubes having side of 1 cm for calculation of average axial and radial velocities of the tracer

The first set of experiments was performed with pharmaceutical granule having narrow PSD. Figure 5.3 shows the circulation pattern of the particulate phase for a 1.33 mm tracer particle at a superficial gas velocity of 2.5 m/s. It is evident from the vector plot that there is a distinct pattern of particle circulation with particles moving up at high velocities near the centre of the bed and slowly moving downward near the wall. This circulation pattern is consistent with the circulation pattern proposed by Tanfara et al. (2002). When the particle reaches the bottom of the bed, it moves slowly towards the centre before moving upwards again at high velocities. Therefore, the tracer particle spends some time sitting at the bottom of the bed before starting its upward journey again. It is interesting to note that this circulation pattern is similar to that of spouted beds. However, ECT observations of Tanfara et al. (2002) and Wiens et al. (2006) revealed the presence of bubbles, which are a characteristic of bubbling fluidized beds.

The conical geometry is the reason behind this observed particle circulation behaviour. Gas that is introduced at the base of the bed will decelerate as the cross-sectional area expands. This feature of the bed is desirable because the higher velocity near the bottom helps to "turn over" wet granule when the bed is operated as a dryer, while the reduced velocity near the top of the bed minimizes entrainment. This deceleration of the gas sets up the observed internal circulation pattern of the granule as particles that are dragged upward by the high-velocity gas near the base are shed toward the vessel walls as the gas slows down and the drag of the gas on the particles is correspondingly reduced. In addition, the tomography work of Wiens et al. (2006) identified bubbling splitting as the predominant mechanism at gas velocities above 2.5 m/s. They also identified "knifing" of the bubbles by the downward-raining solids as the precursor to bubble splitting. This is consistent with the observed downward motion of granule near the centre of the bed in Figure 5.3.

Figure 5.3 is a qualitative representation of the particle circulation and as the tracer particle moves randomly in all the directions, it is difficult to estimate the magnitude of the instantaneous axial and radial velocities from the mean values presented in the figure. In order to provide a quantitative picture of the particle motion, the axial and radial velocities were plotted and compared with the instantaneous axial and radial locations of the tracer inside the bed.

Figure 5.4 represents the axial and radial position of the tracer inside the bed and Figures 5.5 and 5.6 represent the instantaneous axial and radial velocities, respectively of the 1.33 mm tracer particle at a superficial gas velocity of 2.5 m/s.

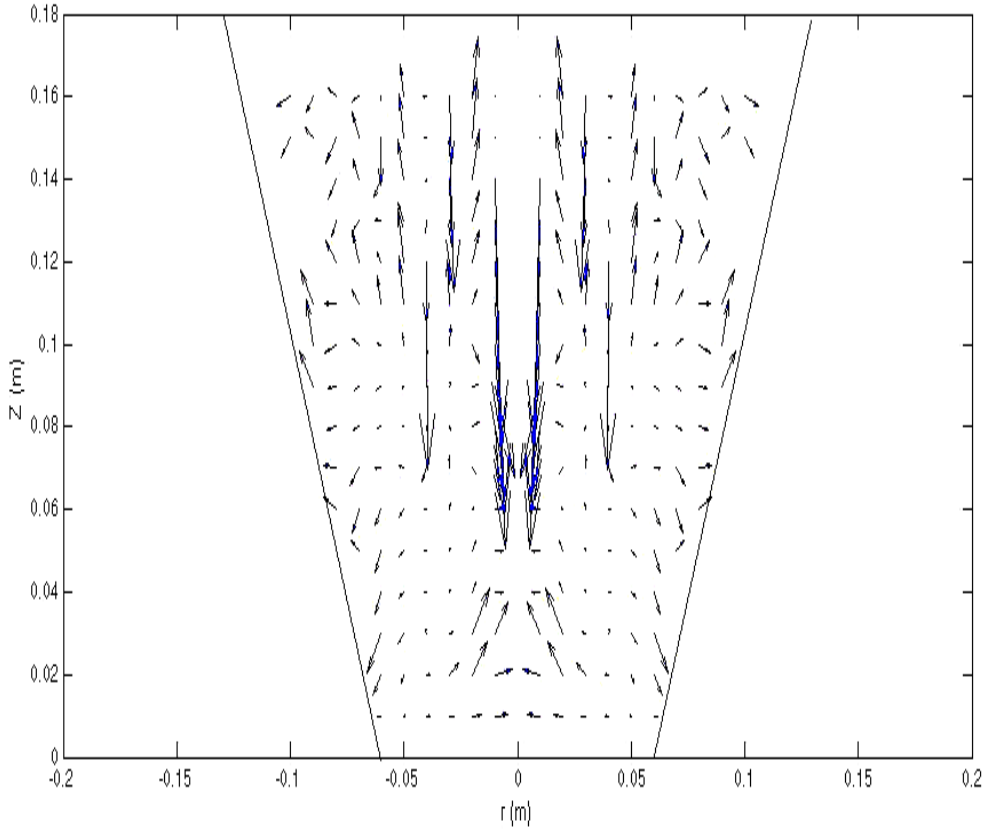

Figure 5.3 Vector plot of the axial and radial velocities depicting circulation of the particulate phase using a 1.33 mm tracer at a superficial gas velocity of 2.5 m/s, 'z' represents the axial height and 'r' represents the radial distance from the axis (centre) of the vessel

Referring to Figure 5.4, the radial and axial positions tend to follow each other, with the axial position of the tracer particle increasing as the radial distance from the centre increases. Furthermore, the upward motion of the particle usually takes place when its radial distance from the centre is less than 4 cm, which provides an indication of the radius of the centralized region of gas flow. This observation is consistent with the circulation pattern depicted in Figure 5.3. Interestingly, it is evident from Figure 5.5 that when the tracer's radial position is near the centre of the vessel and its axial position is near the bottom, it experiences the maximum fluctuation in axial velocity. This suggests that, although the particle rises up when it is near the centre of the bed, particle motion is

very random in nature due to inter-particle and gas-particle interactions. This phenomenon repeats twice in the data presented below and generally speaking this is consistent across all the data for both tracer sizes. The effect of this phenomenon is also evident in the vector plot of Figure 5.3 where the tracer experiences rapid rise or fall when it is near the centre of the bed.

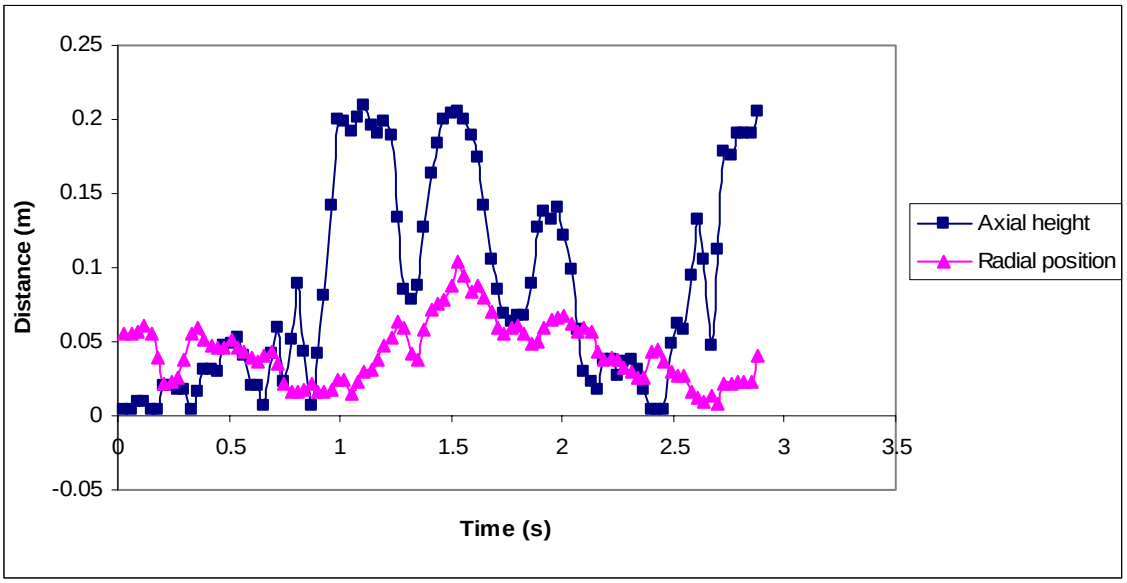

Figure 5.4 Instantaneous axial height and radial position plot of 1.33 mm tracer at superficial gas velocity of 2.5 m/s in the case of narrow PSD

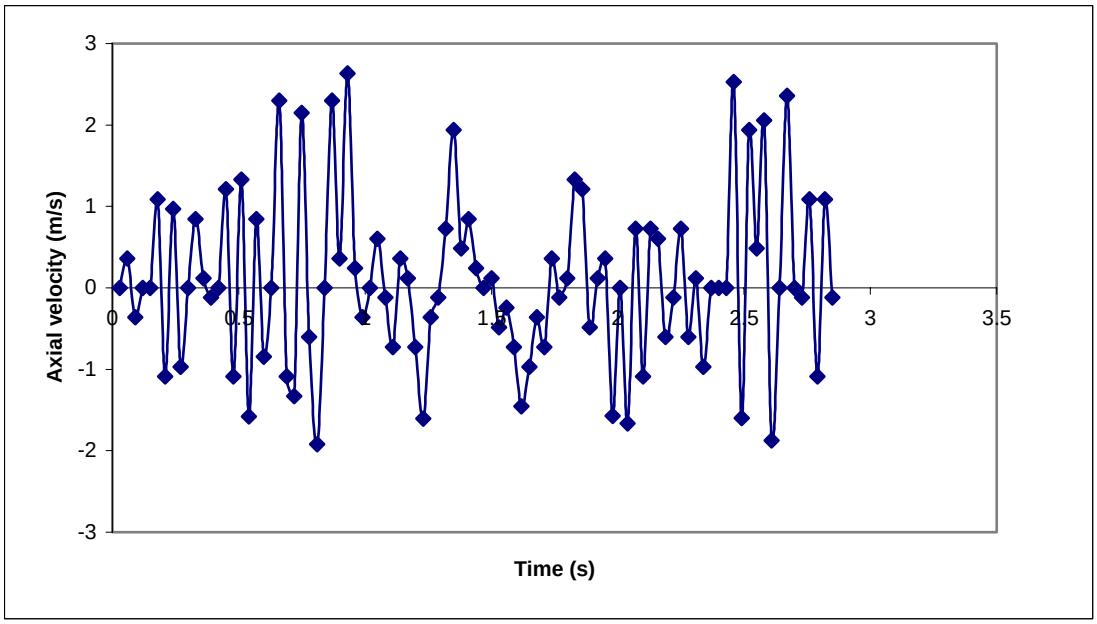

Figure 5.5 Instantaneous **a**xial velocity plot of 1.33 mm tracer at superficial gas velocity of 2.5 m/s in the case of narrow PSD

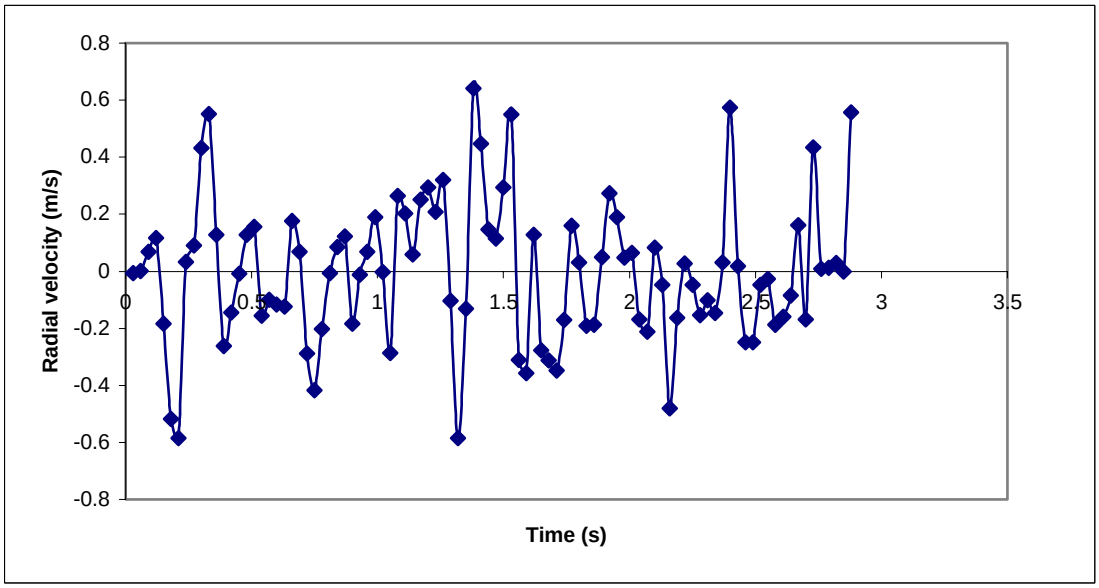

Figure 5.6 Radial velocity plot of 1.33 mm tracer at superficial gas velocity of 2.5 m/s in the case of narrow PSD

A second set of experiments was performed with pharmaceutical granule having wide PSD. Two tracers of 2.60 and 1.80 mm were tracked. Figure 5.7 shows the circulation pattern of the particulate phase for the 1.80 mm tracer at a superficial gas

velocity of 2.5 m/s. Figure 5.7 illustrates that similar to the narrow PSD, there is a well defined circulation pattern inside the bed with tracer moving upward near the centre of the bed and flowing downward near the walls. However, it can be observed that unlike Figure 5.3, the vector plot of figure 5.7 is almost cylindrical in shape, which shows that tracer did not circulate through the entire bed cross section near the top of the bed. Furthermore, the tracer did not enter in the freeboard region above the static bed height of 12 cm, suggesting that the tracer experienced higher resistance in its path to the top of the bed and was therefore ejected at a lower velocity from the upper surface of the bed. This poor circulation was seen in both the tracers and at all the superficial gas velocities.

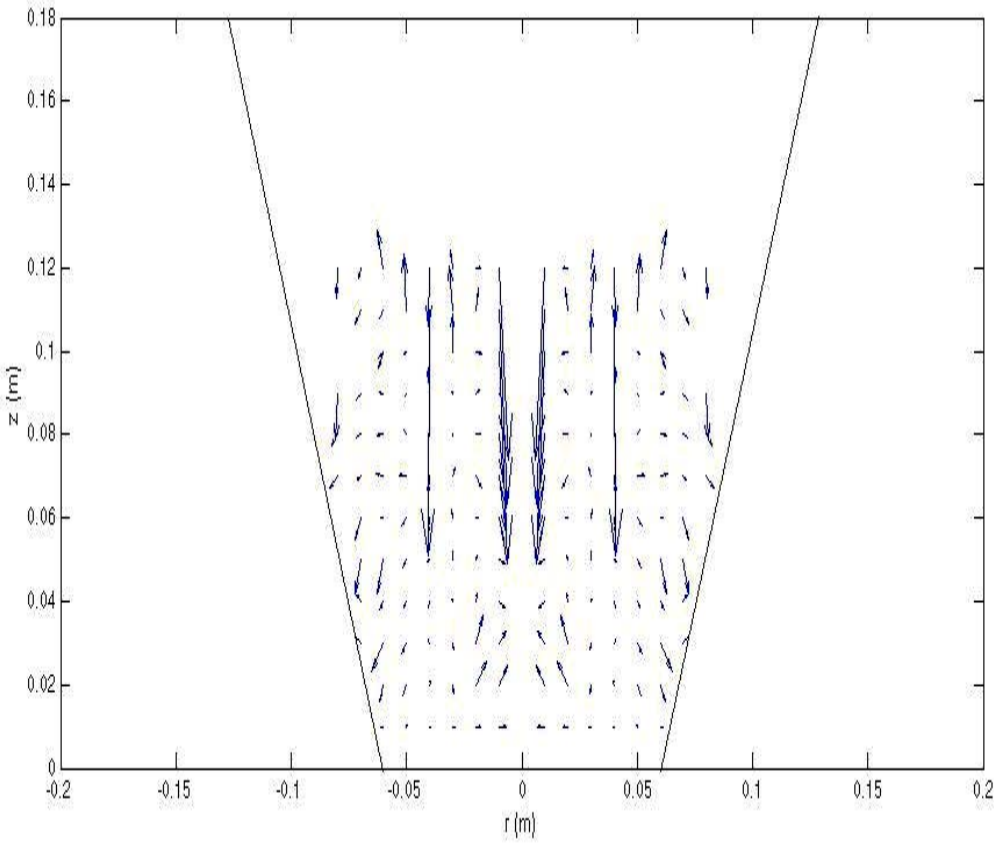

Figure 5.7 Vector plot of the axial and radial velocities depicting circulation of the particulate phase using a 1.80 mm tracer at a superficial gas velocity of 2.5 m/s, 'z' represents the axial height and 'r' represents the radial distance from the axis (centre) of the vessel

Similar to the narrow PSD, the axial and radial velocities were plotted and compared with the instantaneous axial and radial locations of the tracer inside the bed. Figure 5.8 represents the axial and radial position of the tracer inside the bed and Figures 5.9 and 5.10 represents the instantaneous axial and radial velocities, respectively of the 1.80 mm tracer particle at superficial gas velocity of 2.5 m/s. Figure 5.8 shows that similar to narrow PSD, the radial and axial position generally follow each other, with an increase in axial height corresponding to an increase in the radial distance and vice versa. Furthermore, the fluctuation in axial velocity and axial height increases when the tracer is near the centre of the bed. This shows that the circulation pattern of the particulate phase in the case of broad PSD is similar to the one observed in narrow PSD with increased gas flux at the centre of the bed. However, it can be observed from Figure 5.9 that although, in the time between 1 and 2 seconds, the tracer is close to the bottom centre of the bed, its axial velocity remains very low. This results in the tracer spending a lot of time in the bottom section of the bed as compared to the narrow PSD case where the particle spends a considerable amount of time in upper sections as well. It appears as if the tracer gets "stuck" in the bottom region of the bed. This may be due to the presence of large particles in the bed material leading to increased collision frequency between bigger particles. This will break the momentum of the particles and result in their poor circulation. Furthermore, the tracer is never able to leave the dense bed and enter into the freeboard region, which is further evidence of a loss of vertical momentum of particles.

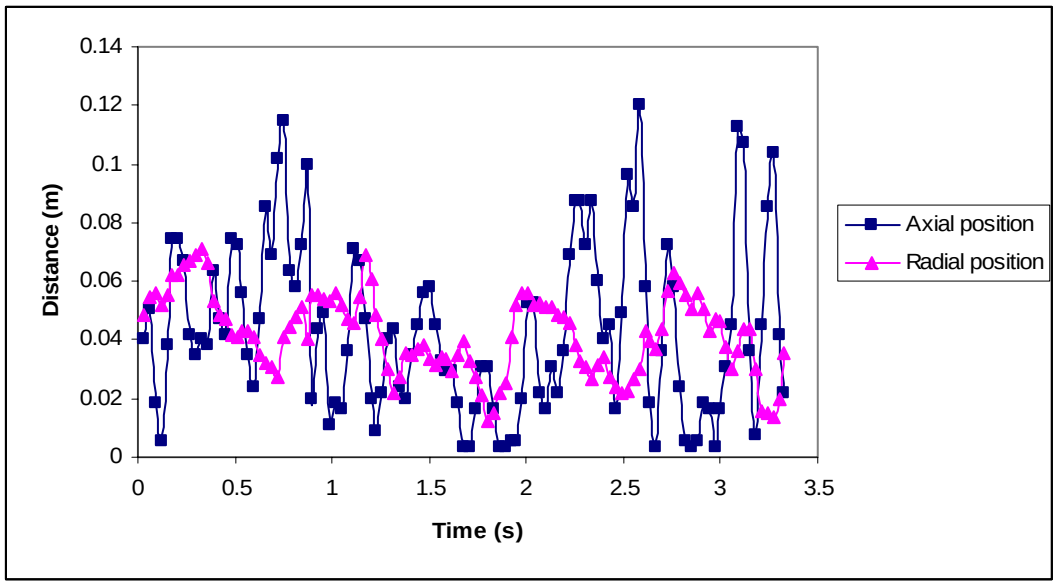

Figure 5.8 Instantaneous axial height and radial position plot of 1.80 mm tracer at superficial gas velocity of 2.5 m/s in the case of broad PSD

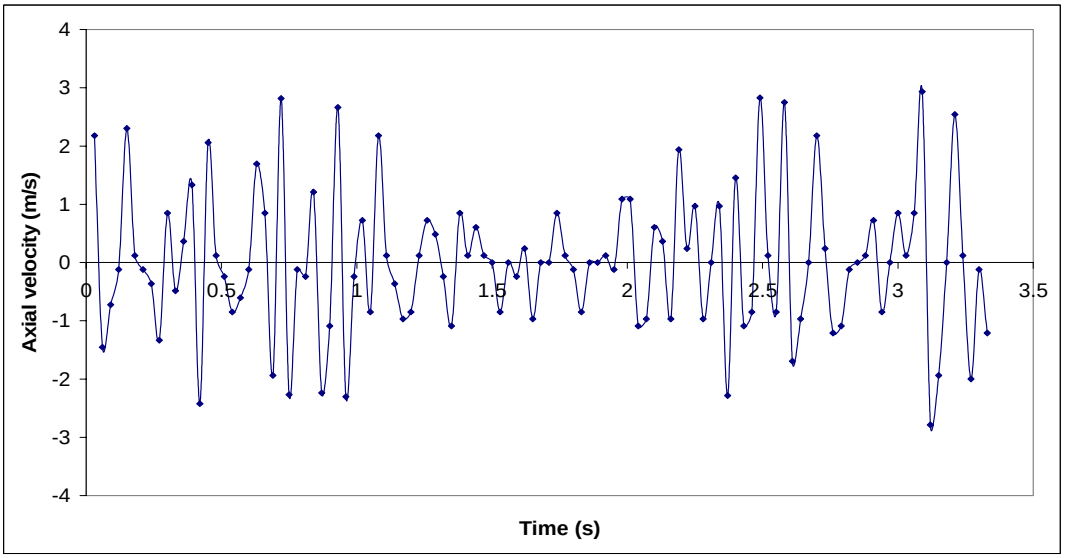

Figure 5.9 Instantaneous axial velocity plot of 1.80 mm tracer at superficial gas velocity of 2.5 m/s in the case of broad PSD

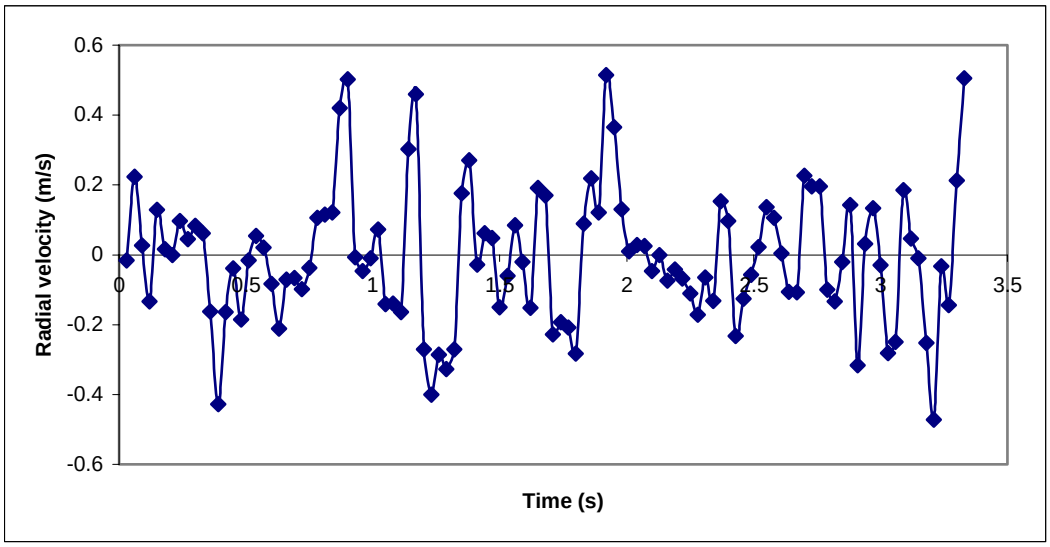

Figure 5.10 Instantaneous radial velocity plot of 1.80 mm tracer at superficial gas velocity of 2.5 m/s in the case of broad PSD

5.2.2 Particle segregation

Analysis of RPT data also allowed particle segregation to be studied in detail. Particle segregation was quantified by calculating the amount of time the tracer particle spent in different axial sections of the bed. For the purpose of this analysis, the bed was divided into 4 axial sections each of 4 cm height and the percentage of time spent by the tracer in each axial section over the 30-minute experiment was calculated. It is important to note that the static bed height was kept constant at 12 cm, therefore, the first three axial sections of 4 cm represented the dense bed and the last axial section represented the freeboard region as the bed expansion was observed to be negligible.

5.2.2.1 Effect of superficial gas velocity and tracer size on particle segregation

Figures 5.11 and 5.12 depict the segregation tendencies of the 1.3 and 2.54 mm tracers respectively and the effect of superficial gas velocity on particle mixing. In the case of narrow PSD, both the 2.54 and 1.33 mm tracer particles showed a greater

tendency to segregate at a superficial gas velocity of 1 m/s, with both tracers spending more than 40% of their time in the first 4 cm of the bed. Particle mixing improved with an increase in superficial gas velocity, with the tracers spending most of their time in the middle section of the bed. Tracer size did not have an appreciable effect on segregation with both 2.54 mm and 1.33 mm tracers being mixed to an equal degree at a given superficial gas velocity. This observation does not match with the observation of Wormsbecker et al. [10], who reported that bigger particles showed higher segregation tendency than the smaller ones at a given superficial gas velocity. However, the bed material in the Wormsbecker et al. [10] study had a broad PSD. In the present case, as the bed contained only one large size tracer in a bed of smaller particles, the effect of size may not be sufficient to produce a noticeable change in the segregation tendency of the bed material. Similar observations were reported by Gauthier et al. [6] who studied the effect of PSD of powders on their fluidization properties and found that small fraction of larger particles in a bed of smaller particles did not have an appreciable effect on fluidization behaviour of the bed material. Interestingly, with an increase in superficial gas velocity, both tracers spent more time in the middle of the bed. Due to the conical geometry of the vessel, the bed cross-sectional area increases with axial position resulting in a decrease in gas velocity. Due to this effect, it may be possible that at lower superficial gas velocities, local gas velocity in the upper sections of the bed may not be sufficient to support the weight of the particles and the particles sink towards the bottom. However, with an increase in superficial gas velocity, local gas velocity in the bottom section of the bed may be sufficiently high to toss particles up into the middle section where the local gas velocity is now higher as well. The higher velocity is sufficient to

support the particles, resulting in particles spending most of their time in the middle section.

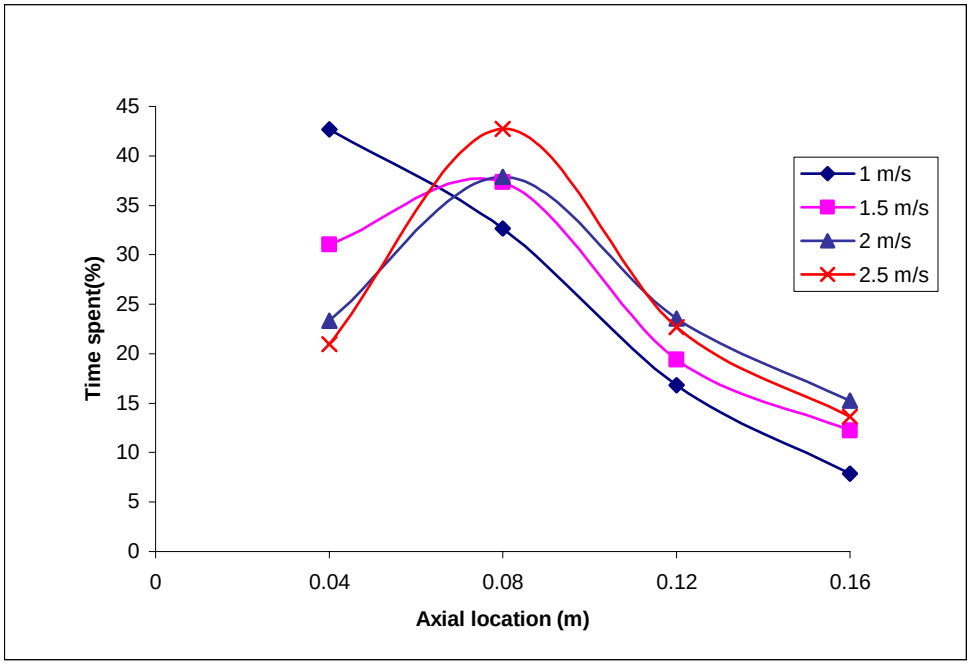

Figure 5.11 Segregation tendency of 1.33 mm tracer in the case of narrow PSD

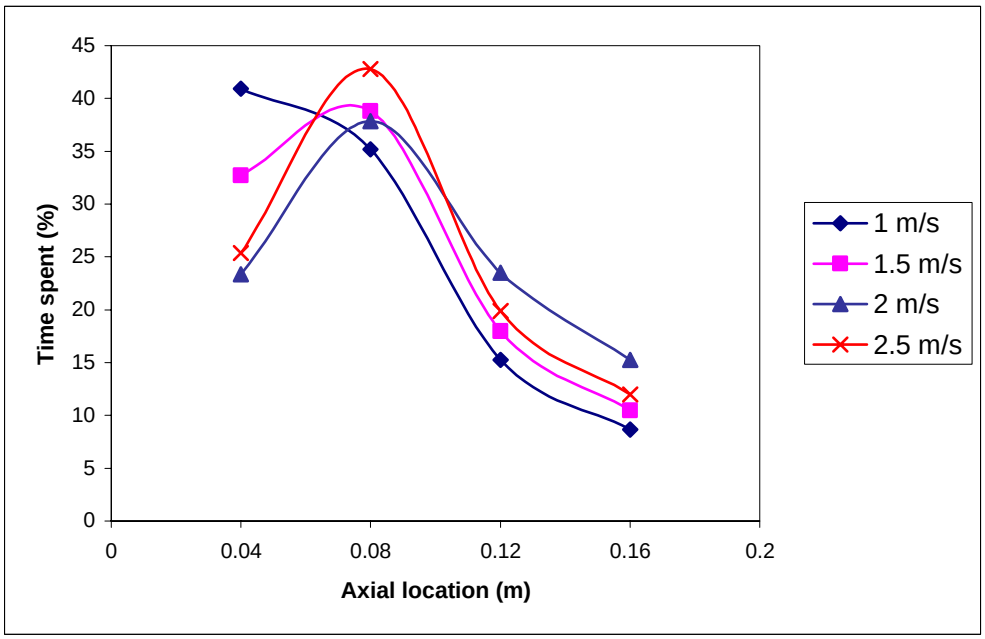

Figure 5.12 Segregation tendency of 2.54 mm tracer in the case of narrow PSD

Figures 5.13 and 5.14 depict the segregation tendencies of 1.80 and 2.60 mm tracer particles at superficial gas velocities of 1, 1.5, 2 and 2.5 m/s. In the case of broad PSD, both tracer particles showed a greater tendency to segregate at lower superficial gas velocities. This indicates that the bed was poorly mixed compared to the narrow PSD case at lower superficial gas velocities. Tracer size also had a noticeable impact, with the bigger tracer showing a much greater tendency to segregate than the smaller one at superficial gas velocities of 1 and 1.5 m/s. This is consistent with the work of Wormsbecker et al. [10] who found that particles larger than 800 μm tend to segregate at the bottom of the bed. However, at higher superficial gas velocities of 2 and 2.5 m/s particle mixing improved considerably and both the tracers exhibited similar segregation tendencies. This observed increase in the segregation tendency of both tracers in the bed having broad PSD is most likely due to changes in gas-particle and particle-particle interactions. The study of Wiens et al. [11] found that in the case of bed material having narrow PSD, penetrated bubbles were first observed at superficial gas velocity of 1 m/s. However, penetrated bubbles were first observed at 1.5 m/s in the bed having wide PSD. The presence of penetrated bubbles leads to better particle mixing as they carry the solid particles upwards in their wake. This delay in the emergence of penetrated bubbles in the case of bed having wide PSD was attributed to presence of Geldart D type particles. Observations of Wiens et al. (2006) in conjunction with particle segregation results presented in this study suggests that gas-solid interactions are affected by the PSD of the bed material. Furthermore, tracer particles used in the present study fall in the Geldart D category due to limitation of the tracer fabrication technique to produce smaller sized tracers. Therefore, tracers never encountered collisions with similar sized particles in the

case of bed having narrow PSD. However, granule having broad PSD contained large number of Geldart D type particles. Collisions between similar sized particles could have resulted in further slowing down of the tracers leading to increased segregation.

Wormsbecker et al. [10] postulated that in the case of bigger particles, the local gas velocity was less than the terminal settling velocity of those particles; therefore, they showed a tendency to segregate at the bottom of the bed.

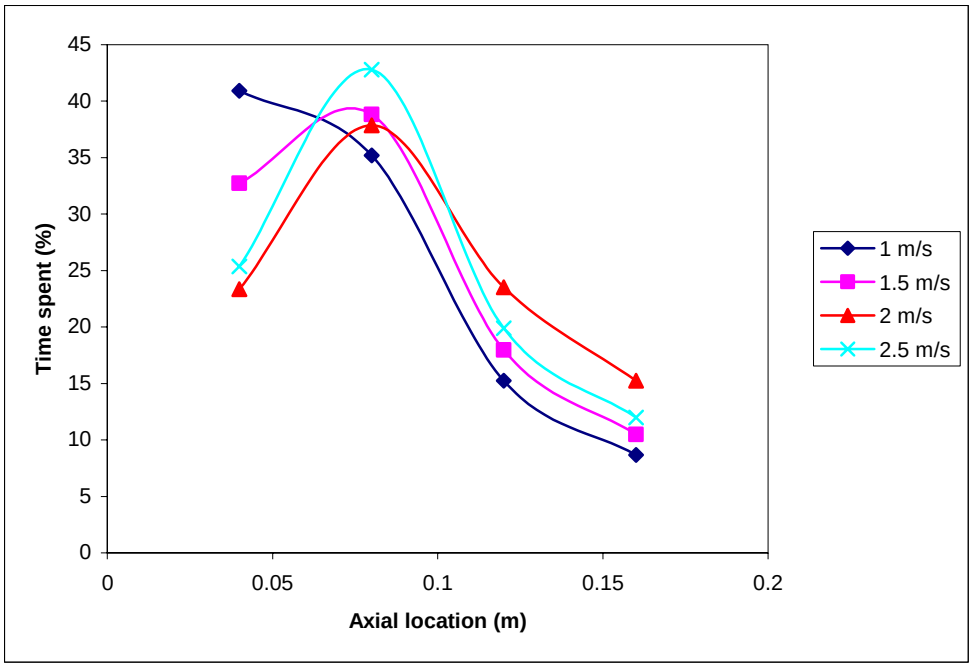

Figure 5.13 Segregation tendency of 1.80 mm tracer in the case of broad PSD

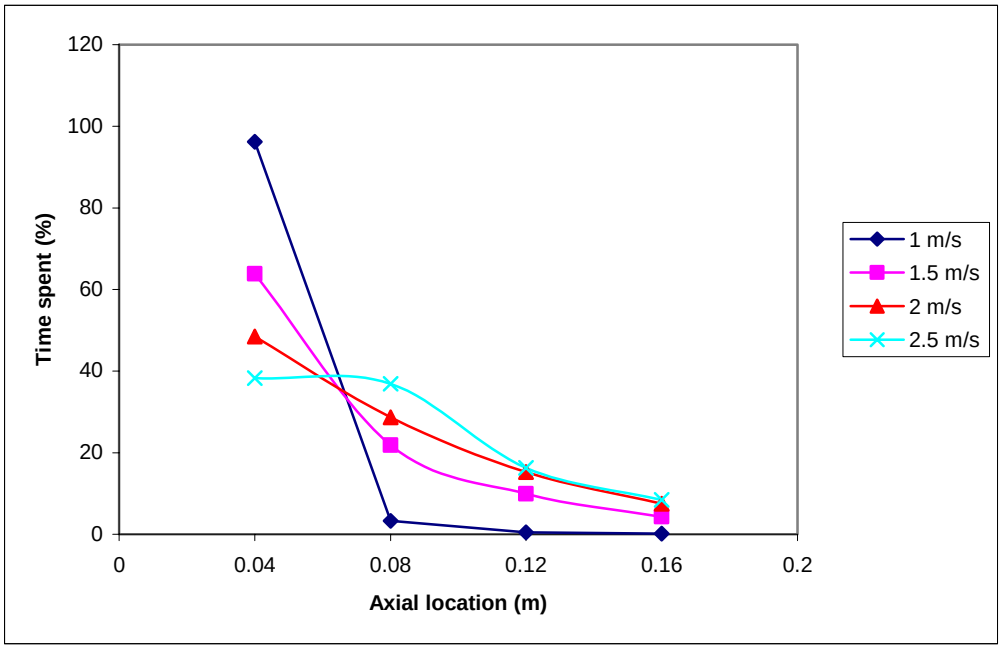

Figure 5.14 Segregation tendency of 2.60 mm tracer in the case of broad PSD

Figure 5.15 presents the terminal settling velocities for granules for varying sizes. The terminal velocity was calculated by using the Haider and Levenspiel drag equation [3] in conjunction with the Richardson and Zaki voidage function for spherical particles in Newton's region. The core voidage was taken to be 0.8 as reported by Tanfara et al. [9]. It can be seen from Figure 5.15 that the terminal settling velocities of the 1.80 and 2.6 mm tracers were 1.4 and 1.6 m/s respectively. Referring to Figures 5.13 and 5.14, it was observed that when the gas velocity was 1 m/s both tracers showed increased segregation tendencies. When the gas velocity were increased to 1.5 m/s, the mixing of 1.80 mm tracer improved considerably; mixing of the 2.60 mm tracer also improved but it remained segregated near the bottom of the bed. When the gas velocity was greater than the terminal settling velocities of both tracers, the tracers exhibited better mixing tendencies and the effect of particle size on their mixing tendency was also

diminished. Therefore, these results from the RPT measurements in the present study support the segregation mechanism proposed by Wormsbecker et al. [10].

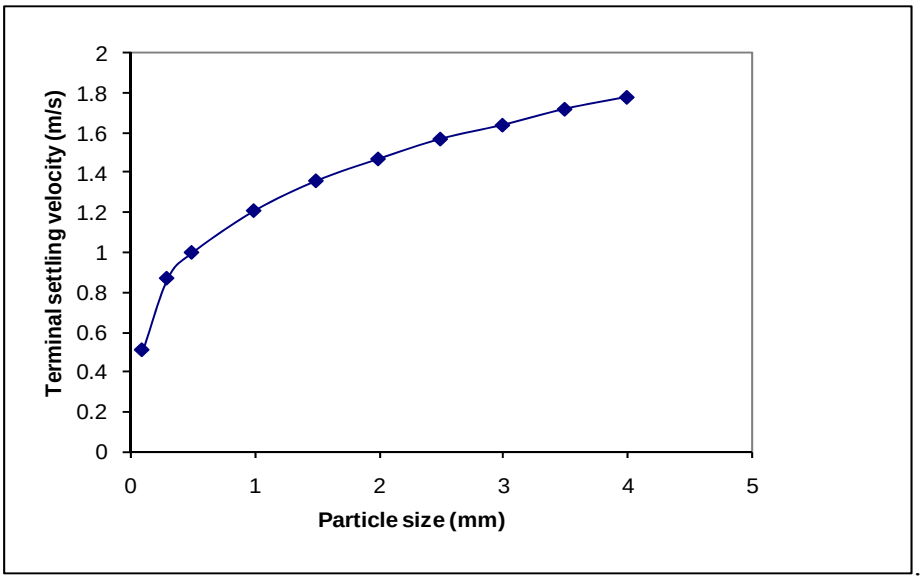

Figure 5.15 Terminal settling velocities of pharmaceutical granules calculated by using Haider and levenspiel drag equation [3] and later corrected using Richardson and Zaki voidage function

5.3 Wet bed studies

This section describes the RPT results of actual drying experiments. Two drying experiments were conducted with 1.6 mm and 2.6 mm tracers respectively. Drying lasted for 25 minutes and the moisture content was reduced from an initial value of 40 wt% to less than 5 wt% at the end of drying process. The static bed height changed from 16 cm at the start to 12 cm at the end of drying. Data obtained from the RPT was divided into 3 groups of 7 minutes each, which corresponded to moisture contents of 26, 18 and 8 wt % at the end of each 7 minute interval.

5.3.2 Particle circulation

RPT data was analyzed using a similar approach to that described in section 5.2.1 to study particle circulation. The vector plot of the first 7 minutes of drying with a 2.60 mm tracer particle in the dryer is presented in Figure 5.16, where it can be seen that the overall circulation pattern is similar to the dry bed, with particles transported upwards near the centre of the bed and falling near the walls. However, it is also evident that, contrary to the dry bed where tracer circulated freely, the tracer in the wet bed follows a more restricted path and never rises above an axial position of 8 cm (which represents only 50% of the dense bed static height at the start of the drying process). The vector plots generated from RPT data spanning 7-14 (Figure 5.17) and 14-21 minutes (not shown here) of drying also depicted similar circulation patterns with tracer moving upwards near the centre and slowly falling near the walls of the vessel. However, the tracer travelled faster and was able to rise higher with a decrease in moisture content which shows that particle mixing and particle circulation improved with the decrease in moisture content.

The vector plots of Figures 5.16 and 5.17 provide a qualitative representation of particle circulation; however, it is difficult to locate the change in hydrodynamics of the bed with decrease in moisture content from these plots. Therefore, individual axial and radial locations and corresponding axial velocities of the tracer were plotted to better understand the change in hydrodynamics of bed as drying proceeded. For ease of data interpretation, only a small portion of RPT data containing the transition in tracer behaviour is presented here.

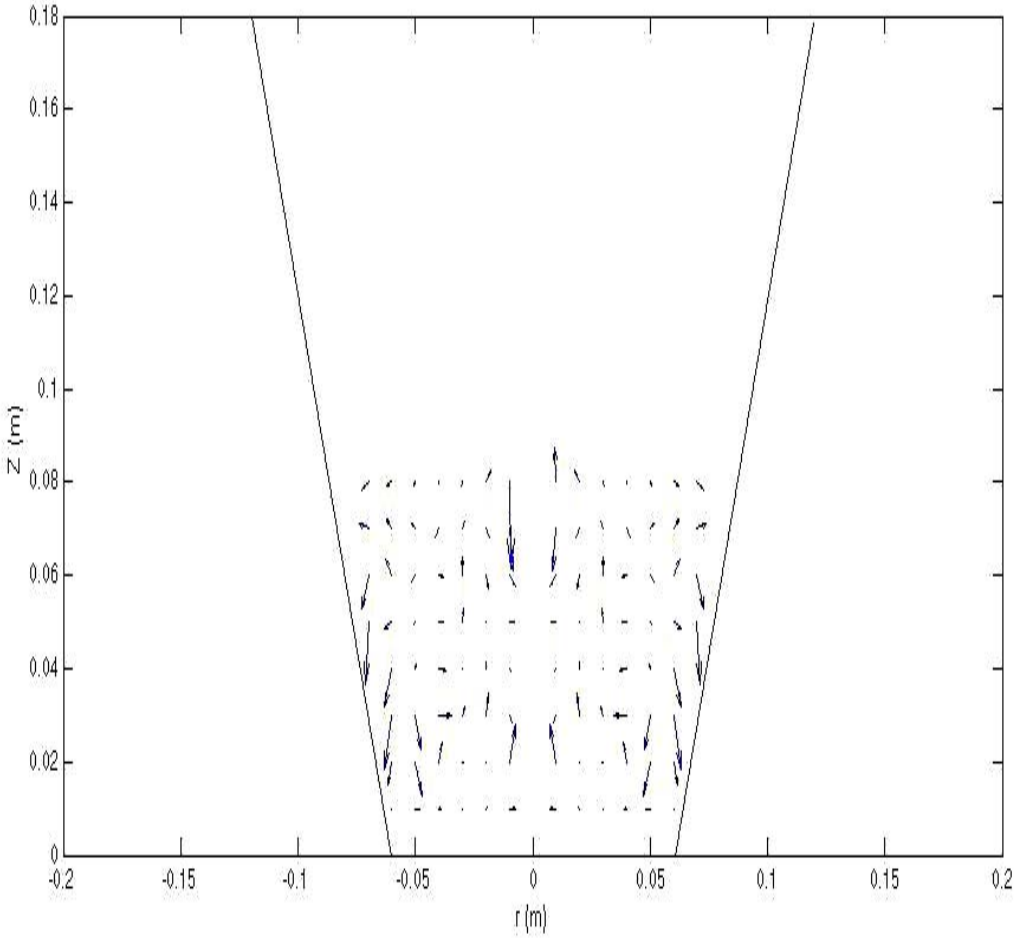

Figure 5.16 Vector plot of the axial and radial velocities depicting circulation of the particulate phase during first 7 minutes of drying using a 2.60 mm tracer at a superficial gas velocity of 1.5 m/s, 'z' represents the axial height and 'r' represents the radial distance from the axis (centre) of the vessel

Figures 5.18 to 5.20 present, respectively the radial position (r), the axial position (z) and the axial velocity of the 2.60 mm tracer with respect to drying time. Interestingly, the RPT data of Figure 5.18 reveals that during the first 6.8 minutes of drying, the tracer never reached near the centre of the bed, resulting in low axial velocity. As a result, the tracer remained axially confined to the first 5 cm of the bed, resulting in poor particle mixing. This indicates that most of the fluidizing air was passing through

the centre of the bed, leading to poor circulation of particles present away from the centre of the bed. A similar trend was seen in the case of the dry bed studies with granule having wide PSD. However, this phenomenon was more severe in the case of actual drying, suggesting that the air flow was highly restricted during the first 6.8 minutes of the drying process. After 6.8 minutes of drying, particle mixing improved considerably, which indicates that the diameter of the core region at the centre of the bed increased and the gas was more uniformly distributed throughout the bed. Similar trends were seen with the 1.60 mm tracer (not shown here).

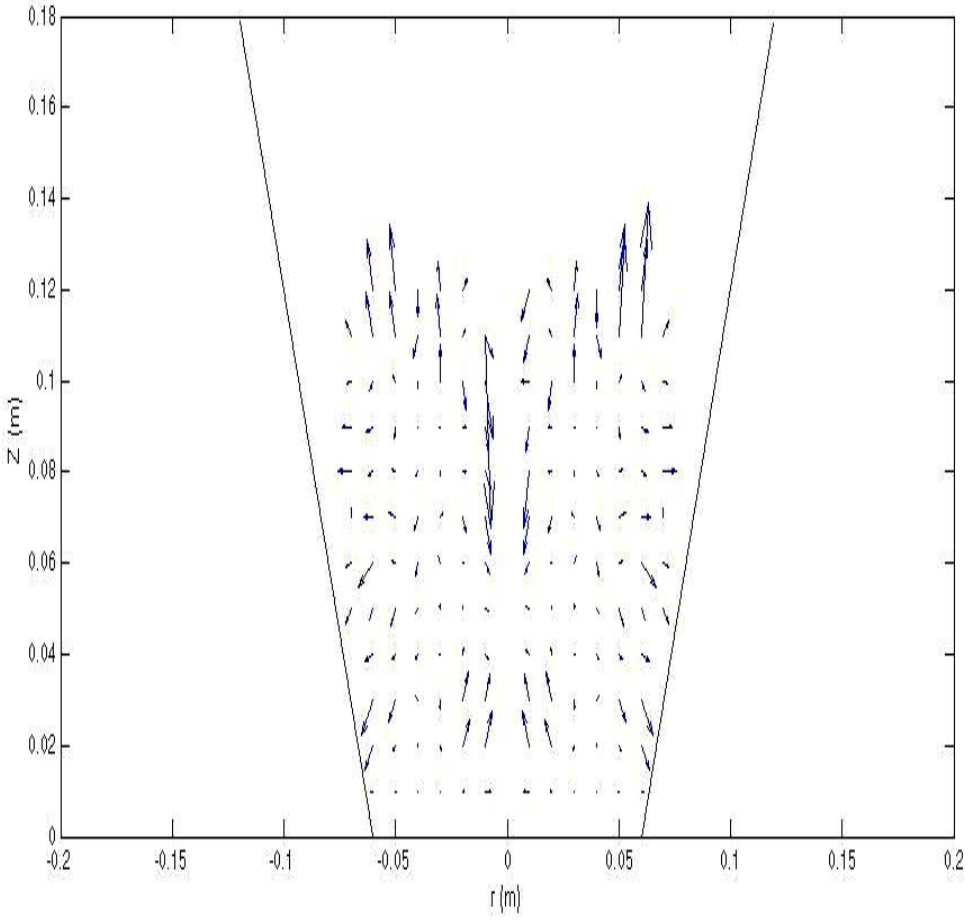

Figure 5.17 Vector plot of the axial and radial velocities depicting circulation of the particulate phase during 7-14 minutes of drying using a 2.60 mm tracer at a superficial gas velocity of 1.5 m/s, 'z' represents the axial height and 'r' represents the radial distance from the axis (centre) of the vessel

5.3.1 Particle segregation

Similar to the dry bed studies, particle segregation was quantified by calculating the percentage of time a tracer particle spent in different axial sections of the bed during drying. The bed was divided into 4 axial sections of 4 cm each and percentage of time the tracer spent in each axial section during each 7 minute interval was calculated. Figures 5.21 and 5.22 show the results of this analysis. As the static bed height during the start of the drying process was 16 cm, perfect mixing would mean that particle spent equal time in each section.

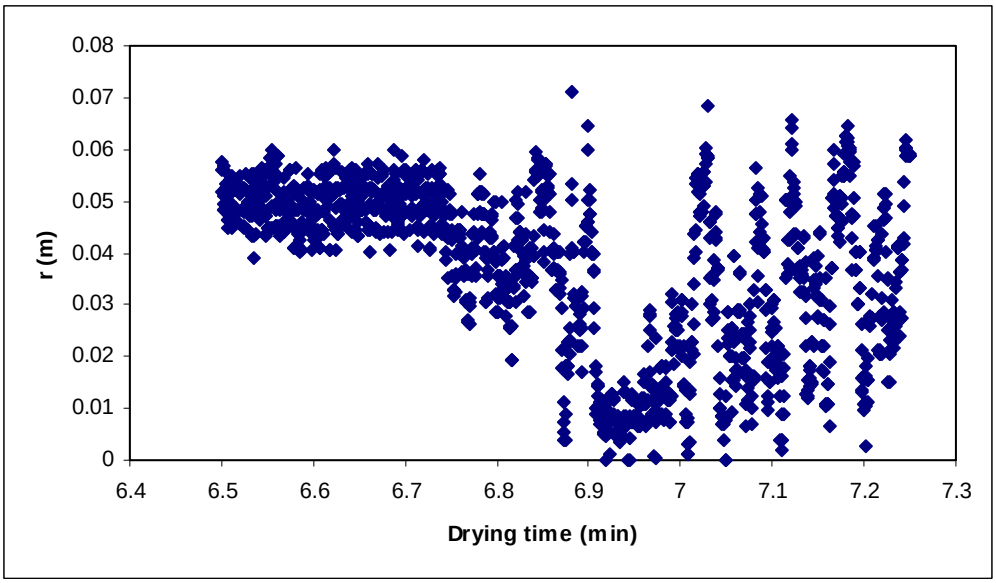

Figure 5.18 Instantaneous radial position plot of 2.60 mm tracer at superficial gas velocity of 1.5 m/s in the case of drying

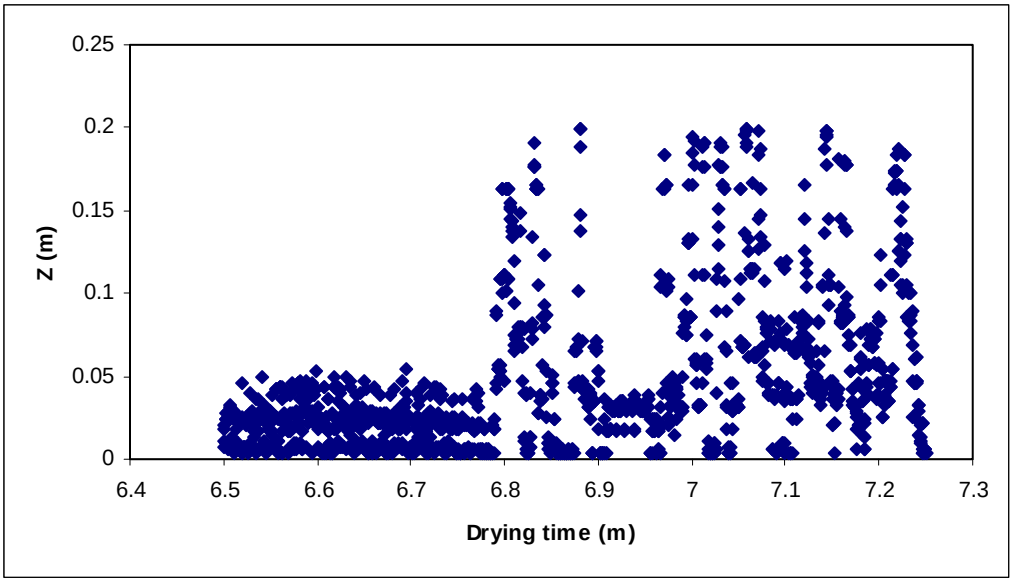

Figure 5.19 Instantaneous axial position plot of a 2.60 mm tracer at superficial gas velocity of 1.5 m/s in the case of drying

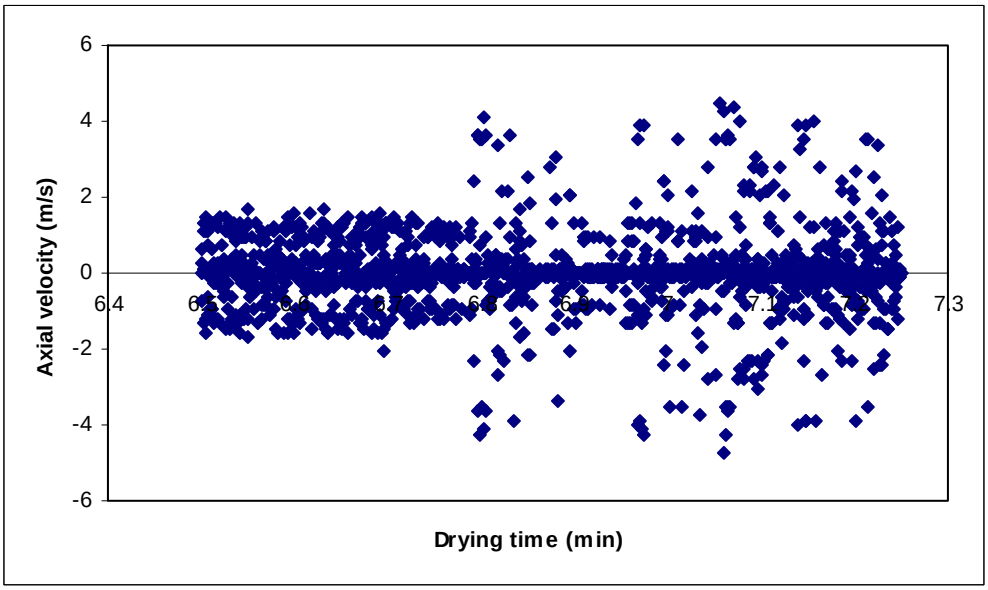

Figure 5.20 Instantaneous axial velocity plot of a 2.60 mm tracer at superficial gas velocity of 1.5 m/s in the case of drying

It is evident from Figures 5.21 and 5.22 that although the circulation pattern of the particulate phase remained the same throughout the drying process (as discussed in

the previous section), the 2.6 mm tracer spent almost 80% of its time and the 1.6 mm tracer almost 40% of its time in the first 4 cm of the bed during the first 7 minutes of drying. In the case of dry bed studies with powder having wide PSD, the bigger tracer was poorly mixed as compared to the smaller one at a given gas velocity. However, the influence of particle size on particle mixing is even more pronounced in the case of actual drying. This is due to the change in particle-particle and gas-particle interactions resulting from the presence of moisture. Particle mixing improved considerably after the first 7 minutes of drying. Figures 5.23 and 5.24 suggest that, average particle speeds were higher at the centre of the bed and decreased with increase in radial distance from the center. This indicates that air flow was higher at the center of the bed as compared to the walls throughout the drying process and supports the particle circulation pattern suggested in the previous section. However, the rate of decrease of the average speed with radial distance from the centre in the first 7 minutes of the drying process was greater than the remaining 14 minutes and this observation was consistent with both the tracers. Chaplin et al. [12] used ECT to study drying of wet pharmaceutical granule in a conical fluidized bed dryer and suggested that during the start of the drying process, the air flow was highly restricted near the centre of the bed resulting in almost all the fluidizing air passing through the centre of the bed. This can be one of the reasons for low particle speeds and poor particle mixing observed by RPT at the start of the drying process.

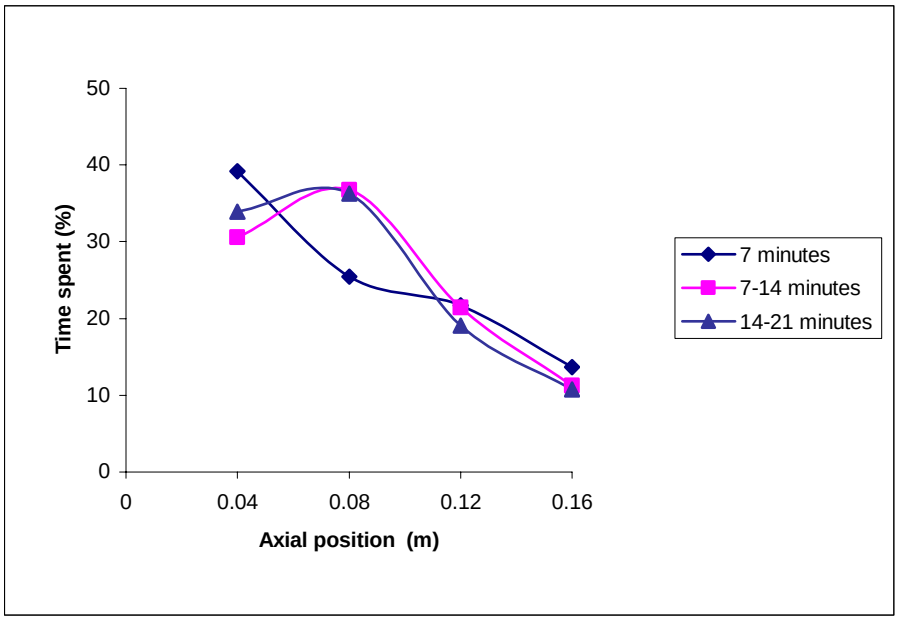

Figure 5.21 Segregation tendency of 1.6 mm tracer particle in the case of actual drying

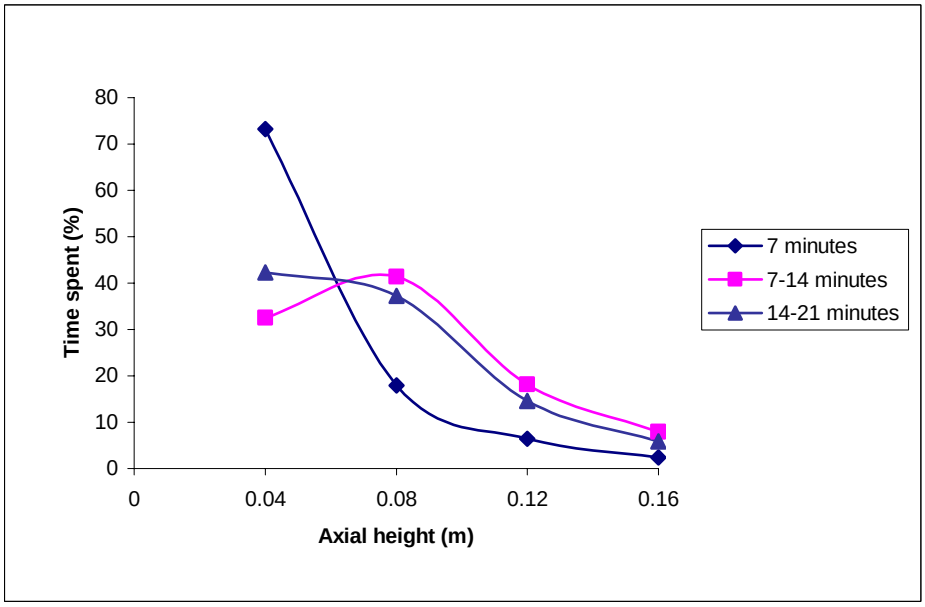

Figure 5.22 Segregation tendency of 2.6 mm tracer in the case of actual drying

During the next 7 minutes, which corresponded to a moisture content of 18 wt %, particle mixing improved significantly with both the tracers spending almost equal time in 4 and 8 cm sections of the bed. Furthermore, referring to figures 5.23 and 5.24, it

can be seen that although there is still a radial gradient of particle speed, but the gradient in noticeably less steep. This change in the particle mixing and particle speeds suggests a change in the hydrodynamics of the bed with fluidizing gas being evenly distributed throughout the bed resulting in better particle mixing. This observation is in agreement with the ECT measurements made by Chaplin et al. [12] and with the results of microscopic analysis of the particle circulation presented in the previous section. The last 7 minutes of the drying process did not show any appreciable change in the particle mixing suggesting that the bed had reached a stable hydrodynamic state. The effect of particle size can be clearly seen on the mixing of tracers with the bigger tracer particle showing higher segregation tendency than the smaller one throughout the drying process. However, the effect of particle size on mixing is less pronounced with decrease in moisture content.

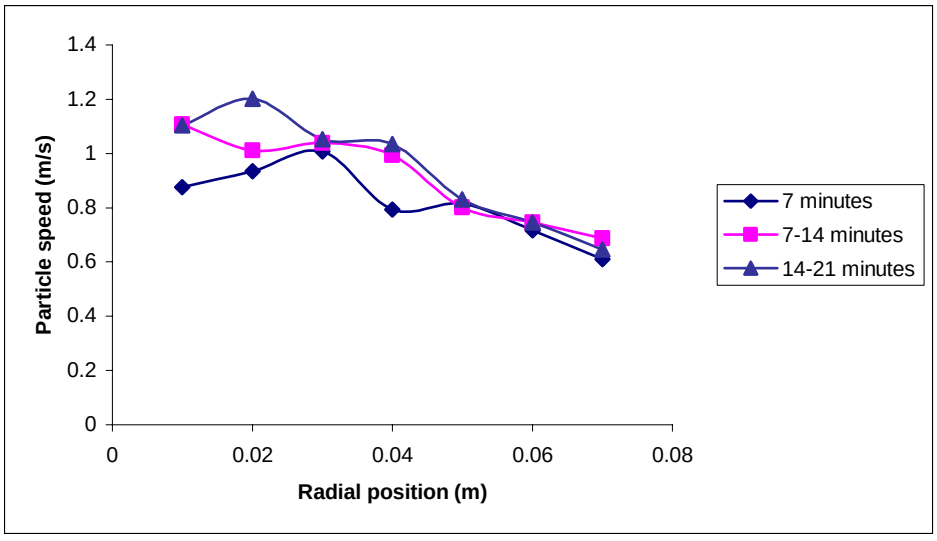

Figure 5.23 Average tracer speed of 2.60 mm tracer with respect to change in radial position at superficial gas velocity of 1.5 m/s in the case of drying

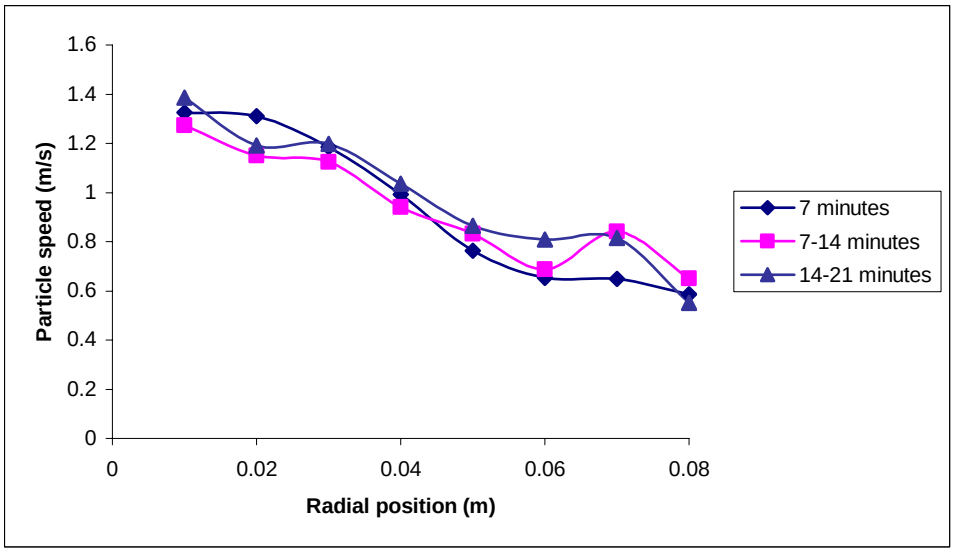

Figure 5.24 Average tracer speed of 2.60 mm tracer with respect to change in radial position at superficial gas velocity of 1.5 m/s in the case of drying

Chapter 6 Results and Discussions for High Speed Imaging

This chapter discusses the results of high speed movies captured by using a high speed camera coupled to a borescope. High speed movies provided a unique opportunity to visually observe particle motion inside a fluidized bed dryer and high quality of images ensured that individual particles could be identified and tracked over subsequent frames to calculate particle speed.

6.1 Particle motion in the case of mono-disperse sugar spheres

In the case of mono-disperse sugar spheres, particles were seen to rise and fall together both at the centre and near the wall at all superficial gas velocities. Particles were seen to rise and fall in waves and this phenomenon was consistent at the superficial gas velocities studied. The typical circulation pattern of particulate phase observed by RPT where particle were observed to rise near the centre and fall near the walls was absent in this case. Mono-disperse sugar spheres would fall into Geldart D type powder due to its mean particle diameter of 774 μm. Geldart D type powders are difficult to fluidize due to their increased size and mass and offer considerably resistance to the flow of gas inside the bed due to which gas flow may have continuously fluctuated throughout the cross-sectional area to flow through the path of least resistance. This can lead to wave motion of particles described above. Particle tracking and velocity estimation revealed that the average particle speed increased with an increase in superficial gas velocity. Furthermore, it was observed that average rise velocity was higher than average fall velocity at a given superficial gas velocity.

6.2 Particle motion in the case of 50:50 mixture

In case of 50:50 mixture of 20-25 mesh and 40-60 mesh powder, particles tended to rise and fall together at superficial gas velocities of 1.5 and 2m/s. Particles generally appeared to "stick" with one another and inter-particle distance was very small (figure-6.1). Both upward and downward motion of particles was seen near the walls and center of the vessel, which was similar to particle motion in the case of mono-disperse sugar spheres described above.

At 3m/s a dilute region with upward motion of the particulate phase began to emerge at the centre at 12 cm borescope height (figure-6.2) suggesting that most of the gas was passing through it. Particles were observed to move independently as inter-particle distance increased. Since at superficial gas velocities of 1.5 and 2 m/s, particles moved together and the inter-particle distance was very small, therefore, it was difficult to estimate speed of individual particles from the high speed movies. At superficial gas velocity of 3 m/s, inter-particle distance increased considerably at the centre of the bed and particles started moving independently. When particles moved independently, smaller particles were observed to have higher average velocity than the larger ones (figure-6.3). It was difficult to estimate segregation tendencies of particles from the high speed movies; however, the observation of smaller particles moving faster than the larger ones supports the observations made by using the RPT set-up. Another important feature of the central region was the change in particle speed. In many instances, fast moving particles were seen to rapidly change their velocities in the central region due to particle-particle collisions; this could be due to high gas flux, low particle density and high particle velocities in the central region. This observation helps in explaining the axial velocity fluctuations of the tracer when it was present near the centre of the bed.

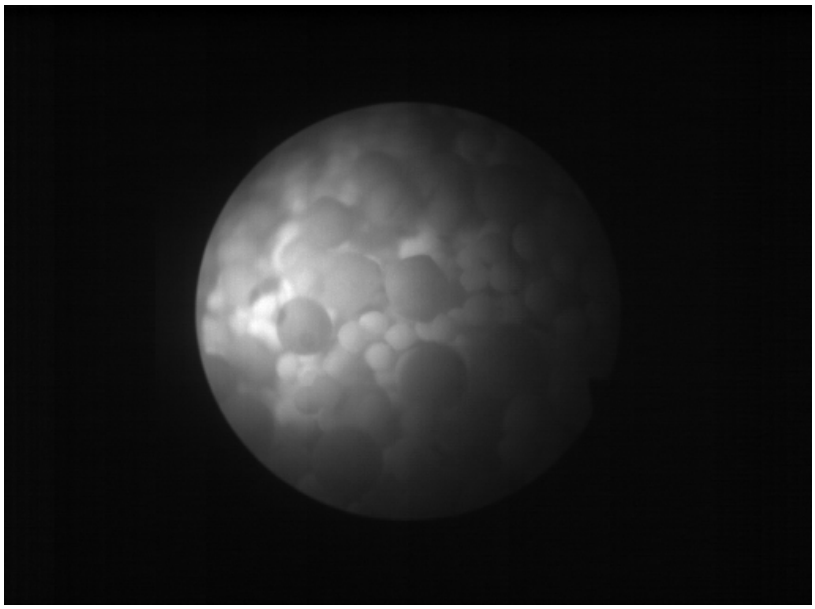

Figure 6.1 Mixture at 1.5 m/s, this picture shows particles rising together. Borescope Location: 12cm-center

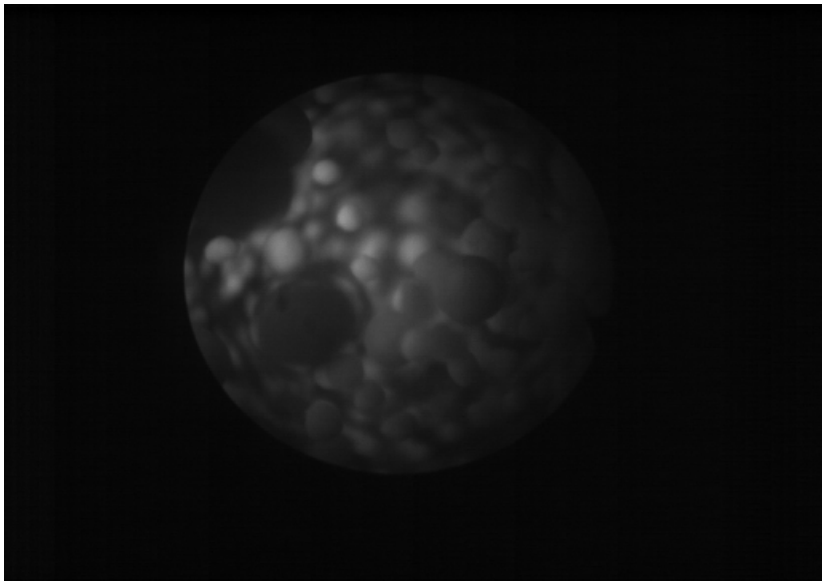

Figure 6.2 Mixture at 3m/s, depicting the emergence of dilute core region
Borescope position: 12cm-center

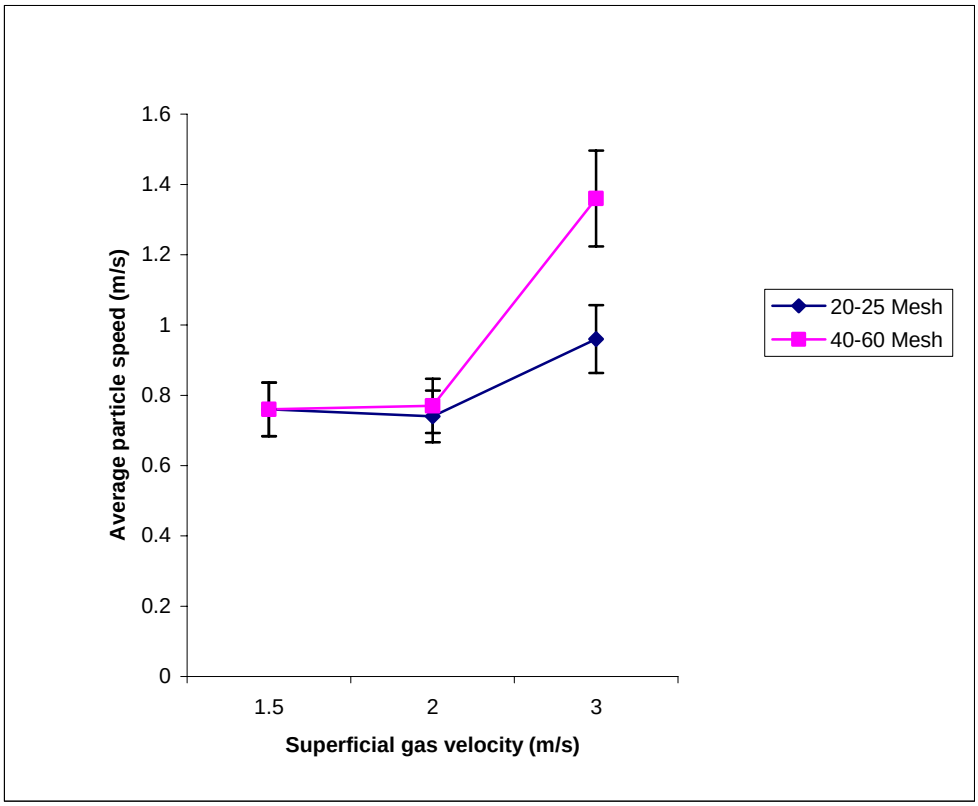

Figure 6.3 Comparison of average particle rise velocities of particles of different sizes in the case of mxture. Borescope location: 12cm-center

6.3 Particle motion in the case of placebo pharmaceutical granulate

In the case of placebo granulate having wide PSD, at the lowest superficial gas velocity of 1.5 m/s, both upward and downward particle motion was observed at the centre of the bed. Particles larger than 1 mm were not seen rising in the core region at 1.5 m/s. As the minimum borescope insertion height was 12 cm, it may be possible that very few particles having diameter greater than 1 mm were able to rise up to 12 cm in the bed at this velocity, which demonstrates that particles greater than 1 mm tend to segregate at superficial gas velocity of 1.5 m/s. At superficial velocities of 2 and 3 m/s, particles greater than 1 mm were frequently seen rising which revealed that mixing of particulate phase increased with the increase in superficial gas velocity. However, smaller particles were observed to move faster than the larger ones (figure-6.4) which was consistent with

the observations made in the case of mixture. The central region became more dilute with the increase in superficial gas velocity and downward motion of particles in the dilute region became almost non existent. Furthermore, average rise velocity of the particulate phase was higher than average fall velocity (figure 6.5) which matched well with the observations made by RPT system.

At superficial gas velocities of 2 and 3 m/s (figure 6.6) when the borescope was positioned at a height of 12 cm, particles were generally seen to be moving up at high speeds at the centre of the bed. However, particle motion was observed to be slow and downwards near the walls of the vessel, this circulation pattern was consistent with the circulation pattern suggested by RPT.

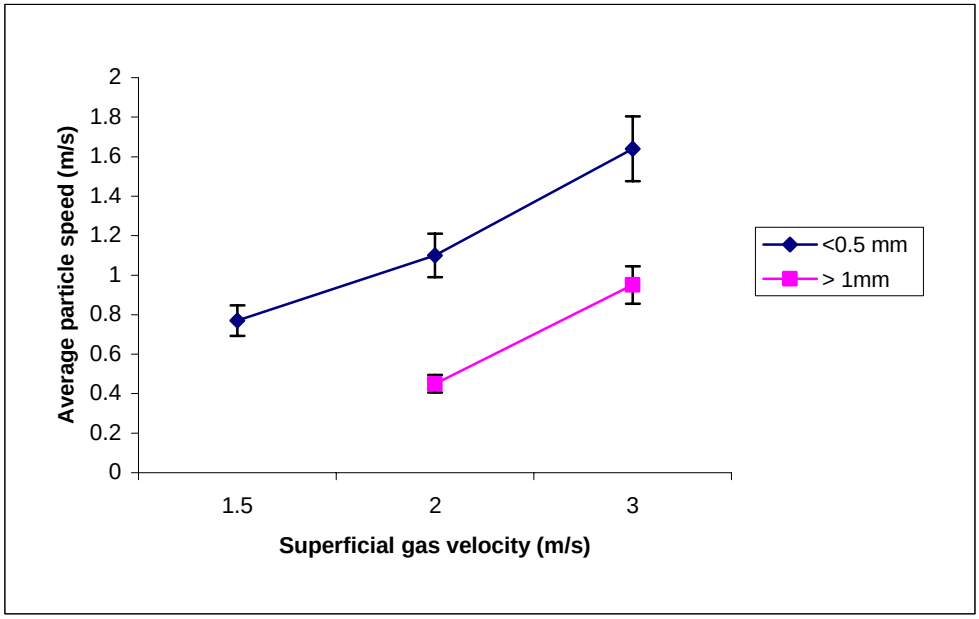

Figure 6.4 Effect of particle size on average particle velocities in the case of placebo
Borescope position: 12cm-center

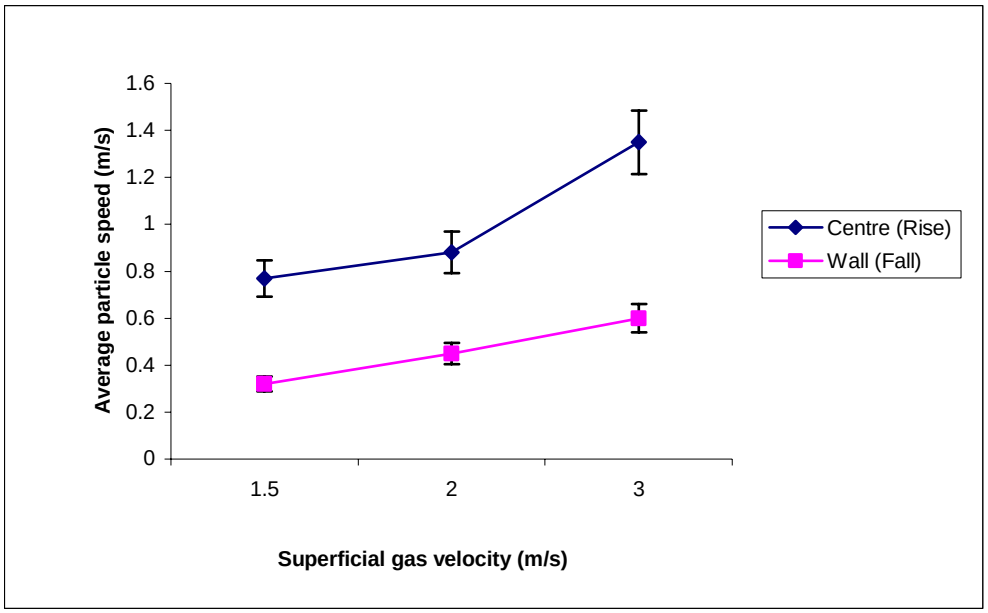

Figure 6.5 Comparison of average particle velocities at the centre and wall of the bed at 12cm borescope height

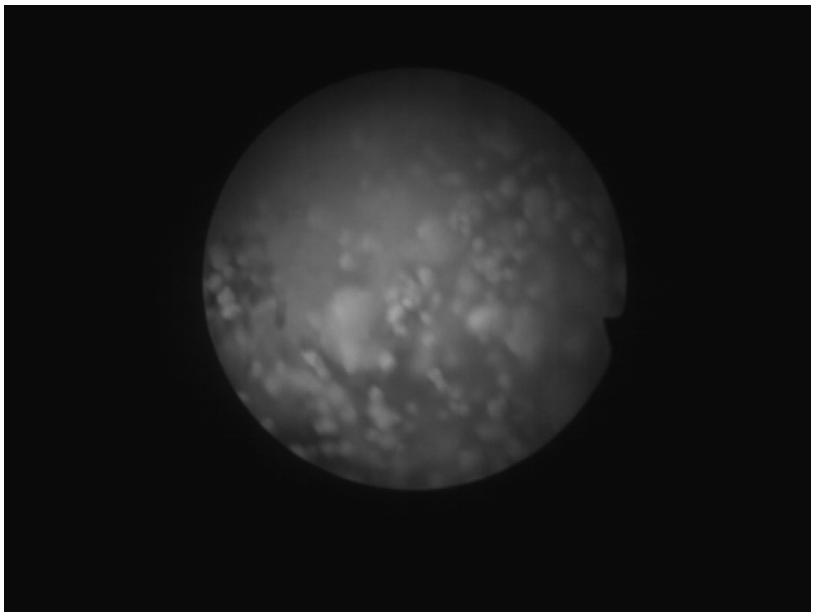

Figure 6.6 Placebo at 3m/s, picture depicting dilute region at the centre of the bed Borescope position: 12cm-centre

The placebo granulate had the smallest mean particle diameter and the widest size distribution among the three test powders and a dilute region at the centre of the bed was observed at 2 and 3m/s superficial gas velocities. Since this dilute region was completely absent in the case of the sugar sphere mixture and developed at superficial gas velocity of 3 m/s in the case of mono-disperse test powder, it can be deduced that mean particle size and particle size distribution of the bed material clearly has a profound effect on the movement and circulation of particulate phase inside a conical fluidized bed. Further research needs to be done to fully understand this relationship.

6.4 Comparison of Radioactive Particle Tracking with High Speed Imaging

Two particles tracking techniques have been developed and used in the present study to study the effect of particle size distribution on the motion and segregation tendencies of the particulate phase inside a conical fluidized bed dryer. RPT is a powerful particle tracking technique that can provide valuable experimental data regarding motion of particulate phase which can improve our basic understanding of particle motion and can be used for validation of mathematical models. However, it is a very challenging technique to design and develop as it involves intensive mathematical modeling and computer programming. Furthermore, RPT uses a radioactive tracer, therefore, it can not be used if there is no slowpoke nuclear reactor in the vicinity or if there is a policy against contamination in process equipments.

High speed imaging technique is a very robust particle tracking technique that can be easily used on lab and industrial scale. Visual observations made by capturing high speed movies provide good understanding of the motion of particulate phase on a microscopic level. However, it can only provide limited information on the macroscopic

scale and due to limitation of the installed memory on the high speed camera, only 1 second of continuous motion could be recorded. Therefore, although the results of RPT matched well with the results of high speed imaging in principle, it is not advisable to compare the magnitude of particle speeds from both the techniques. Furthermore, two different fluidized beds were used in both studies which can also impact the magnitude of results of both studies.

Chapter 7 Conclusions and Recommendations

7.1 Conclusions

The objective of the present study was to perform particle tracking in a conical fluidized bed dryer to study particle segregation and movement of the particulate phase. To achieve this objective, two particle tracking systems were developed. The first one was called the radioactive particle tracking (RPT) system and it was developed at the fluidization laboratory at U of S. RPT system tracked the motion of a γ-ray emitting tracer particle inside a conical fluidized bed dryer by strategically located scintillation detectors located outside the dryer. RPT experiments were conducted first in dry bed using two different particle size distributions and then during actual drying of pharmaceutical granule. Two tracers of different sizes were tracked in each experiment to understand the effect of particle size on its motion. The second technique used a high speed camera coupled with a borescope to capture high speed movies of the movement of particulate phase inside a conical fluidized bed dryer at research laboratories of Merck Frosst & Co., Montreal. Particle tracking was performed offline by analyzing the motion of individual particles in subsequent frames of the high speed movies. The following conclusions were drawn from the present study:

- Vector plot of the movement of tracer particles from RPT data revealed that particles move upwards at high speeds near the centre of the bed and fall slowly near the wall.
- Particle size was found to have a profound effect on the segregation tendencies of the particulate phase. Bigger particles were more inclined to segregate near the bottom of the bed and moved slowly compared to smaller ones. This effect was more pronounced at superficial gas velocity of 1 m/s.

- Particle size distribution (PSD) of the bed material was seen to influence the segregation tendencies of tracer particles. At similar gas velocities, tracers were more segregated in the case of bed material with broad PSD. Effect of tracer size was also more pronounced in the bed having wide PSD with larger tracer showing higher segregation tendencies than the smaller one. This can be due to increase in collision frequency of the bigger particles resulting in increased resistance in the path of tracers in the case of bed having broad PSD and changed nature of gas-particle interactions.
- Particle segregation decreased with increase in superficial gas velocity and it was observed that segregation due to size difference was negligible when superficial gas velocity was above the terminal velocity of particles. This can be due to change in dominating force on the particles from gravity at lower gas velocities to drag exerted by upward moving gas at higher gas velocities. This observation supports the segregation mechanism proposed by Wormsbecker et al. [10].
- Particle segregation was observed to be high with tracer spending most of the time near the bottom of the bed at the start of actual drying of wet pharmaceutical granule. This can be due to high moisture content of the bed material. Particle mixing improved considerably after first 7 minutes of drying. The moisture content dropped from 40 % w/w to 18 % w/w during this time. This change can be attributed to change in the hydrodynamics of fluidized bed dryer after first 7 minutes of drying. This observation matched well with the observations of Chaplin et al. [12].

- Similar to dry bed studies, particle size had an appreciable effect on particle mixing during drying with bigger tracer showing higher segregation tendency than the smaller one throughout the drying process.
- Analysis of high speed movies provided visual confirmation of the circulation pattern depicted by the vector plots generated from RPT data and agreed in principle with the particle segregation tendencies observed by RPT.

Both particles tracking techniques used in the dry bed studies agreed well in principle regarding the mixing and circulation patterns of the particulate phase in the case of a conical fluidized bed dryer. However, it is not advisable to compare the magnitude of results of both the techniques due to different nature of the two techniques and change in experimental conditions.

7.2 Recommendations

This project involved the development of two particle tracking techniques to perform particle tracking in a conical fluidized bed dryer. Both techniques have room for improvement. Resolution of RPT system can be improved by improving the process of calibration. In the present study tracer was placed at 14 known locations to calibrate the system due to constraints of manually placing the tracer at known locations. This resulted in 3-D resolution of 9 mm. However, an automated calibration system can be designed, which would place the tracer at 200-250 known locations inside the bed resulting in improved resolution of the RPT system. Furthermore, in the present study, the tracer was stationary at each known location during the calibration process. However, in actual process, tracer is always moving. Therefore, an automated system will make it possible to

calibrate the RPT system while tracer is moving from one known location to another with a known speed. Another feature which needs improvement is the size of the tracer particle. The smallest tracer used in present study was 1.33 mm in diameter due to limitation of the fabrication technique used in preparing the tracers. New tracer fabrication techniques should be investigated to reduce the tracer size to less than 500 μm. Furthermore, RPT technique can be used in conjunction with ECT technique to study the movement of gas and solid phase simultaneously to better understand the hydrodynamics of conical fluidized bed.

High speed imaging was useful for localized study of particulate phase. However, particles tend to stick to the borescope lens making the technique unsuitable for use in regions with high particle density. A protective cap or some kind of cleaning mechanism can be used to remove this shortcoming. Furthermore, due to limitation of installed memory of 2 GB on the high speed camera, only 1 second of continuous motion could be observed, the installed memory on the high speed camera can be increased to remove this bottleneck.

References

[1] Lim. K.S., Zhu, J.X., Grace J.R., Hydrodynamics of gas-solid fluidization, International Journal of Multiphase Flow, 21 (Suppl.), 1995, 141-193.

[2] Geldart, D. Types of Gas Fluidization, Powder Technology, 1973, 7, 285-292.

[3] Kunii, D., Levenspiel, O., Fluidization Engineering (2^{nd} Edition), Butterworth-Heinemann, Toronto, 1991.

[4] Tanfara, H., Pugsley, T., Winters, C., Effect of particle size distribution on local voidage in a bench-scale fluidized bed dryer, Drying Technology 2002, 20, 1273-1289.

[5] Grace, J. R., Sun, G., Influence of particle size distribution on the performance of fluidized bed reactors, The Canadian Journal of Chemical Engineering 1991, 69, 1126-1123.

[6] Gauthier, D., Zerguerras, S., Flamant, G., Influence of the particle size distribution of powders on the velocities of minimum and complete fluidization, Chemical Engineering Journal 1999, 74, 181-196.

[7] Rowe, P. N., Nienow, A.W., Agbim, A. J., A preliminary quantitative study of particle segregation in gas fluidized beds- binary systems of near spherical particles. Trans. Inst. Chenical Engineering 50, 1972, 324-333.

[8] Hoffmann, A. C., Romp, E. J., Segregation in a fluidized powder of a continuous size distribution, Powder technology, 66, 119-126.

[9] Tanfara, H., Hydrodynamics of fluidized beds used in the pharmaceutical industry, M.Sc. thesis, 2000, University of New Brunswick.

[10] Wormsbecker, M., Adams, A., Pugsley, T., Winters, C., Segregation by size difference in a conical fluidized bed of pharmaceutical granulate, Powder Technology, 2005, 153, 72-80.

[11] Wiens, J., Pugsley, T., Tomographic imaging of a conical fluidized bed of dry pharmaceutical granule, Powder Technology, 2006, 169, 49-59.

[12] Chaplin, G., Pugsley, T., van der Lee, L., Kantzas, A. and Winters, C., 2005b, The dynamic calibration of an electrical capacitance tomography sensor applied to the fluidized bed drying of pharmaceutical granule, Meas. Sci. & Technol. 16, 1281-1290.

[13] van Ommen, J.R., Coppens, M.C., van Den Bleek, C. M., Early warning of agglomeration in fluidized beds by attractor comparison, AIChE Journal, 2000, 46(11), 2183-2197.

[14] Chaouki, J., Larachi, F. and Dudukovic, M.P., 1997, Non-invasive monitoring of Multiphase flows, Elsevier, The Netherlands.

[15] Lin, J. S., Chen, M. M., and Chao, B. T., A novel radioactive particle tracking facility for measuring solids motion in gas fluidized beds, AIChE Journal, 1985, 31, 465-473.

[16] Devanathan, N. Moslemian, D., Dudukovic, M.P., Flow mapping of bubble columns using CARPT, Chemical Engineering Science, 1990, 45, 2285-2291.

[17] Dudukovic, M.P., Bhusarapu, S., Al-Dahhan, M.H., Powder Technology, 2006, 163, 98-123.

[18] Yang, Y.B., Devanathan, N., Dudukovic, M.P., Liquid backmixing in bubble columns, Chemical Engineering Science, 1992, 47, 2859, 2864.

[19] Kumar, S.B., Devanathan, N., Moslemian, D., Dudukovic, M.P., Chemical Engineering Science, 1994, 49, 5637, 5652.

[20] Larachi, F., Kennedy, G., Chaouki, J., A γ-ray detection system for 3-D particle tracking in multiphase reactors, Nuclear instruments & methods in physics research A, 1994, 568-576.

[21] Godfroy, L., Larachi, F., Kennedy, G., Grandjean, B.P.A., Chaouki, J., On-line flow visualization in multiphase reactors using neural networks, Appl. Radiat. Isot., 1997, 48-225.

[22] Bram, S.A., Turton, R., Particle velocity and voidage profiles in a draft tube equipped spouted-fluidized bed coating device, Chemical Engineering Communications, 2004, 191, 1379-1400.

[23] Kai, T., Misawa, M., Takahashi, T., Tiseanu, I., Ichikawa, N., Observation of three-dimensional structure of bubbles in a fluidized catalyst bed, Canadian Journal of Chemical Engineering, 2005, 83, 113-118.

[24] Pallares, D., Johnsson, F., A novel technique for particle tracking in cold two-dimensional fluidized beds-simulating fuel dispersion, Chemical Engineering Science, 2006, 61, 2710-2720.

[25] Chaplin, G., Pugsley, T.,Winters, C., The S-static as an early warning of entrainment in a fluidized bed dryer containing pharmaceutical granule, Powder Technology, 2005, 149, 148-156.

[26] Godfroy, L., PhD thesis, Ecole polytechnic, 1997.

[27] Roy, S., Larachi, F., Al-Dahhan, M.H., Dudukovic, M.P., Optimal design of radioactive particle tracking experiments for flow mapping in opaque mutiphase reactors, Applied radiations and isotopes, 2002, 56, 485-503.

[28] Wielopolski, L., The Monte Carlo calculation of the average solid angle subtended by A right circular cylinder from distributed sources, Nuclear instruments and methods, 1977, 577-581.

[29] Beam, G.B., Wielopolski L., Gardner, R.P., Verghese, R., Monte Carlo calculation of Efficiencies of right-circular cylindrical NaI detectors for arbitrarily located point Sources, Nuclear Instruments and methods, 1978, 501-508.

[30] Gupta, P., Churn turbulent bubble columns experimentation and modeling, PhD thesis, 2002, CREL, University of Washington.

[31] Tsoulfanidis, N., Measurement and detection of radiation, series in nuclear engineering, McGraw-Hill, 1983.

[32] Cesana, A., Terrani, M., An empirical method for peak-to-total ratio computation of a gamma-ray detector, Nucl. Instr. & Meth. A281, 1989, Pg- 172-175.

Appendix A

The following Visual Basic code was written to operate the DigiBASE in LIST mode and to transfer the data recorded by DigiBASE to a personal computer for further analysis.

```
Option Explicit
 Dim bstop As Boolean

    Dim totalcounts(100) As Double

  Dim UCONN21(100) As Object



Private Sub Command1_Click()

       Dim i
       Dim version As String
       Dim serialnumber As String
       Dim starttime As Date
       Dim stoptime As Date
Text1.Text = " "
Text1.SelStart = 0
Text1.SelLength = 0


            For i = 1 To List1.ListCount
          If List1.Selected(i - 1) Then
            Set UCONN21(i - 1) = CreateObject("UMCBI.CONN.2")
             ULIST1.SelIndex = i
             UCONN21(i - 1).Address = ULIST1.SelAddress
             UCONN21(i - 1).Open
             version = Trim(UCONN21(i - 1).Comm("SHOW_VERSION"))
             serialnumber = Trim(UCONN21(i - 1).Comm("SHOW_SNUM"))
             version = Left(version, Len(version) - 1)
             version = Mid$(version, 3)
             serialnumber = Mid$(serialnumber, 3)

             serialnumber = "& serialnumber"
             prepareMCB (i - 1)
             totalcounts(i - 1) = 0
          End If

       Next i
       '
       'start all
       '
```

```
        Dim ldata As Variant
Open "testdata.bin" For Binary As #1
        starttime = Time()
        For i = 1 To List1.ListCount
           If List1.Selected(i - 1) Then
              UCONN21(i - 1).Comm ("Start")

           End If
        Next i
        '
        'Loop Collecting data
        '
        bstop = False
        Dim oldtime
        oldtime = Timer
        While Not bstop
           For i = 1 To List1.ListCount
              If List1.Selected(i - 1) Then
                 ldata = UCONN21(i - 1).GetRawData(0, 16384)
           If ldata(0) <> 0 Then
                    ReDim Preserve ldata(ldata(0) \ 4) As Long
           Put #1, , i
                    Put #1, , ldata
                    totalcounts(i - 1) = totalcounts(i - 1) + ldata(0) \ 4
           End If
              End If
           Next i
           DoEvents
           If Timer - oldtime > 1 Then
              For i = 1 To List1.ListCount
                 If List1.Selected(i - 1) Then
                    Text1.SelText = "MCB " & i & " total conversions = " & totalcounts(i - 1)
& vbCrLf

                 End If
              Next
              oldtime = Timer


           End If
           If oldtime > Timer Then oldtime = Timer
        Wend
        stoptime = Time()
        Text1.SelText = "started: " & starttime
        Text1.SelText = "finished: " & stoptime
        Dim elapsed
        elapsed = (stoptime - starttime) * 3600 * 24
        Text1.SelText = "elapsed = " & Format$(elapsed, "0s") & vbCrLf
```

```
        For i = 1 To List1.ListCount
           If List1.Selected(i - 1) Then
              Text1.SelText = "MCB " & i & " got " & totalcounts(i - 1) & " Conversions = "
& Format$(totalcounts(i - 1) / elapsed, "0.0") & " cps" & vbCrLf
              restoreMCB i - 1
           End If
Next i
       Close #1
End Sub

Private Sub Command2_Click()
bstop = True
End Sub

Private Sub form_load()

ULIST1.CreateList
Dim i As Integer
For i = 1 To ULIST1.MaxSelection
ULIST1.SelIndex = i
List1.AddItem ULIST1.SelName

Next i

End Sub

Sub prepareMCB(ByVal index)
       UCONN21(index).Comm ("SET_HV 675")
       UCONN21(index).Comm ("ENAB_HV")
       UCONN21(index).Comm ("STOP")
       UCONN21(index).Comm ("SET_MODE_LIST")
       UCONN21(index).Comm ("SET_GAIN_FINE 0.7865")

   End Sub
   Sub restoreMCB(ByVal index)
      UCONN21(index).Comm ("STOP")
      UCONN21(index).Comm ("SET_MODE_PHA")
 UCONN21(index).Comm ("CLEAR_ALL")
   End Sub
    Private Sub cmdstop_click()

   End Sub
```

Appendix B

The following code was written in C++ to convert the data recorded by the Scintillation detectors from binary format to text format.

```
#include <stdio.h>
#include<conio.h>
#include<iostream>
#include<fstream>

#define VBHEADER 3 // 3 words (32 bits) = 12 bytes added by visual basic!
#define MAXWORD 20480 // may need to be adjusted
main( int argc, char* argv[])
	{
	long event_time, event_data;
	long header[VBHEADER];
	long packet_bytes, packet_words;
	long packet[MAXWORD];
		short detector[2];
	int i;
	FILE *infp, *outfp;

	if( argc > 1 )
		{
		// if a file is given on the command line read from it
		if( (infp = fopen(argv[1], "rb") ) == NULL)
			{
			fprintf( stderr, "Cannot open file %s for reading\n",argv[1]);
			exit(1);
			}
		fprintf(stderr, "Opened file %s for reading.\n", argv[1]);
		}
	else
		{
		// otherwise read from the standard input
		// and write to standard output
		infp = stdin;
		outfp = stdout;
		}
	if( argc > 2 )
		{
		// if a second file is given on the command line
		// write to it, otherwise write to standad output
		if( (outfp = fopen( argv[2], "w") ) == NULL)
			{
			fprintf( stderr, "Cannot open file %s for writing\n",argv[2]);
			exit(1);
```

```
                }
        fprintf(stderr, "Opened file %s for writing.\n", argv[2]);
        }
    else
        {
        outfp = stdout;
        }

    // loop over reading in the input file until and end of file
    for(;;)
        {
                        // read the detector number
                        if( fread( detector, sizeof(short), 2, infp) != 2)
                                {
            // end of file reached
            fclose(infp);
            fclose(outfp);
            exit(0);
            }

        // first skip over the VB Variant header
        if( fread( header, sizeof(long), VBHEADER, infp) != VBHEADER)
            {
            // end of file reached
            fclose(infp);
            fclose(outfp);
            exit(0);
            }
        // read the number of bytes in the packet
        if( fread( &packet_bytes, sizeof(long), 1, infp) != 1)
            {
            fprintf( stderr, "Unexpected End of File\n");
            exit(1);
            }
        packet_words = packet_bytes/4;
        //fprintf( outfp, "Packet words = %d\n", packet_words);
        if(packet_words > MAXWORD)
            {
            fprintf(stderr, "Words in packet is greater than MAXWORD, increase
it!\n");
            fprintf( stderr, "Packet words = %d\n", packet_words);
            exit(1);
            }

        if( fread( packet, sizeof(long), packet_words, infp) != packet_words)
            {
            fprintf( stderr, "Unexpected End of File\n");
            exit(1);
```

```
                }
            for(i=0; i < packet_words; i++)
                {
                // fprintf(stderr, "Word = %20x\n",packet[i]);
                // bit 31 is type of data
                if((packet[i] & 0x80000000) == 0)
                    {
                    // Data word in bits 0 - 20
                    //  so mask with 0x1fffff (0-20 set)
                    event_time = packet[i] & 0x1fffff;
                    // Time in bits 21 - 30
                    // shift right 21 bits so these are now
                    // bits 0 - 9 then mask with 0x3ff (0-9 set)
                    event_data = (packet[i] >> 21) & 0x3ff;
                    }
                else
                    {
                    // Time word in bits 0 - 30
                    //  so mask with 0x7fffffff (0-30 set)
                    event_time = packet[i] & 0x7fffffff;
                    // data = 0 will indicate it is a time event
                    event_data = 0;
                    }
                fprintf( outfp, "%5d   %7d   %10d\n", detector[1], event_data,
event_time);
                }
            }
                }
```

Appendix C

The following code was written in C++ to count the number of γ-ray counts recorded by each scintillation detectors in a given time interval.

```
#include <stdlib.h>
#include<stdlib.h>
#include<stdio.h>
#include<conio.h>
#include<iostream>
#include<math.h>
#include<fstream>
#include<iomanip>
# define PI 3.14159
main()
{
int i;
double detector, counts, tstamp,time_final =0;

ifstream in("C:/Documents and Settings/Todd/My Documents/Visual Studio
Projects/panga/panga.txt");  // opens the text file containing 19200 3D points

ofstream out_file1;
out_file1.open("detector1.txt");


ofstream out_file2;
out_file2.open("detector2.txt");


ofstream out_file3;
out_file3.open("detector3.txt");

ofstream out_file4;
out_file4.open("detector4.txt");

ofstream out_file5;
out_file5.open("detector5.txt");

ofstream out_file6;
out_file6.open("detector6.txt");

ofstream out_file7;
out_file7.open("detector7.txt");

ofstream out_file8;
out_file8.open("detector8.txt");
```

```
ofstream out_file9;
out_file9.open("detector9.txt");


ofstream out_file10;
out_file10.open("detector10.txt");


ofstream out_file11;
out_file11.open("detector11.txt");

ofstream out_file12;
out_file12.open("detector12.txt");


ofstream out_file0;
out_file0.open("detector0.txt");
while(!in.eof())
{
        in >>detector >> counts>>tstamp;


if (detector==1)
{
        if (counts>0)
        {
        cout <<detector;

        time_final =  tstamp;

        out_file1 <<"\n"<<detector<<"      " <<counts <<"      "<<time_final;
        }
}

if(detector==2)
{
if (counts>0)
        {
cout<<detector;

time_final =  tstamp;

out_file2 <<"\n"<<detector<<"      " <<counts <<"      "<<time_final;

}
}
```

```
if (detector==3)
{
if (counts>0)
        {
        time_final = tstamp;

        out_file3 <<"\n"<<detector<<"      " <<counts <<"      "<<time_final;
        }
}
if (detector==4)
{
if (counts>0)
        {
        time_final =  tstamp;
        out_file4 <<"\n"<<detector<<"      " <<counts <<"      "<<time_final;

        }}

if (detector==5)
{
        if (counts>0)
        {
        time_final =   tstamp;

        out_file5 <<"\n"<<detector<<"      " <<counts <<"      "<<time_final;

        out_file5.close;

}
}
if (detector==6)
{
if (counts>0)
        {
        time_final = tstamp;

        out_file6 <<"\n"<<detector<<"      " <<counts <<"      "<<time_final;

        }
}

if (detector==7)
{
if (counts>0)
        {
         time_final =  tstamp;

        out_file7 <<"\n"<<detector<<"      " <<counts <<"      "<<time_final;
```

```
out_file7.close;

        }
}

if (detector==8)
{
if (counts>0)
        {
         time_final =  tstamp;

        out_file8 <<"\n"<<detector<<"      " <<counts <<"      "<<time_final;
out_file8.close;

        }
}

if (detector==9)
{
if (counts>0)
        {
         time_final =  tstamp;

        out_file9 <<"\n"<<detector<<"      " <<counts <<"      "<<time_final;
out_file9.close;

        }
}

if (detector==10)
{
if (counts>0)
        {
         time_final =  tstamp;

        out_file10 <<"\n"<<detector<<"      " <<counts <<"      "<<time_final;
out_file10.close;

}
}

if (detector==11)
{
        {
         time_final =   tstamp;

        out_file11 <<"\n"<<detector<<"      " <<counts <<"      "<<time_final;
out_file11.close;
```

```
}
}

if (detector==12)
{
if (counts>0)
        {
         time_final =  tstamp;

        out_file12 <<"\n"<<detector<<"      " <<counts <<"      "<<time_final;
out_file12.close;

        }
}

}
getch();
return(0);
}
```

Appendix D

The following code was written in C++ to generate coordinates of 19200 points inside the conical bed, one using the approach of Larachi et al. [20] and using Monte-Carlo method.

```
#include <stdlib.h>
#include<stdlib.h>
#include<stdio.h>
#include<conio.h>
#include<iostream>
#include<math.h>
#include<fstream>
#include<iomanip>
# define PI 3.14159
main()
{
using namespace std;
ofstream out_file;
out_file.open("data.txt");

float    x,y,z=0,z1,r,Theta=1,Phi=0,n3,Cangle,B,r1,p;

int      i,j,k;
Cangle=(PI/180)*19;
for(i=0;i<=59;i++)
{
        z=z+.003633;
p=.125;

r=z*tan(Cangle)+.0575;

for (j=0;j<=7;j++)
{           r1=r*p;
                p=p+.125;
for (k=0;k<=39;k++)
        {
                Phi=Phi+9*(PI/180);
                x= r1*cos(Phi);
                y= r1*sin(Phi);

B=sqrt(x*x+y*y);
cout<<"value of r1 is " <<B <<endl;
cout<<x <<"," <<y <<","<<z <<endl;
out_file <<x <<"," <<y <<"," <<z<<endl;

        }  }  }cout<<z<<r1<<endl;
getch();}
```

Appendix E

The following code was written in C++ to calculate the total counts for each detector for above mentioned tracer locations inside the bed, in the presence of an attenuating media.

```
#include <stdlib.h>
#include <stdio.h>
#include <fstream>
#include<iostream>
#define N_MAX 1000000000000
#include <conio.h>
#include<math.h>
#include<iomanip>
#define PI 3.14134
#define IA 10867
#define IM 2147483647
#define AM (1.0/IM)
#define IR 2836
#define MASK 123459876
#define IQ 127773


main()
{
        using namespace std;
        int i,j;
long double X[20000], Y[20000], Z[20000];


long k;
float x;
double idum=2.;

double sum_0, sum_1, var, Eff,W3,sum_2, Omega,t;

double Ro=.0254, P, Alphamax, Alpha, W1,H,Thetacrit,Thetamin,Thetamax,L=.0508,
    OA,OB,W2,W,y;

double Theta, T1,T,N, N1, d, fD,fa,uD=3.0,
Theta1,Theta2,Theta3,TI,dr,dr1,ur=0.001,uw=.0297;

double xc=.2,yc=0.0001,zc=.166,x1c,y1c,z1c,x2c,y2c,z2c,xp,yp,zp;

double x1p,y1p, z1p,x2p,y2p,z2p,A1,A2, x2,y2,z2,x3,y3,z3,t1,t2,alpha2,beta2,
```

```
      gamma2,A,B,C,A3,B3,C3, D3,Cangle,D;

double x4,y4,z4,x5,y5,z5,t3,t4,dr2,dr3,Th,LODA,DISC;

double strenght=3700000,V=0.96,Deadtime=.000002,Counts,Timeinterval;

Cangle=(PI/180)*11;

ifstream in("panga.txt");  // opens the text file containing 19200 3D points
ofstream out_file;
out_file.open("data.txt");
ofstream out_file1;
out_file1.open("data1.txt");

cout<<"Enter the value of time interval= ";
cin >>Timeinterval;
//*************************************************************************
*****************
// Calculations for photopeak efficiency to total efficiency ratio.                *
//The scintillation crystal is 2" * 2" NaI, and the method of calculation is taken from   *
// A.Cesana et al, Nucl. Instr. & Meth. A281,1989, Pg- 172-175                      *
//*************************************************************************
*****************

float radius=2.54,height=5.08, Volume,Area,a=0.8698, b=0.4807,ratio;
Volume= PI*radius*radius*height;
Area=2*PI*radius*height;
ratio= 1-a*(exp(-b*Volume/Area));

cout<< "value of photpeak efficiency is" <<ratio <<endl;

//*************************************************************************
*******************
// Calculations for total efficiency of the scintillation detectors by Monte Carlo Method  *
// Taken from Beam et al, Nuclear Instruments & methods, 1978,154,Pg 501-508.& PhD
Thesis  *
// By Puneet Gupta, CREL, Univ of Washington.                                      *
//*************************************************************************
*******************


for(i=1;i<=19000;i++)      // loop to calulate efficiency at each point
{
        in >>X[i] >> Y[i]>>Z[i]; // arrays are assigned the value of each point one by one


        xp=X[i]; yp=Y[i]; zp=Z[i];
```

```
        /*first Coordinate transform of XY plane*/

if (xc>0)
{
        A1=atan(yc/xc);

}
else
{




        A1=PI+atan(yc/xc);
}

x1p=xp*cos(A1)+yp*sin(A1);
y1p=-xp*sin(A1)+yp*cos(A1);
z1p=zp;

x1c=xc*cos(A1)+yc*sin(A1);
y1c=0;
z1c=zc;

H=fabs(x1c-x1p);
P=sqrt((y1c-y1p)*(y1c-y1p)+(z1c-z1p)*(z1c-z1p));


/* second transformation of YZ plane*/

if (z1c=z1p)
{
        A2=PI/2;
}
else
{
        A2=atan((y1c-y1p)/(z1c-z1p));
}

x2p=x1p; y2p=-z1p*sin(A2)+y1p*cos(A2);   z2p=z1p*cos(A2)+y1p*sin(A2);
x2c=x1c; y2c=-z1c*sin(A2)+y1c*cos(A2);   z2c=z1c*cos(A2)+y1c*sin(A2);

/* equation of the circles describing the parameters of right-circular cone are  */



  if (P>Ro)
```

```
  {
  Alphamax=asin(Ro/P);
W1=Alphamax/PI;

/* Calculate x: random number uniformly
    distributed in range 0 to 1 */
  for (j = 0, sum_0 = 0., sum_1 = 0.,sum_2=0.; j <= 1000; j++)
    {
idum !=MASK;
          k=(idum)/IQ;
          idum=IA*(idum-k*IQ)-IR*k;
          if(idum<0) idum+=IM;
          x=AM*(idum);
          idum != MASK;
          printf ("value of x is%f\n", x);


          /* calculation of various angles*/

          Alpha= Alphamax*(2*x-1); printf("value of Alpha %f\n", Alpha);

OA=P*cos(Alpha)+sqrt(Ro*Ro-P*P*sin(Alpha)*sin(Alpha));

OB=P*cos(Alpha)-sqrt(Ro*Ro-P*P*sin(Alpha)*sin(Alpha));

Thetamax= atan(OA/H);

Thetacrit=atan(OB/H);

Thetamin=atan(OB/(H+L));

y = (double) rand() / (double) RAND_MAX;  //second random number generator for
Theta

          Theta =acos(cos(Thetamin)-y*(cos(Thetamin)-cos(Thetamax)));
if(z2p<=z2c)
{
          Theta1=Theta;
}
else
{
          Theta1=PI-Theta;
}
alpha2=Theta1;
beta2=acos(sin(Theta1)*sin(Alpha));
gamma2=acos(sin(Theta1)*cos(Alpha));
```

```
A=
pow(cos(alpha2),2)+pow(cos(gamma2)*sin(A2),2)+2*cos(beta2)*cos(gamma2)*sin(A2)
*cos(A2)+
pow(cos(beta2)*cos(A2),2)-pow(cos(gamma2)*cos(A2)*tan(Cangle),2)
-pow(cos(beta2)*sin(A2)*tan(Cangle),2)+
2*cos(gamma2)*cos(beta2)*cos(A2)*sin(A2)*pow(tan(Cangle),2);

B= 2*x2p*cos(alpha2) +2*z2p*cos(gamma2) *pow(sin(A2)
,2)+2*y2p*cos(beta2)*pow(cos(A2) ,2)+
2*y2p*cos(gamma2)*sin(A2)*cos(A2)+2*z2p*cos(beta2)*sin(A2)*cos(A2)
-2*z2p*cos(gamma2)*pow(cos(A2)*tan(Cangle) ,2)-
2*y2p*cos(beta2)*pow(sin (A2)*tan(Cangle) ,2) +
2*y2p*cos(gamma2)*cos(A2)*sin(A2)*pow(tan(Cangle) ,2)+
2*z2p*cos(beta2)*cos(A2)*sin(A2)* pow(tan(Cangle)
,2)+.115*cos(beta2)*sin(A2)*tan(Cangle)
-.115*cos(alpha2)*cos(A2)*tan(Cangle);

C= pow(x2p,2)+pow(z2p*sin(A2) ,2)+pow(y2p*cos(A2)
,2)+2*y2p*z2p*sin(A2)*cos(A2)
-pow(z2p*cos(A2)*tan(Cangle) ,2)-pow(y2p*sin(A2)*tan(Cangle) ,2)
+2*y2p*z2p*cos(A2)*sin(A2)* pow(tan(Cangle) ,2)-.00331-
.115*z2p*cos(A2)*tan(Cangle)
+ .115*y2p*sin(A2)*tan(Cangle);

DISC=(B*B-4*A*C);
if(DISC>=0)
{

D=sqrt(DISC);

t1=((-B+D)/(2*A));
t2=((-B-D)/(2*A));

        x2=x2p+t1*cos(alpha2);
        y2=y2p+t1*cos(beta2);
        z2=z2p+t1*cos(gamma2);



        x3=x2p+t2*cos(alpha2);
        y3=y2p+t2*cos(beta2);
        z3=z2p+t2*cos(gamma2);

dr= sqrt(pow(x2p-x2,2)+pow(y2p-y2,2)+pow(z2p-z2,2));

dr1= sqrt(pow(x2p-x3,2)+pow(y2p-y3,2)+pow(z2p-z3,2));

// Quadratic equation for distance travelled by photone in the wall I.e. Thickness
```

```
A3=pow(cos(alpha2),2)+pow(cos(gamma2)*sin(A2),2)+2*cos(beta2)*cos(gamma2)*sin(
A2)*cos(A2)+
pow(cos(beta2)*cos(A2),2)-pow(cos(gamma2)*cos(A2)*tan(Cangle),2)
-pow(cos(beta2)*sin(A2)*tan(Cangle),2)+
2*cos(gamma2)*cos(beta2)*cos(A2)*sin(A2)*pow(tan(Cangle),2);


B3=2*x2p*cos(alpha2) +2*z2p*cos(gamma2) *pow(sin(A2)
,2)+2*y2p*cos(beta2)*pow(cos(A2) ,2)+
2*y2p*cos(gamma2)*sin(A2)*cos(A2)+2*z2p*cos(beta2)*sin(A2)*cos(A2)
-2*z2p*cos(gamma2)*pow(cos(A2)*tan(Cangle) ,2)-
2*y2p*cos(beta2)*pow(sin (A2)*tan(Cangle) ,2) +
2*y2p*cos(gamma2)*cos(A2)*sin(A2)*pow(tan(Cangle) ,2)+
2*z2p*cos(beta2)*cos(A2)*sin(A2)* pow(tan(Cangle)
,2)+.117*cos(beta2)*sin(A2)*tan(Cangle)
-.117*cos(alpha2)*cos(A2)*tan(Cangle);

C3=pow(x2p,2)+pow(z2p*sin(A2) ,2)+pow(y2p*cos(A2)
,2)+2*y2p*z2p*sin(A2)*cos(A2)
-pow(z2p*cos(A2)*tan(Cangle) ,2)-pow(y2p*sin(A2)*tan(Cangle) ,2)
+2*y2p*z2p*cos(A2)*sin(A2)* pow(tan(Cangle) ,2)-.0034223-
.117*z2p*cos(A2)*tan(Cangle)
+.117*y2p*sin(A2)*tan(Cangle);

LODA=(B3*B3-4*A3*C3);
if(LODA>=0)
{

D3=sqrt(LODA);
t3=( (-B3+D3) / (2*A3));
t4=( (-B3-D3) / (2*A3));

x4=x2p+t3*cos(alpha2) ;
y4=y2p+t3*cos(beta2);
z4=z2p+t3*cos(gamma2) ;

x5=x2p+t4*cos(alpha2) ;
y5=y2p+t4*cos(beta2);
z5=z2p+t4*cos(gamma2) ;

dr2= sqrt(pow(x2p-x4,2)+pow(y2p-y4,2)+pow(z2p-z4,2));

dr3= sqrt(pow(x2p-x5,2)+pow(y2p-y5,2)+pow(z2p-z5,2));

if(dr>=dr1)
{
if(dr2>=dr3)
```

```
{
Th=dr2-dr;  // As dr is the real solution for distance covered by the photon the reactor.
}
else
{
        Th=dr3-dr;
}
//   dr2 is the solution to the distance travelled by inside the wall.


printf (" the distance travelled in wall is %f\n",Th);
fa=exp(-ur*dr-uw*Th);

}

else
{
if(dr2>=dr3)
{
        Th=dr2-dr1;
}
else
{
        Th=dr3-dr1;
}
printf (" the distance travelled in wall is %f\n",Th);
fa=exp(-ur*dr1-uw*Th);
printf ("Value of fa is %f\n", fa);
}
W2=(cos(Thetamin)-cos(Thetamax))/2.0;



          if (Theta<Thetacrit) /* Photon enters from the lateral side*/
{
          T= H*(tan(Thetamax)-tan(Thetacrit));
N=(H+L)*(tan(Theta)-tan(Thetamin));



if (T>N)          /* Photon leaves from the bottom of the detector*/
{
        d=(H+L)/cos(Theta)-(P*cos(Alpha)-sqrt(.25*L*L-
P*P*sin(Alpha)*sin(Alpha)))/sin(Theta);
}


else  /* photon leaves from the lateral side*/
```

```
{
        d=2*(sqrt(L*L*.25-P*P*sin(Alpha)*sin(Alpha)))/sin(Theta);
}

}


else       /*Photon enters from the top*/
{
        N1=(H+L)*tan(Theta);
        T1= H*tan(Thetamax);
        if (T1>N1) /* photon leaves from the bottom*/
        {
                d=L/cos(Theta);
        }


        else /* photon leaves from the lateral side*/
        {
                d=(P*cos(Alpha)+sqrt(L*L*.25-
P*P*sin(Alpha)*sin(Alpha)))/sin(Theta)+H/cos(Theta);
        }}

        fD=1-exp(-uD*d); /* calculation of probability fD*/

        W3=W1*W2;
        W=W1*W2*fD*fa;
          printf("Value of total weight is %f", W);

  }
else
{
        W=0;

}}
else
{
        W=0;

}

sum_0 =sum_0+ W;
  printf("value of sum is %f\n",sum_0);

  sum_1 = sum_1+(W*W);
           sum_2=sum_2+W3;

}
```

```
Omega = (sum_2/j);
printf("value of omega is %f\n", Omega);
Eff = (sum_0 / (j));
cout<<"Value of Efficiency is" <<Eff;
var = sqrt(((sum_1)/(Omega*Omega)-i*Eff*Eff) / (i*(i-1)));
printf("value of Alphamax is %f\n", Alphamax);

printf("Value of weight W1=%f\n", W1);

}

//*****************************************************************
***
// Photon is located along the axis of the detector and this is          *
// complete program in itself, with all the steps as in the program      *
//above.                                                                 *
//*****************************************************************
***

else            /*if p <Ro i.e tracer is located along the axis of the detector*/
  {
          Thetamax=atan((Ro+P)/H);
          Thetacrit=atan((Ro-P)/H);

          Thetamin=0;
          for (j = 0, sum_0 = 0., sum_1 = 0.; j <= 1000; j++)
   {

idum !=MASK;
        k=(idum)/IQ;
        idum=IA*(idum-k*IQ)-IR*k;
        if(idum<0) idum+=IM;
        x=AM*(idum);
        idum != MASK;
        printf ("value of x is%f\n", x);

Theta =acos(cos(Thetamin)-x*(cos(Thetamin)-cos(Thetamax)));

cout<<"value of x is" <<x<<endl;

        W2=(cos(Thetamin)-cos(Thetamax))/2.0;

if(Theta<Thetacrit)

{
        W1=1;
        printf("Value of weight W1=%f\n", W1);
```

```
        d=L;      /* photon always leaves from the bottom*/
y = (double) rand() / (double) RAND_MAX;   /* second random number generator for
Alpha*/
Alpha= 2*PI*y;

}
else
{

Alphamax=acos((P*P+H*H*tan(Theta)*tan(Theta)-Ro*Ro)/(2*H*P*tan(Theta)));


y = (double) rand() / (double) RAND_MAX;   /* second random number generator for
Theta*/
Alpha= Alphamax*(2*y-1);

W1=Alphamax/PI;


TI=H*tan(Thetamax)*cos(Alpha);
Theta2=atan(TI/(H+L));
Theta3=atan(TI/H);


if (Theta<=Theta2) /* photon leaves from the bottom*/
{

d=L/cos(Theta);
}
else
{
        /* photon leaves from the lateral side*/

                d=(P*cos(Alpha)+sqrt(L*L*.25-
P*P*sin(Alpha)*sin(Alpha)))/sin(Theta)+H/cos(Theta);
}


}

if(z2p<=z2c)
{
        Theta1=Theta;
}
else
{
        Theta1=PI-Theta;
}
```

```
alpha2=Theta1;
beta2=acos(sin(Theta1)*sin(Alpha));
gamma2=acos(sin(Theta1)*cos(Alpha));

A=
pow(cos(alpha2),2)+pow(cos(gamma2)*sin(A2),2)+2*cos(beta2)*cos(gamma2)*sin(A2)
*cos(A2)+
pow(cos(beta2)*cos(A2),2)-pow(cos(gamma2)*cos(A2)*tan(Cangle),2)
-pow(cos(beta2)*sin(A2)*tan(Cangle),2)+
2*cos(gamma2)*cos(beta2)*cos(A2)*sin(A2)*pow(tan(Cangle),2);

B= 2*x2p*cos(alpha2) +2*z2p*cos(gamma2) *pow(sin(A2)
,2)+2*y2p*cos(beta2)*pow(cos(A2) ,2)+
2*y2p*cos(gamma2)*sin(A2)*cos(A2)+2*z2p*cos(beta2)*sin(A2)*cos(A2)
-2*z2p*cos(gamma2)*pow(cos(A2)*tan(Cangle) ,2)-
2*y2p*cos(beta2)*pow(sin (A2)*tan(Cangle) ,2) +
2*y2p*cos(gamma2)*cos(A2)*sin(A2)*pow(tan(Cangle) ,2)+
2*z2p*cos(beta2)*cos(A2)*sin(A2)* pow(tan(Cangle)
,2)+.115*cos(beta2)*sin(A2)*tan(Cangle)
-.115*cos(alpha2)*cos(A2)*tan(Cangle);


C=pow(x2p,2)+pow(z2p*sin(A2) ,2)+pow(y2p*cos(A2)
,2)+2*y2p*z2p*sin(A2)*cos(A2)
-pow(z2p*cos(A2)*tan(Cangle) ,2)-pow(y2p*sin(A2)*tan(Cangle) ,2)
+2*y2p*z2p*cos(A2)*sin(A2)* pow(tan(Cangle) ,2)-.00331-
.115*z2p*cos(A2)*tan(Cangle)
+.115*y2p*sin(A2)*tan(Cangle);



DISC=(B*B-4*A*C);
if (DISC>=0)
{
D=sqrt(DISC);


t1=((-B+D)/(2*A));
t2=((-B-D)/(2*A));


        x2=x2p+t1*cos(alpha2);
        y2=y2p+t1*cos(beta2);
        z2=z2p+t1*cos(gamma2);


        x3=x2p+t2*cos(alpha2);
        y3=y2p+t2*cos(beta2);
```

```
        z3=z2p+t2*cos(gamma2);

dr= sqrt(pow(x2p-x2,2)+pow(y2p-y2,2)+pow(z2p-z2,2));


dr1= sqrt(pow(x2p-x3,2)+pow(y2p-y3,2)+pow(z2p-z3,2));

/* Quadratic equation for distance travelled by photone in the wall I.e. Thickness */

A3=pow(cos(alpha2),2)+pow(cos(gamma2)*sin(A2),2)+2*cos(beta2)*cos(gamma2)*sin(
A2)*cos(A2)+
pow(cos(beta2)*cos(A2),2)-pow(cos(gamma2)*cos(A2)*tan(Cangle),2)
-pow(cos(beta2)*sin(A2)*tan(Cangle),2)+
2*cos(gamma2)*cos(beta2)*cos(A2)*sin(A2)*pow(tan(Cangle),2);

B3=2*x2p*cos(alpha2) +2*z2p*cos(gamma2) *pow(sin(A2)
,2)+2*y2p*cos(beta2)*pow(cos(A2) ,2)+
2*y2p*cos(gamma2)*sin(A2)*cos(A2)+2*z2p*cos(beta2) *sin(A2)*cos(A2)
-2*z2p*cos(gamma2)*pow(cos(A2)*tan(Cangle) ,2)-
2*y2p*cos(beta2)*pow(sin (A2)*tan(Cangle) ,2) +
2*y2p*cos(gamma2)*cos(A2)*sin(A2)*pow(tan(Cangle) ,2)+
2*z2p*cos(beta2)*cos(A2)*sin(A2)* pow(tan(Cangle)
,2)+.117*cos(beta2)*sin(A2)*tan(Cangle)
-.117*cos(alpha2)*cos(A2)*tan(Cangle);

C3=pow(x2p,2)+pow(z2p*sin(A2) ,2)+pow(y2p*cos(A2)
,2)+2*y2p*z2p*sin(A2)*cos(A2)
-pow(z2p*cos(A2)*tan(Cangle) ,2)-pow(y2p*sin(A2)*tan(Cangle) ,2)
+2*y2p*z2p*cos(A2)*sin(A2)* pow(tan(Cangle) ,2)-.0034223-
.117*z2p*cos(A2)*tan(Cangle)
+.117*y2p*sin(A2)*tan(Cangle);

LODA=B3*B3-4*A3*C3;
if(LODA>=0)
{

D3=sqrt(B3*B3-4*A3*C3) ;

t3=( (-B3+D3) / (2*A3));
t4=( (-B3-D3) / (2*A3));

x4=x2p+t3*cos(alpha2) ;
y4=y2p+t3*cos(beta2);
z4=z2p+t3*cos(gamma2) ;

x5=x2p+t4*cos(alpha2) ;
y5=y2p+t4*cos(beta2);
z5=z2p+t4*cos(gamma2) ;
```

```
dr2= sqrt(pow(x2p-x4,2)+pow(y2p-y4,2)+pow(z2p-z4,2));

dr3= sqrt(pow(x2p-x5,2)+pow(y2p-y5,2)+pow(z2p-z5,2));

if (dr<=dr1)
{
 Th=dr2-dr;  //As dr is the real solution for distance covered by the photon the reactor.
          //  dr2 is the solution to the distance travelled by inside the wall

printf (" the distance travelled in wall is %f\n",Th);
fa=exp(-ur*dr-uw*Th);
printf("Value of fa is %f\n", fa);
}
else
{
         Th=dr3-dr1;
printf (" the distance travelled in wall is %f\n",Th);
fa=exp(-ur*dr1-uw*Th);
printf ("Value of fa is %f\n", fa);
}
fD=1-exp(-uD*d);

W=W1*W2*fD*fa;
W3=W1*W2;


}
else
{
         W=0;

}}
else
{
         W=0;

}


  sum_0 += W;
     sum_1 += (W3);

           printf("value of sum is %f\n",sum_0);
}

Omega=sum_1/j;
Eff = (sum_0/(j));
```

```
        var = sqrt((sum_1-i*Eff*Eff) / (i*(i-1)));

printf("value of Alphamax is %f\n", Alphamax);
printf("Eff = %f  var = %f\n", Eff,var );
printf("value of Thetacrit is%f\n", Thetacrit);
printf("value of H is %f\n", H);
printf("value of P is %f\n", P);

}

/* Calculation of number of counts from total efficiency and photopeak to total ratio*/

Counts=(Timeinterval*V*strenght*ratio*Eff)/(1+Deadtime*V*strenght*ratio*Eff);

out_file1 <<xp <<","<<yp<<","<<zp<<","<<Eff <<","<<Counts <<endl;
}
getch() ;
return 0;
}
```

Appendix G

The following code was written to convert the absolute γ-ray counts recorded by the scintillation detectors to relative counts with respect to all the detectors. This was done for both simulated and actual counts.

```
#include <stdlib.h>
#include <stdio.h>
#include <fstream>
#include<iostream>
#include <conio.h>
#include<math.h>
#include<iomanip>

main()
{
        using namespace std;
        int i,j;
long double x[19500], y[19500], z[19500], c1,c2,c3,c4,c5,c6,c7,c8,c9,c10,c11,c12,
m1,m2,m3,m4,m5,m6,m7,
m8,m9,m10,m11,m12,
a=0,b=0,c=0,f=0,k,M1,M2,M3,M4,M5,M6,M7,M8,M9,M10,M11,M12;
long double l,m,n,o;

ifstream in1("C:/Documents and Settings/Todd/My Documents/Visual Studio
Projects/counts/counts1.txt");  ifstream in2("C:/Documents and Settings/Todd/My
Documents/Visual Studio Projects/counts2/counts2.txt");ifstream in3("C:/Documents and
Settings/Todd/My Documents/Visual Studio Projects/counts3/counts3.txt");  ifstream
in4("C:/Documents and Settings/Todd/My Documents/Visual Studio
Projects/counts4/counts4.txt");
ifstream in5("C:/Documents and Settings/Todd/My Documents/Visual Studio
Projects/counts5/counts5.txt");  ifstream in6("C:/Documents and Settings/Todd/My
Documents/Visual Studio Projects/counts6/counts6.txt");
ifstream in7("C:/Documents and Settings/Todd/My Documents/Visual Studio
Projects/counts7/counts7.txt");  ifstream in8("C:/Documents and Settings/Todd/My
Documents/Visual Studio Projects/counts8/counts8.txt");
ifstream in9("C:/Documents and Settings/Todd/My Documents/Visual Studio
Projects/counts9/counts9.txt");  ifstream in10("C:/Documents and Settings/Todd/My
Documents/Visual Studio Projects/counts10/counts10.txt");//inputs data from 12 files
ifstream in11("C:/Documents and Settings/Todd/My Documents/Visual Studio
Projects/counts11/counts11.txt");ifstream in12("C:/Documents and Settings/Todd/My
Documents/Visual Studio Projects/counts12/counts12.txt");

ifstream in13; ifstream in14; ifstream in15; ifstream in16;
ifstream in17; ifstream in18; ifstream in19; ifstream in20;
ifstream in21; ifstream in22; ifstream in23;ifstream in24;
ofstream out_file1;
```

```
out_file1.open("count1.txt");
ofstream out_file2;
out_file2.open("count2.txt"); //opening 12 output data files
ofstream out_file3;
out_file3.open("count3.txt");
ofstream out_file4;
out_file4.open("count4.txt");
ofstream out_file5;
out_file5.open("count5.txt");
ofstream out_file6;
out_file6.open("count6.txt");
ofstream out_file7;
out_file7.open("count7.txt");
ofstream out_file8;
out_file8.open("count8.txt");
ofstream out_file9;
out_file9.open("count9.txt");
ofstream out_file10;
out_file10.open("count10.txt");
ofstream out_file11;
out_file11.open("count11.txt");
ofstream out_file12;
out_file12.open("count12.txt");

while(!in1.eof())
{

in1 >> m1; in2 >> m2; in3>> m3; in4>> m4; in6>> m6; in7>> m7; in8>> m8;
in9>> m9; in10>> m10; in11>> m11; in12>> m12;
k=m1+m2+m3+m4+m6+m7+m8+m9+m10+m11+m12;
M1=m1/k; M2=m2/k; M3=m3/k; M4=m4/k; M6=m6/k; M7=m7/k; M8=m8/k;
M9=m9/k;
M10=m10/k; M11=m11/k; M12=m12/k;

out_file1<<"\n"<<M1;out_file2<<"\n"<<M2;out_file3<<"\n"<<M3;out_file4<<"\n"<<M
4;
out_file6<<"\n"<<M6;
out_file7<<"\n"<<M7;out_file8<<"\n"<<M8;out_file9<<"\n"<<M9;out_file10<<"\n"<<
M10;
out_file11<<"\n"<<M11;out_file12<<"\n"<<M12;

}
getch();

}
```

Appendix H

The following code was written in C++ to compare the counts recorded by each detector interval with the counts calculated at 19,200 points inside the vessel to find the location of the tracer particle.

```
#include <stdlib.h>
#include <stdio.h>
#include <fstream>
#include<iostream>
#include <conio.h>
#include<math.h>
#include<iomanip>



main()
{
        using namespace std;
        int i,j;
long double x[19500], y[19500], z[19500], c1,c2,c3,c4,c5,c6,c7,c8,c9,c10,c11,c12,
m1,m2,m3,m4,m5,m6,m7,
m8,m9,m10,m11,m12, a=0,b=0,c=0,f=0,k;
long double l,m,n,o;
ifstream in1("count1.txt");  ifstream in2("count2.txt");
ifstream in3("count3.txt");  ifstream in4("count4.txt");
ifstream in5("count5.txt");  ifstream in6("count6.txt");
ifstream in7("count7.txt");  ifstream in8("count8.txt");
ifstream in9("count9.txt");  ifstream in10("count10.txt");
ifstream in11("count11.txt");ifstream in12("count12.txt");
ifstream in13; ifstream in14; ifstream in15; ifstream in16;
ifstream in17; ifstream in18; ifstream in19; ifstream in20;
ifstream in21; ifstream in22; ifstream in23;ifstream in24;
ofstream out_file;
out_file.open("data.txt");
while(!in1.eof())
{
in13.open("detectors1.txt");in14.open("detectors2.txt");in15.open("detectors3.txt");
in16.open("detectors4.txt");in17.open("detectors5.txt");in18.open("detectors6.txt");
in19.open("detectors7.txt");in20.open("detectors8.txt");in21.open("detectors9.txt");
in22.open("detectors10.txt");in23.open("detectors11.txt");in24.open("detectors12.txt");


        k=10000;

in1 >> m1; in2 >> m2; in3>> m3; in4>> m4; in6>> m6; in7>> m7; in8>> m8;
in9>> m9; in10>> m10; in11>> m11; in12>> m12;
```

```
for(j=0; j<=18500;j++)
{
in13 >>x[j] >>y[j] >>z[j] >> c1; in14>>c2; in15>>c3; in16>>c4;
in18>> c6; in19>>c7; in20>> c8; in21>>c9; in22>>c10; in23>>c11; in24>>c12;

f=pow((c1-m1),2)/c1 + pow((c2-m2),2)/c2 + pow((c3-m3),2)/c3 + pow((c4-m4),2)/c4
 + pow((c6-m6),2)/c6 + pow((c7-m7),2)/c7 + pow((c8-m8),2)/c8
+ pow((c9-m9),2)/c9 + pow((c10-m10),2)/c10 + pow((c11-m11),2)/c11 + pow((c12-
m12),2)/c12;

if (f<k)
{
        k=f;
a=x[j]; b=y[j]; c=z[j];


}

}

j=0;
cout<<a<<b<<c<<"  "<<k<<endl;

out_file<<"\n"<<a<<"  "<<b<<"   "<<c<<endl;

in13.close();in14.close();in15.close();in16.close();in17.close();in18.close();
in19.close();in20.close();in21.close();in22.close();in23.close();in24.close();
}

getch();

}
```

Appendix I

The following code was written in C++ for the data analysis of the RPT data.

```
#include<stdlib.h>
#include<stdio.h>
#include<conio.h>
#include<iostream>
#include<math.h>
#include<fstream>
#include<iomanip>
# define PI 3.14159
main()
{
using namespace std;
int a=0,b=0,c=0,d=0,e=0,f=0,g=0,h=0,i=0,j=0,k=0,l=0,m=0,n=0,o=0;
double x=0,y=0,z=0,x1=0,y1=0,z1=0,X,Y,Z, disp, vel,t=.03,theta,r=0;
double v1=0, v2=0,v3=0,v4=0,v5=0,v6=0,v7=0,v8=0,
v9=0,v10=0,v11=0,theta1=0,theta2=0,theta3=0,theta4=0,
theta5=0,theta6=0,theta7=0,theta8=0,theta9=0,theta10=0,theta11=0,r1=0,Z1=0,Vr,Vz;
double meanv1, meanv2, meanv3, meanv4, meanv5, meanv6,meanv7, meanv8, meanv9,
meanv10, meanv11, meantheta1, meantheta2,
meantheta3,meantheta4,meantheta5,meantheta6,meantheta7, meantheta8,
meantheta9,meantheta10,meantheta11;
double meanVr1,meanVr2,
meanVr3,meanVr4,meanVr5,meanVr6,meanVr7,meanVr8,meanVr9,meanVr10,meanVr1
1,
meanVz1,meanVz2,meanVz3,meanVz4,meanVz5,meanVz6,meanVz7,meanVz8,meanVz
9,meanVz10,meanVz11,
Vr1=0,Vr2=0,Vr3=0,Vr4=0,Vr5=0,Vr6=0,Vr7=0,Vr8=0,Vr9=0,Vr10=0,Vr11=0,Vz1=0,
Vz2=0,
Vz3=0,Vz4=0,Vz5=0,Vz6=0,Vz7=0,Vz8=0,Vz9=0,Vz10=0,Vz11=0,R=0;
ifstream in1("data.txt");

ofstream out_file1;
out_file1.open("velocity.txt");

ofstream out_file2;
out_file2.open("time.txt");

ofstream out_file3;
out_file3.open("velocity_vector.txt");

ofstream out_file4;
out_file4.open("velocity_vector1.txt");

ofstream out_file5;
```

```
out_file5.open("velocity_vector2.txt");

ofstream out_file6;
out_file6.open("velocity_vector3.txt");

 while(!in1.eof())
{
        in1  >>x1>> y1 >>z1;

        disp= pow((pow((x1-x),2)+pow((y1-y),2)+pow((z1-z),2)),0.5);
        vel=disp/t;
        X=(x1+x)/2;  Y=(y1+y)/2;  Z=(z1+z)/2;

        theta=(atan((z1-z)/(x1-x)))*(180/PI);


r=pow((x1*x1+y1*y1),0.5);

          Vr=(r-r1)/t;
          Vz= (z1-z)/t;

x=x1; y=y1; z=z1;
          Z1=Z; R=pow((X*X+Y*Y),0.5);;
r1=r;
if (Z<=.20)
{
        if(Z>0.0)
        {
if (vel>0)
{
        if(vel<5)

        {


          out_file3 <<X<<"  "<<Y<<"  "<<Z<<"  "<<R<<"  "<<Vr<<"  "<<Vz <<endl;



       if (r<0.01)
                {
                        Vr1=Vr1+Vr;
                                Vz1=Vz1+Vz;
         v1=v1+vel;
                        theta1=theta1+theta;
                        a=a+1;
out_file4 <<Vr<<"    "<<Vz<<endl;
                }
```

```
if(r>.01)
{
  if(r<.02)
        {Vr2=Vr2+Vr;
              Vz2=Vz2+Vz;
              v2=v2+vel;
              theta2=theta2+theta;
              b=b+1;

        }}

if(r>.02)
{
if (r<.03)
        {Vr3=Vr3+Vr;
              Vz3=Vz3+Vz;
              v3=v3+vel;
              theta3=theta3+theta;
              c=c+1;

        }}

if(r>.03)
{
if (r<.04)
        {
Vr4=Vr4+Vr;
              Vz4=Vz4+Vz;
              v4=v4+vel;
              theta4=theta4+theta;
              d=d+1;
        }}
if(r>.04)
{

        if(r<.05)
        {
              Vr5=Vr5+Vr;
              Vz5=Vz5+Vz;
              v5=v5+vel;
              theta5=theta5+theta;
              e=e+1;
        }}
if(r>.05)
{
        if(r<.06)
```

```
        {
                Vr6=Vr6+Vr;
                Vz6=Vz6+Vz;
                v6=v6+vel;
                theta6=theta6+theta;
                f=f+1;
        }}
if(r>.06)
{

        if(r<.07)
        {
                Vr7=Vr7+Vr;
                Vz7=Vz7+Vz;
                v7=v7+vel;
                theta7=theta7+theta;
                g=g+1;
        }}

if(r>.07)
{
if(r<.08)
        {
                Vr8=Vr8+Vr;
                Vz8=Vz8+Vz;
                v8=v8+vel;
                theta8=theta8+theta;
                h=h+1;
        }}

if(r>.08)
{
if(r<.09)
        {
                Vr9=Vr9+Vr;
                Vz9=Vz9+Vz;
                v9=v9+vel;
        theta9=theta9+theta;
        i=i+1;
        }}
if(r>.09)
{
        if(r<.1)
        {
                Vr10=Vr10+Vr;
                Vz10=Vz10+Vz;
                v10=v10+vel;
                theta10=theta10+theta;
```

```
                        j=j+1;
                }}

                else
                {
                        Vr11=Vr11+Vr;
                        Vz11=Vz11+Vz;
                        v11=v11+vel;
                        theta11=theta11+theta;
                        k=k+1;
                }}}}

        if (Z<.04)
        {
                l=l+1;
        }
        if(Z>.04)
        {
                if(Z<.08)
                {
                        m=m+1;
                }}
        if(Z>.08)
        {
                if(Z<.12)
                {
                        n=n+1;
                }}
        if(Z>.12)
        {
                if(Z<.16)
                {
                        o=o+1;
                }}

        }}

meanv1= v1/a;  meantheta1=theta1/a; meanVr1=Vr1/a; meanVz1=Vz1/a;
meanv2=v2/b; meantheta2=theta2/b; meanVr2=Vr2/b; meanVz2=Vz2/b;
meanv3=v3/c; meantheta3=theta3/c; meanVr3=Vr3/c; meanVz3=Vz3/c;
meanv4=v4/d; meantheta4=theta4/d; meanVr4=Vr4/d; meanVz4=Vz1/d;
meanv5=v5/e; meantheta5=theta5/e; meanVr5=Vr5/e; meanVz5=Vz5/e;
meanv6=v6/f; meantheta6=theta6/f; meanVr6=Vr6/f; meanVz6=Vz6/f;
meanv7=v7/g; meantheta7=theta7/g; meanVr7=Vr7/g; meanVz7=Vz7/g;
meanv8=v8/h; meantheta8=theta8/h; meanVr8=Vr8/h; meanVz8=Vz8/h;
meanv9=v9/i; meantheta9=theta9/i; meanVr9=Vr9/i; meanVz9=Vz9/i;
meanv10=v10/j; meantheta10=theta10/j; meanVr10=Vr10/j; meanVz10=Vz10/j;
meanv11=v11/k; meantheta11=theta11/k; meanVr11=Vr1/k; meanVz11=Vz11/k;
```

```
out_file1 <<meanv1  <<"   "<<meanVr1 <<"  "<<meanVz1 <<"   " <<a <<endl;
out_file1 <<meanv2  <<"   "<<meanVr2<<"  "<<meanVz2 <<"  "<<b <<endl;
out_file1 <<meanv3  <<"   "<<meanVr3<<"  "<<meanVz3<<"  "<<c<<endl;
out_file1 <<meanv4  <<"   "<<meanVr4<<"  "<<meanVz4<<"  "<<d <<endl;
out_file1 <<meanv5  <<"   "<<meanVr5<<"  "<<meanVz5<<"  "<<e <<endl;
out_file1 <<meanv6  <<"   "<<meanVr6<<"  "<<meanVz6<<"  "<<f <<endl;
out_file1 <<meanv7  <<"   "<<meanVr7<<"  "<<meanVz7<<"  "<<g <<endl;
out_file1 <<meanv8  <<"   "<<meanVr8<<"  "<<meanVz8<<"  "<<h <<endl;
out_file1 <<meanv9  <<"   "<<meanVr9<<"  "<<meanVz9<<"  "<<i <<endl;
out_file1 <<meanv10  <<"  "<<meanVr10<<"  "<<meanVz10<<"  "<<j<<endl;
out_file1 <<meanv11  <<"  "<<meanVr11<<"  "<<meanVz11<<"  "<<k <<endl;


out_file2 <<".04"<<"  "<<l<<endl;
out_file2 <<".08"<<"  "<<m<<endl;
out_file2 <<".12"<<"  "<<n<<endl;
out_file2 <<".16"<<"  "<<o<<endl;

getch();

}
```